Tailored Doping Strategies for Photocatalytic CO_2 Reduction and Water Splitting on $KCa_2Nb_3O_{10}$ Layered Perovskite

by

Bengisu Yılmaz

A Dissertation Submitted to the Graduate
School of Sciences and Engineering in
Partial Fulfillment of the Requirements for
the Degree of
Doctor of
Philosophy
in

Material Science and Engineering

KOÇ ÜNİVERSİTESİ

December 6, 2023

Tailored Doping Strategies for Photocatalytic CO_2 Reduction and Water Splitting on $KCa_2Nb_3O_{10}$ Layered Perovskite

Koç University

Graduate School of Sciences and Engineering

This is to certify that I have examined this copy of a doctoral dissertation by

Bengisu Yılmaz

and have found that it is complete and satisfactory in all respects,
and that any and all revisions required by the final
examining committee have been made.

Committee Members:

Assoc Prof Uğur Ünal (Advisor)

Assoc Prof Sarp Kaya

Assoc Prof Ferdi Karadaş

Assoc. Prof. Mustafa Kemal Bayazıt

Assist Prof Safacan Kölemen

Date: 06.12.2023

With heartfelt appreciation, I dedicate this dissertation to my family, whose endless love and encouragement have been my constant inspiration.

ABSTRACT

Tailored Doping Strategies for Photocatalytic CO_2 Reduction and Water Splitting on $KCa_2Nb_3O_{10}$ Layered Perovskite

Doctor of Philosophy in Materials Science and Engineering December 6, 2023

Global warming is defined as the long-term heating of the Earth's surface that has been observed since the pre-industrial period. This phenomenon is primarily driven by human activities, especially the use of fossil fuels, and is accompanied by various consequences such as the increasing global population and industrialization, leading to elevated greenhouse gas levels in the atmosphere and a reduction in green areas. The negative effects of global warming and related climate change, the world's most critical problem, are becoming more serious day by the day. Researchers and industries are pursuing two main approaches to address the challenge of reducing CO_2 emissions. The primary approach is to tackle CO_2 emissions at the production level by reducing reliance on fossil fuels and exploring alternative energy sources such as hydrogen energy. The second way is clearly to convert CO_2 into useful products. Recently, photocatalytic reactions have gained popularity in converting CO_2 to useful chemicals and producing H_2 from water due to their features such as being environmentally friendly, simpler to set-up, more cost-effective, and more scalable. Yet, there is more to investigate about photocatalyst systems. The use of hole-scavengers to improve photocatalytic activity has been widely used, but the behavior of hole-scavengers on 2D nanosheets of perovskite photocatalysts has yet to be discovered. Another way to improve the photocatalytic activity is the utilization of co-catalyst particles on the surface of the photocatalyst. Given that only the surface atoms of particles actively participate in photocatalytic reactions while the inner atoms remain inactive, the sustainability of using co-catalyst particles, especially those incorporating noble metals, becomes a concern. Thus, it is crucial to disperse single-atom co-catalysts in a photocatalytic system.

Hole scavenger study as a first chapter, aims to mechanistically investigate the photocatalytic performance of hole scavengers on nanosheets of 2D layered $KCa_2Nb_3O_{10}$ perovskite oxide. A range of hole scavengers were added to the photocatalytic system to observe how they influence the charge carrier dynamics and overall photocatalytic

efficiency. To analyze the behavior of hole scavengers on a $[Ca_2Nb_3O_{10}]^-$ perovskite nanosheet, photoelectrochemical and photocatalytic experiments were utilized.

Investigation of single site noble atom doped 2D layered perovskite for photocatalytic hydrogen evolution reactions is a second chapter. Pd noble metal was chosen for single-site atom doping. The incorporation of Pd as a single-site atom dopant altered the electrical band structure of the photocatalyst. Depending on the doping concentration, this caused the narrowing or shifting of the bandgap to visible spectrum. Also, it can serve as an active site for photocatalytic reactions, facilitating the transfer of charge carriers. Pd doping reduced the recombination rate of electron-hole pairs by providing additional reaction pathways, leading to more efficient charge utilization.

In the last chapter, the photocatalytic CO_2 reduction performances and photocatalytic activities were investigated by using ultrathin 2D layered Dion-Jacobson type perovskite oxide $KCa_2Nb_3O_{10}$ with single-site ruthenium doping. To investigate the impact of ruthenium doping, a study on CO_2 reduction was carried out using photoelectrochemical and photocatalytic methods. The nanosheets exhibited higher photocatalytic CO_2 reduction activity. The main products obtained were methanol and ethanol. The findings presented in this study will shed light on the tremendous potential of ultrathin 2D layered Dion-Jacobson type perovskite oxide $KCa_2Nb_3O_{10}$ with single-site ruthenium doping as a promising photocatalyst for CO_2 reduction. This thesis holds significant implications for developing sustainable strategies to combat CO_2 emissions and foster a greener future.

ÖZETÇE

$KCa_2Nb_3O_{10}$ Katmanlı Perovskit Üzerinde Fotokatalitik CO_2 İndirgeme ve Su Ayrıştırma için Katkılama Stratejileri

Malzeme Bilimi ve Mühendisliği, Doktora 6

Aralık, 2023

Küresel ısınma, önceden sanayi öncesi dönemden bu yana gözlemlenen Dünya'nın yüzeyinin uzun vadeli ısınması olarak tanımlanır. Bu fenomen, başta fosil yakıt kullanımı olmak üzere insan faaliyetlerine dayanmakta ve artan dünya nüfusu ve endüstrileşme gibi çeşitli sonuçlarla birlikte atmosferde yükselen sera gazı seviyeleri ve yeşil alanlarda azalma gibi bir dizi etkiyi beraberinde getirmektedir. Dünyanın en kritik sorunu olan küresel ısınmanın ve buna bağlı iklim değişikliğinin negatif etkileri, her geçen gün daha da ciddi bir sorun haline gelmektedir. Araştırmacılar ve endüstri, CO_2 emisyonlarını azaltma zorluğuyla başa çıkmak için iki temel yaklaşımı benimsemektedir. Öncelikle, üretim düzeyindeki CO_2 emisyon sorunlarına çözüm bulma amacıyla, fosil yakıtlara olan bağımlılığı azaltmak ve hidrojen enerjisi gibi alternatif enerji kaynaklarını araştırmak hedeflenmektedir. İkinci yol ise CO_2'yi yararlı ürünlere dönüştürmektir. Son zamanlarda, fotokataliz, çevre dostu olması, daha basit kurulum, daha maliyet etkin ve daha ölçeklenebilir olma gibi özellikleri nedeniyle CO_2'yi indirgeme ve sudan H_2 üretme konularında popülerlik kazanmıştır.

Ancak, fotokataliz sistemleri hakkında daha fazla araştırma yapılması gerekmektedir. Fotokatalitik aktiviteyi artırmak için delik tutucuların kullanılması yaygın bir uygulama olmuştur, ancak perovskit fotokatalizörlerin 2D nanokatmanlarında delik tutucuların davranışı henüz keşfedilmemiştir. Fotokatalitik aktiviteyi artırmak için başka bir yol, fotokatalizörün yüzeyine yardımcı katalizör parçacıkları yerleştirmektir. Parçacıklar yüzeyde bulunduğundan, yalnızca yüzey atomları fotokatalitik reaksiyonlara etkin bir şekilde katılırken, iç atomların etkin olmaması, özellikle nüfuzlu metalleri içeren yardımcı katalizör parçacıklarının sürdürülebilirliği endişe kaynağı olabilir. Bu nedenle, bir fotokatalitik sistemin içinde tek atomlu yardımcı katalizörleri, yapı içinde dağıtmak önemlidir.

İlk bölüm olan delik tutucu çalışması, 2D katmanlı $KCa_2Nb_3O_{10}$ perovskit oksit nanokatmanları üzerinde, delik tutucuların fotokatalitik performansa etkisini mekanistik olarak incelemeyi amaçlamaktadır. Delik tutucular fotokatalitik sistemdeki, taşıyıcı dinamiklerini ve genel fotokatalitik verimliliği nasıl etkilediklerini gözlemlemek için kullanılmıştır. $[Ca_2Nb_3O_{10}]^-$ perovskit nanokatman üzerinde delik tutucuların davranışını analiz etmek için fotoelektrokimyasal ve fotokatalitik deneyler yapılmıştır.

İkinci bölüm, tek atom soy metal katkılı 2D katmanlı perovskitlerin fotokatalitik hidrojen üretim reaksiyonları için incelenmesidir. Tek atomlu soy metal katkılaması için soy metal olarak paladyum seçilmiştir. Pd'nin tek atomlu bir katkı maddesi olarak eklenmesi, fotokatalizörün elektriksel bant yapısını değiştirdiği gözlemlenmiştir. Bu, katkılama konsantrasyonuna bağlı olarak band aralığının daralmasına veya görünür spektruma kaymasını sağlamıştır. Ayrıca, fotokatalitik reaksiyonlar için aktif bir bölge olarak hizmet ederek, taşıyıcı yüklerinin transferini kolaylaştırmıştır. Pd katkısı, elektron-delik çiftlerinin rekombinasyon hızını azaltarak ve ek reaksiyon yolları sağlayarak, daha verimli bir yük kullanımı sağlamıştır.

Son bölümde, tek atom rutenyum katkılı 2D katmanlı Dion-Jacobson tipi perovskit oksit $KCa_2Nb_3O_{10}$ kullanılarak fotokatalitik CO_2 indirgeme performansları ve fotokatalitik aktiviteler incelenmiştir. Ruthenium katkılamanın etkisini görmek için, fotoelektrokimyasal ve fotokatalitik olarak CO_2 indirgenmesi incelemesi yapılmıştır. Fotokatalitik CO_2 indirgenme aktivitesinin nanokatmanlı örneklerde daha yüksek olduğu gözlemlenmiştir. Ana ürün olarak methanol ve ethanol elde edilmiştir. Bu çalışmada elde edilen bulgular, tek atom rutenyum katkılı 2D katmanlı Dion-Jacobson tipi perovskit oksit $KCa_2Nb_3O_{10}$ fazının, CO_2 indirgeme için umut vaat eden bir fotokatalizör olarak potansiyelini ortaya koymaktadır. Bu tez, CO_2 emisyonlarıyla mücadele etmek ve daha yeşil bir gelecek oluşturmak için sürdürülebilir stratejiler geliştirmek adına önemli sonuçlar taşımaktadır.

ACKNOWLEDGMENTS

I extend my deepest appreciation to my advisor, Assoc. Prof. Uğur Ünal, whose vast knowledge and guidance have shaped my academic journey. His mentorship has been a beacon of inspiration, and I am proud to have learned from someone with such profound expertise and dedication. In my opinion, a competent, visionary, and supportive advisor is crucial for a successful and at the same time enjoyable PhD experience, but they are rare to come by. Therefore, I consider myself fortunate to have the opportunity to work with an exceptional mentor like him. I hold immense respect for him, not only as a mentor but as a role model in the academic realm. I am deeply grateful to him for generously providing me the opportunity to work in his lab, sharing his wealth of knowledge, placing trust in me, and consistently offering unwavering support.

I would like to sincerely thank my jury members, Assoc. Prof. Sarp Kaya, Assoc. Prof. Ferdi Karadaş, Assoc. Prof. Mustafa Kemal Bayazıt and Asst. Prof. Safacan Kölemen. Their insightful comments and feedback throughout my thesis have been invaluable in helping me to improve my thesis.

I am immensely grateful for the unwavering support and invaluable contributions of my dear lab mates Gizem Kanat, Armin Asghari Alamdari, Hossein Mahdavi, Ali Berk Demir and Ceren Ünver throughout my Ph.D. journey. Their friendship and assistance have been instrumental in overcoming challenges and achieving milestones. Together, we formed an indomitable team, and their encouragement provided the motivation needed to navigate the complexities of research and academia. I was blessed to be able to enjoy my work in the laboratory with all these friends with whom I was on the same page. I am thankful to each and every one of them, it was very valuable for me to share our great moments, to motivate each other in our low mood moments and to be a real team. I hope our roads will cross somehow in the future again.

I would like to express my gratitude to my dear friends Asım Önal and Ghazaleh Azizi Saadatlou who hold a special place in my heart. I would like to mention that they have been with me through the hard times, also shared my happiness, and they have been with me through it all. Thank you for your unwavering support, friendship, and the countless enjoyable moments we have shared. I am very grateful to them for their constant support and for the memories that we have made together, filled with laughter, and look forward

to creating new ones together.

Also, I would like to thank AliReza Nazarahi and Hüseyin Can Özdemir, with whom I had the pleasure of working during my PhD. I am grateful for their hard work and valued friendship.

I would like to especially thank all the members of KUTEM, FunTech and SarpKayaLab for their kindness in not turning down any of my requests for support and for their wonderful friendship. I will always remember them with whom I connected on the same frequency.

I would like to thank Dr. Barış Yağcı and Dr. Hadi Jahangiri for their support with the facilities of KUYTAM (Koç University Surface Science and Technology Center). I greatly appreciate Dr. Annamaria Miko and Dr. Pınar Tatar Güner for teaching me how to teach and evaluate students. I have learned so much during my TA studies with them. I had the chance to work as a TA for 6 semesters with Dr. Annamaria Miko. Observing her work and vision gave me a new perspective. I would like to especially thank Dr. Annamaria Miko for always being there for me with both her knowledge and experience and for supporting me.

I would especially like to thank to my invaluable family. I am grateful to my mother Gülten Yılmaz and my father Ahmet Yılmaz, my biggest supporters in life, for all their efforts, love and all the values they taught me about life. I would like to thank them very much for giving me the greatest support throughout my entire education life. Their sacrifices and encouragement sustained me through the highs and lows of the Ph.D. journey. Their belief in my abilities fueled my perseverance, and I am deeply thankful for the love and strength they provided. I would also like to thank my beautiful cat Nero, the youngest member of our family, who has brought joy and happiness to my life. I hope everyone is lucky enough to meet that furry friend one day that can change their life for the better.

This thesis was supported by The Scientific and Technological Research Council of Turkey (TUBITAK) 1001 project (The Scientific and Technological Research Projects Funding Program) entitled ‘’2D nanosheets of layered perovskites for photocatalytic CO_2 reduction reactions’’ with project number 118Z865. I would like to thank TUBITAK for their support.

TABLE OF CONTENTS

LIST OF TABLES

LIST OF FIGURES

ABBREVIATIONS

KCNO	$KCa_2Nb_3O_{10}$
HCNO	$HCa_2Nb_3O_{10}$
CNO^-	$[Ca_2Nb_3O_{10}]^-$
NS	Nanosheet
CV	Cyclic Voltammetry
LSV	Linear Sweep Voltammetry
CA	Chronoamperometry
IPA	Isopropyl Alcohol
MeOH	Methanol
EDTA-Na_2	Ethylenediaminetetraacetic Acid, Disodium Salt
PEI	Polyethylenimine
HER	Hydrogen Evolution Reaction
CO_2RR	Carbondioxide Reduction Reaction
SCE	Saturated Calomel Electrode
NHE	Normal Hydrogen Electrode
DJ	Dion Jacobson
RP	Ruddlesden Popper
CB	Conduction Band
VB	Valence Band

CHAPTER 1: INTRODUCTION

1.1 Introduction

Global warming is caused by human activities, especially the widespread use of fossil fuels such as coal, oil, and gas, as well as the gradual decrease in green areas. The world has faced many problems caused by the rapidly increasing population and, accordingly, the significantly developed industrialization.

The fundamental principle of global warming revolves around the balance of radiation energy. The sun emits energy that warms the Earth's surface, and the Earth and its atmosphere radiate thermal energy back into space. On average, these two energy streams must be in equilibrium [1]. However, the presence of greenhouse gases in the atmosphere disrupts this balance by absorbing thermal radiation from the Earth's surface. They act as a "blanket" over the Earth, preventing some of this radiation from escaping into space [2]. The greenhouse effect is named after the way a greenhouse's glass allows visible light to pass through while absorbing infrared radiation. If human activities increase greenhouse gas concentrations, this radiation balance is altered, and as a result, the Earth's surface temperature rises [3]. Today, the world's expanding population and the rise of industries, along with the gradual reduction of green spaces and the release of greenhouse gases, result in a gradual rise in atmospheric CO_2 levels and the creation of a significant carbon footprint [4]. Consequently, the most significant contemporary climate challenge, global warming, is intensifying, causing an increase in Earth's average temperature.

To stabilize and even reduce CO_2 concentrations in the atmosphere, the world needs to achieve net-zero emissions. This necessitates significant and rapid reductions in emissions. The report for 2022 given in Figure 1.1 provides country-specific data on emissions from fossil fuel use and industrial sources. As seen from this graph, emissions are increasing rapidly. As a result, in addition to increasing greenhouse gas emissions, it also led to the release of approximately 37.5 Gt of carbon dioxide into the atmosphere annually.

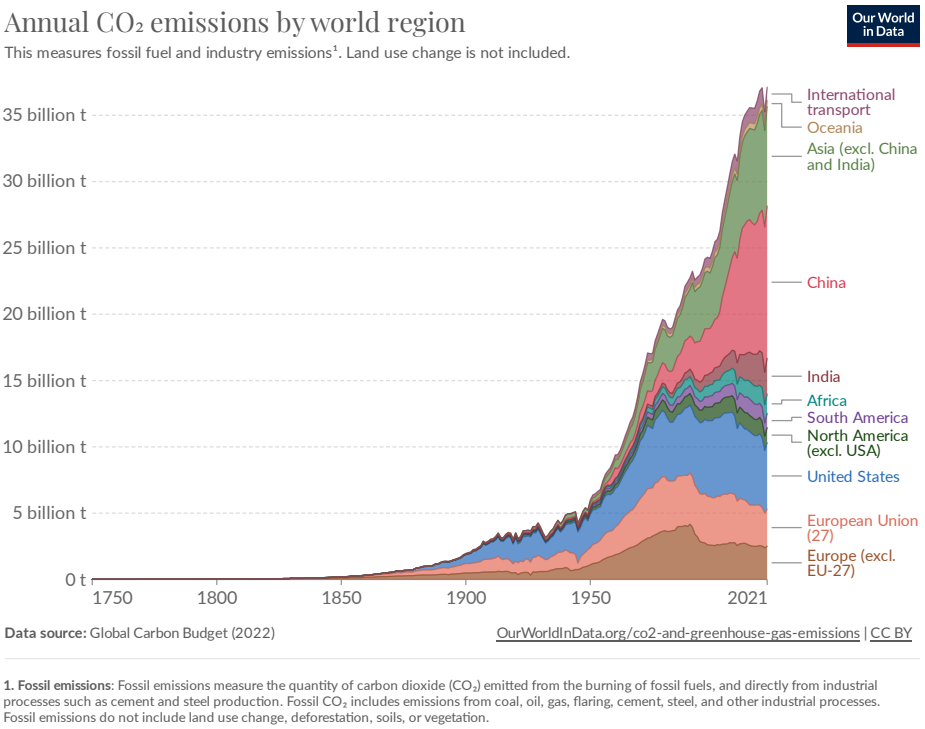

Figure 1.1: Annual CO_2 emissions by region [5] (Source: Our World Data based on the global Carbon Project (2023). Note: fossil fuel and industry emissions. Land use change is not included.)

In Figure 1.2, a comparison is presented between the current climate and energy policies and a world without climate policies. According to the graph, if no climate policies are implemented an increase of 4.1-4.8 degrees is projected. Even if current policies are maintained, temperatures are expected to rise by 2.5-2.9 degrees. Hence, to avoid these scenarios, it's crucial to transition to clean energy sources, which can help lower the level of CO_2 in the atmosphere or, at the very least, maintain it at acceptable levels.

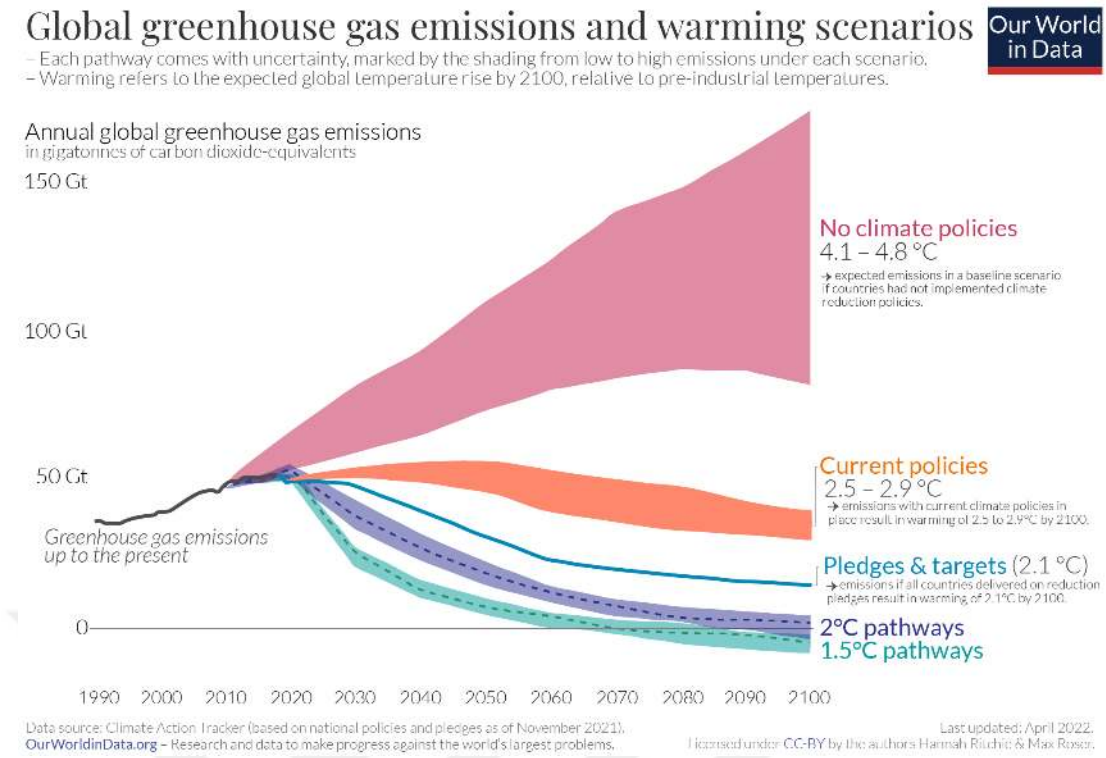

Figure 1.2: Global Greenhouse Gas Emission and warming scenarios [5].

Global climate policies, which started with the United Nations Framework Convention on Climate Change (UNFCCC), expanded with the Kyoto Protocol, and took its final form with the Paris Climate Agreement, aim to reduce carbon emissions by reducing fossil fuel use (Figure 1.3).

Figure 1.3: Global Climate Change Policies [6]

The Paris Agreement, adopted in 2015, is an important international agreement aimed at combating climate change. This aims to limit the rise in global temperatures to 2 degrees and keep it below 1.5 degrees if possible [7]. The Paris Agreement emphasizes the importance of both mitigation (reducing emissions) and adaptation (adapting to the effects of climate change) measures [8]. It also promotes financial and technological

support to help developing countries transition to more sustainable, low-carbon economies. The agreement emphasizes the need for global cooperation in combating climate change.

1.2 Classification of Energy sources

Energy resources can be classified into two categories based on their utilization and convertibility. Based on their utilization, energy resources are categorized as renewable and non-renewable energy sources. Simultaneously, with respect to their manner of origination, they are equally categorized into renewable and non-renewable energy resources. Non-renewable energy is defined as exhaustible energy sources. These resources encompass reserves with finite capacities, incapable of renewal once fully depleted. Notable examples in this category include fossil fuels like coal, lignite, gasoline, natural gas, and oil, nuclear energy. In contrast, renewable (inexhaustible) energy sources are characterized as self-renewing resources capable of persisting without depletion over an extended timeframe. Globally, these resources are widely embraced and encompass. Within the convertibility of energy resources, a further distinction is made, delineating them as either primary or secondary. Primary energy sources are those directly harnessed from natural sources, without undergoing any energy transformation. Hence, they are often referred to as natural energy resources. This category encompasses both renewable and non-renewable energy sources. While primary energies can be directly utilized, they may also undergo conversion processes to yield other energy forms. The energy derived from the conversion of primary energy is defined as secondary energy. Notable examples of secondary energy sources include gasoline, electricity, coke, diesel, secondary coal, diesel, air gas, and liquefied petroleum gas (LPG).

This classification of energy resources, founded on considerations of sustainability and their roles within primary and secondary energy systems, assumes a pivotal role in shaping energy policies and strategies. It underscores the intricate balance between the utilization of finite, non-renewable resources, and the imperative shift towards harnessing sustainable, renewable alternatives.

In Figure 1.4, each fuel source showing annual gross world energy consumption is displayed. Recent assessments reveal an increase in renewable energy sources such as solar and wind; however, they also underscore the ongoing heavy reliance on fossil fuels

for the world's energy needs. Fossil fuels maintain an 79.6% share of total primary energy consumption.

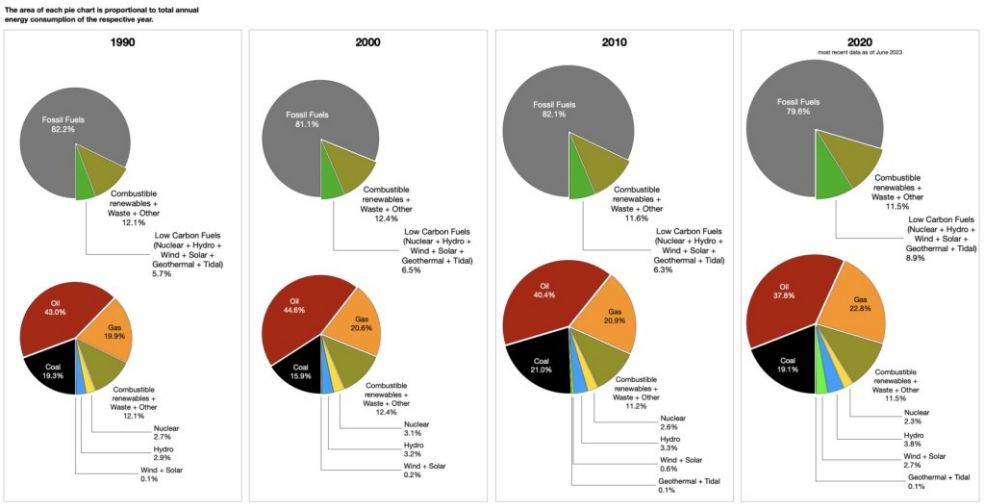

Figure 1.4: Annual gross world energy consumption (i.e final energy) by share [9].

The negative effects of global warming and related climate changes, which are the most critical problem in the world, are becoming more evident day by day. Increasing temperatures, melting glaciers and loss of valuable biological diversity, the increasing amount of greenhouse gases in the atmosphere and the damage to the ozone layer caused by CO_2 gas are indicators that decisive action must be taken urgently. The preservation of ecosystems, many of which are highly sensitive to temperature fluctuations, is another benefit of CO_2 reduction. By preventing abrupt temperature shifts, natural habitats can be conserved, species loss can be mitigated, and ecosystem disruption can be prevented.

There are two questions to be asked at this point. First, what can be done for the future and what can be done today. If we consider the question in terms of long term and short term, it will be examined in two separate ways: the adoption of clean energy as a solution for the future (long term solution) and the conversion of the present CO_2 which is increasing day by day (short-term solution).

1.3 As the Clean Energy of the Future: Hydrogen Energy

In the face of all this, our focus is shifting to sustainable solutions that can help us reduce the devastating effects of global warming. Among these solutions, hydrogen energy stands out as a ray of hope. hydrogen energy is gaining momentum as a clean energy source with the potential to revolutionize the way we produce and consume energy. One of the fundamental principles of combating climate change is to reduce our

carbon footprint. By harnessing the power of hydrogen energy, we can transition from fossil fuels to a green energy environment and significantly reduce CO_2 emissions into the atmosphere.

1.3.1 Production of Hydrogen Energy

In the coming years, hydrogen is poised to emerge as one of the most promising energy sources. It is crucial to remember, however, carbon emissions of different types of hydrogen greatly depending on how it is produced and how emissions are calculated. Different producing processes can result in variable levels of emissions.

Based on the production processes made accessible by today's technology, color-coded terminology is used to distinguish various types of hydrogen.

	Terminology	Technology	Feedstock/ Electricity source	GHG footprint*
PRODUCTION VIA ELECTRICITY	Green Hydrogen	Electrolysis	Wind, Solar, Hydro, Geothermal, Tidal	Minimal
	Purple/Pink Hydrogen		Nuclear	
	Yellow Hydrogen		Mixed-origin grid energy	Medium
PRODUCTION VIA FOSSIL FUELS	Blue Hydrogen	Natural gas reforming + CCUS gasification + CCUS	Natural gas, coal	Low
	Turquoise Hydrogen	Pyrolysis	Natural gas	Solid carbon (by-product)
	Grey Hydrogen	Natural gas reforming		Medium
	Brown Hydrogen	Gasification	Brown coal (lignite)	High
	Black Hydrogen		Black coal	

**GCG footprint given as a general guide but it is accepted that each category can be higher in some cases.*

Figure 1.5: Definitions of the Hydrogen color spectrum obtained based on the footprint of hydrogen production methods.

While hydrogen is a transparent gas, these designations have grown popular as a convenient shorthand given in Figure 1.5 [10], and their meanings are explained below[11]:

1. black-brown (from coal),
2. gray (hydrocarbons without carbon capture and storage [CCS]),
3. blue (hydrocarbons with CCS),
4. turquoise (pyrolysis),

5. pink (nuclear powered electricity),
6. yellow (solar energy),
7. red (high-temperature catalytic process),
8. white (naturally-occurring geological hydrogen) and
9. green (clean RE electricity)

Black hydrogen is created by generating hydrogen from black coal, often through a gasification process. Brown hydrogen, on the other hand, is produced by gasifying lignite, which is brown coal. It is regarded as the least environmentally friendly technique of producing hydrogen, emitting the same amount of CO_2 as direct combustion of the source fuel [12]. Grey hydrogen is produced using technologies that rely on fossil fuels such as natural gas or coal by steam methane reforming. It is not environmentally friendly because it emits carbon dioxide during production [13]. Blue hydrogen, similarly, grey hydrogen, is produced using fossil fuels by steam methane reforming. However, that process contains equipment to capture and store carbon emissions in a Carbon Capture, Usage and Storage (CCUS) system e.g., making it slightly cleaner [14]. Turquoise hydrogen is produced through high-temperature procedures and is conventionally energized by renewable sources such as solar or wind. It is cleaner than grey or blue hydrogen [15]. Pink hydrogen is obtained via the electrolysis powered by nuclear power. This process is currently costly [16]. Yellow hydrogen is created using nuclear energy to power the electrolysis process. While it is environmentally friendly, it does pose concerns about nuclear safety and waste management [14]. Red hydrogen is produced via high-temperature catalytic splitting of water with nuclear thermal power as a source of energy [12]. It refers to naturally occurring or geologically formed hydrogen that is kept in natural deposits [17].

Green hydrogen is the cleanest appearance of the available forms. It is precisely produced using water electrolysis using electricity derived from sustainable sources. Importantly, its manufacture produces no carbon emissions, showing its persistent commitment to environmental integrity [18].

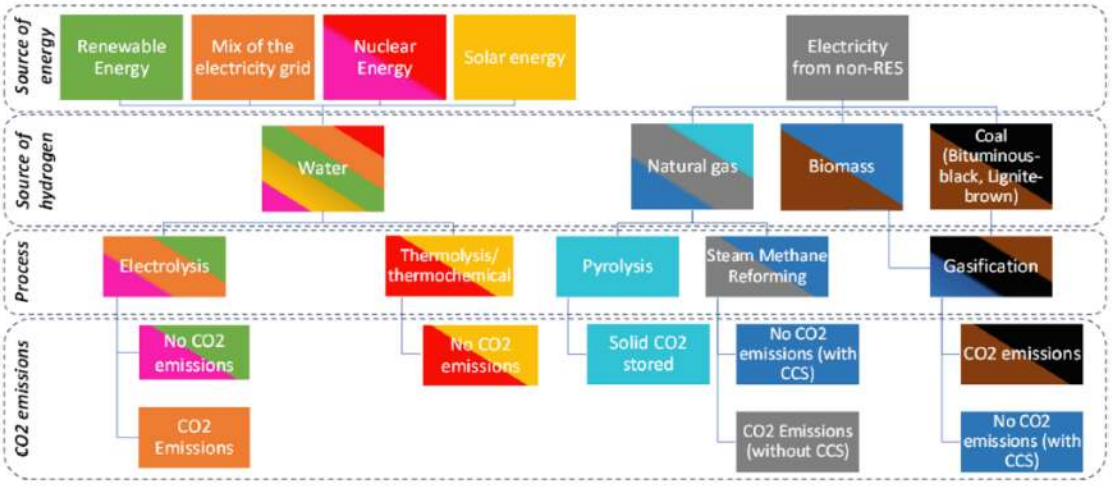

Figure 1.6: Summary of the sources of energy and hydrogen atoms, the process of production and emissions associated with the following proposed colors to refer to hydrogen: green, orange, red, pink, blue, gray, turquoise, brown, black, and yellow [19].

Figure 1.6 shows a summary of the energy and hydrogen atom sources, production processes, and emissions related with the following proposed hydrogen color-codes. The color-coded hydrogen production strategies have been discussed. Nevertheless, when long-term sustainability and environmental implications are considered, green hydrogen truly shines. Green hydrogen, obtained from renewable energy sources such as wind, solar, or hydropower, is clearly critical for achieving a cleaner, more environmentally sustainable energy future. Its carbon-neutral manufacturing technique positions it as a keystone in the battle against climate change and the transition to an ecologically sound energy landscape. Moreover, the diminishing costs associated with renewable energy sources are bolstering the competitiveness of green hydrogen [13], [15], [18].

Green hydrogen is generated using renewable energy sources through water thermolysis (thermal energy), photolysis (photon energy), and electrolysis (electrical energy) techniques, resulting in zero carbon emissions[20]–[24] . Water electrolysis powered by wind, solar, or other renewables is a more developed and widely utilized green hydrogen production process [25]. Photocatalytic water splitting stands out as a novel and environmentally friendly way of producing green hydrogen. As a result, it is a viable and feasible method for producing green hydrogen [26].

Photocatalytic water splitting uses light energy to facilitate the separation of water molecules into hydrogen and oxygen at the catalyst surface. This demands the acquisition

of suitable semiconductor materials as well as the creation of highly efficient photocatalysts.

1.3.2 Mechanism of Photocatalytic Water Splitting

In general, the process of photocatalytic water splitting involves three main steps. Here is a step-by-step overview of the working principle:

(1) When light is absorbed by semiconductor photocatalysts, electron (e-) and hole (h+) pairs are produced.

(2) Charge separation and migration to the surface of semiconductor photocatalysts

(3) Surface redox reactions: Reduction and oxidation of water.

The electronic structure of semiconductor photocatalysts generally consists of a conduction band, a valence band, and a band gap separates them. Photocatalytic water splitting mechanism is given in Figure 1.7. When the light interacts with the semiconductor photocatalyst, it is adsorbed by the semiconductor. If the energy of the photon is equal to or greater than the band gap, the electrons in the valence band will move to the conduction band, resulting in the formation of electron-hole pairs. The electrons in the conduction band (CB) participate in the reduction reaction to produce H_2, while the oxidation reaction is also carried out by the holes in the valence band (VB). For these reactions to occur, the minimum band edge of CB must be more negative than the redox potential of H^+/H_2 (0 V vs. RHE), while the maximum band edge of VB must be more negative than the redox potential of O_2/H_2O (1.23 V vs. RHE) should be more positive [27].

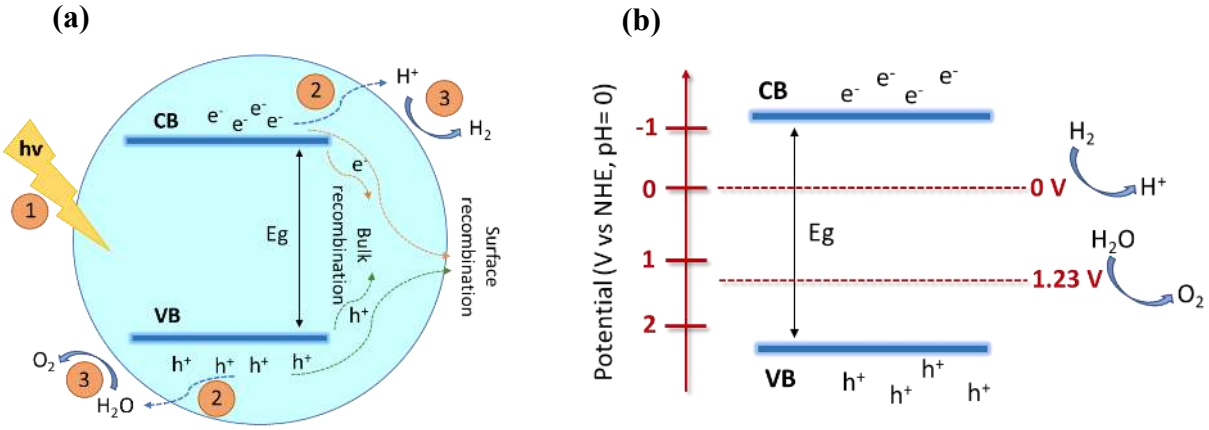

Figure 1.7: (a) Photocatalytic water splitting mechanism steps and (b) schematic diagram for water splitting photocatalyzed by a semiconductor with an aqueous redox mediator.

1.4 CO_2 Conversion

The significance of transitioning to clean energy sources as a future-oriented solution has been examined above. Additionally, in answer to the question of what can be done today, it is evident that efforts to conversion the existing CO_2 in the atmosphere hold paramount importance [28], [29]. CO_2 conversion methods can be grouped into four main categories as follows:

- Catalytic Conversion
    - Photocatalytic
    - Electrocatalytic
    - Thermocatalytic
- Electrochemical
- Mineralization
- Biological
- Copolymerization

Catalytic conversion is the employment of catalysts to convert heavy hydrocarbons, chemicals, or fuels to useful products such as light hydrocarbons, chemicals, or fuels. Catalytic conversion of CO_2 involves three fundamental methodologies: thermocatalytic, photocatalytic, and electrocatalytic [30]. Thermocatalytic conversion uses high temperatures in combination with catalysts to initiate chemical reactions that transform carbon dioxide into valuable products [31]. Photocatalytic conversion, on the other hand, employs catalysts activated by light to initiate reactions; semiconductors often serve as preferred photocatalysts [32]. This technique possesses remarkable potential for transforming CO_2 into renewable energy sources via photon energy. PhotocatalyticCO2 conversion method provides a promising and straightforward strategy to simultaneously reduce the atmospheric CO_2 level and fulfill the future energy demand. Electrocatalytic conversion engages in electrochemical reactions at the interface between the catalyst and the electrolyte, leading to the electrochemical reduction of CO_2, giving rise to a diverse range of products [33].

Electrochemical CO_2 conversion uses electric energy to drive reduction of CO_2, turning it into useful products like carbon monoxide, methane, ethylene etc which can serve as valuable intermediates for various industrial processes [34].

Mineralization is the chemical reaction that occurs between CO_2 and naturally occurring minerals, particularly magnesium and calcium silicates, to generate stable carbonates. The primary product is stable carbonate minerals [35] .

Bioconversion of CO_2 to energy involves first trapping the CO_2 within a biological system and then converting it into biofuels such as ethanol, butanol, or methane or bioenergy [36].

Copolymerization involves incorporating CO_2 as a monomer into polymer chains to generate CO_2-based polymers during the polymerization process. These polymers offer eco-friendly substitutes for plastics, foams, and coatings, thereby reducing the carbon footprint of polymer manufacturing [37] .

1.4.1 Photocatalytic CO_2 conversion

Photochemical reduction stands out as a highly encouraging approach to CO_2 conversion in terms of environmental sustainability and renewable compared to other CO_2 conversion methods. It uses solar energy to drive chemical reactions, potentially capturing and using CO_2 while eliminating the need for fossil fuels. Moreover, solar energy is both environmentally friendly and a renewable resource, further enhancing its appeal in this context. The photocatalytic reduction mechanism of CO_2 is a complex process that involves several intermediate steps as given in Figure 1.8.

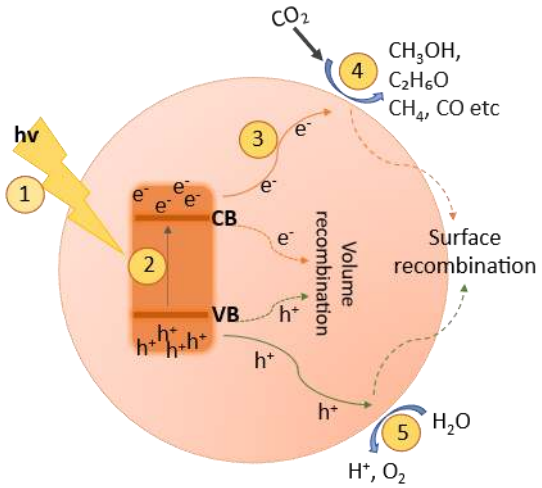

Figure 1.8: Schematic representation of the five fundamental steps in photocatalytic CO_2 reduction.

These steps can be listed as follows:

1. **Photon Absorption**: Photocatalysis begins with the absorption of photons (light) by the photocatalyst material.
2. **Generation of Electron-Hole Pairs**: The energy from the photons excites electrons in the valence band and them from the valence band to the conduction band. The excited electrons in the conduction band and the resulting electron holes in the valence band create electron-hole pairs.
3. **CO_2 Adsorption and Photocatalytic Reduction**: CO_2 molecules from the surrounding atmosphere or solution are adsorbed onto the surface of the photocatalyst. The excited electrons in the conduction band goes to the surface to interact with CO_2 and participate in reduction reactions.
4. **Product Formation**: The reduced CO_2 molecules to form CO, methane (CH_4), or other carbon-based products, depending on the reaction conditions and the specific photocatalyst used.
5. **Water Oxidation:** Simultaneously, the electron holes participate in water oxidation reactions by to release molecular oxygen and H^+ is evolved as a byproduct.

Semiconductor materials are the preferred choice for photocatalytic energy conversion due to their specific properties. The band gap inherent in semiconductors allows them to absorb light, initiating the creation of electron–hole pairs essential for photocatalytic energy conversion reactions. The redox properties of semiconductors further enhance their versatility, allowing them to engage in a wide array of reduction and oxidation reactions. Semiconductor materials serve as catalysts for numerous applications, such as the water splitting, decomposition of pollutants [38], CO_2 reduction reactions [39] and production of advantageous chemicals on reaction surfaces.

Their compatibility with the solar spectrum positions them as key players in converting solar energy into chemical energy, contributing significantly to the production of renewable energy. However, certain factors must be mentioned, which adversely affect the efficiency of the photocatalytic reaction, despite its numerous advantages.

Several factors including the photocatalyst material's band gap energy, stability, surface area and charge carrier mobility should be considered. Additionally, parameters

such as the wavelength and intensity of light source, temperature, and pH value are also important. Furthermore, the e-h recombination issue remains a significant challenge to overcome. In photocatalytic systems, electron-hole recombination refers to the recombination of photogenerated electrons (e^-) in the conduction band and photogenerated holes (h^+) in the valence band of a semiconductor photocatalyst. This recombination causes a loss of charge carriers and prevents the energy from the initially absorbed photon from being utilized in desired chemical reactions, resulting in reduced efficiency of photocatalytic energy conversion.

Two-dimensional layered materials lead the way in semiconductors for photocatalytic energy conversion, possessing a unique array of properties that enhance their catalytic abilities [40], [41]. With their atomically thin structure a large surface area, which increases the density of active sites for photocatalysis [42]. The tunable band structures achievable through layer manipulation or chemical functionalization, allows for precise control over light absorption, rendering them versatile and adaptable to specific wavelengths [43], and their charge transport properties expedite electron-hole pair separation [44], ensuring high efficiency. Notably, the fast charge carrier mobility inherent in 2D materials minimizes electron–hole recombination, ensuring efficient charge transfer during photocatalysis [45]. Moreover, 2D layered materials are favored for applications in photocatalytic energy conversion as including atomic thinness, high electron mobility and conductivity, and a shortened diffusion path length by decreasing photo-induced bulk recombination [46].

1.5 Major Categories of Semiconductor Photocatalysts

In the literature, various inorganic (Metal Oxides, Layered Perovskites, Transition Metal Chalcogenides (TMDCs), MXene, Hexagonal Boron Nitride (h-BN), Black Phosphorus, Sulfide photocatalysts such as CdS, ZnS, $ZnIn_2S_4$; nitrides like Ta_3N_5, $LaTaON_2$ and complex oxides with layers like $K_2La_2Ti_3O_{10}$, $K_4Nb_6O_{17}$, $KCa_2Nb_3O_{10}$), and organic (g-C_3N_4, Metal-Organic Frameworks (MOFs), etc.) photocatalysts are used in photocatalytic energy conversion applications.

MOFs have recently gained recognition as potential materials for various applications such as gas adsorption and separation, sensors, gas storage, and (photo)catalysis. MOFs consist of transition metals (Fe, Co, Mn, Ni, Cu) bonded to organic ligands containing elements like C, H, O, N, S, etc. [47]. Due to the properties of

MOFs, permanent crystalline structures, high surface area, low density and significant porosity, MOFs act as effective electrocatalyst and photocatalysts, enhancing charge and mass transport[48]. The integration of different molecular components allows versatile property modulation, making MOFs valuable in catalysis and beyond [49]–[51].

A wide range of g-C_3N_4 based photocatalysts have been developed to drive various reduction and oxidation reactions under light irradiation at appropriate wavelengths due to their unique physicochemical, optical, and electrical properties [52], [53]. After the discovery of g-C_3N_4-based photocatalysts by Wang et. al. in 2009 [54], g-C_3N_4-based nanostructures have been used as ideal candidates for various energy and environmental photocatalytic applications, such as photocatalytic water reduction and oxidation [55]–[57], pollutant degradation and carbon dioxide reduction [58]–[60].

MXenes have become one of the interesting classes of 2D materials that can be used in electrocatalytic and photocatalytic energy conversion reactions [61]–[65] after their discovery by Naguib et al. in 2011 [66]. It can be said that they have recently started to be used in the field of CO_2 reduction [67] and have gained popularity among the 2D layered materials. They are formulated as $M_{n+1}X_nTz$ (n = 1–3), with M representing Ti, Sc, Nb, Ta, Cr, Mo, Zr, Hf, and V [63].

Oxide-based semiconductors are favorable contenders for photocatalytic applications due to their light absorption and charge transfer properties, as well as their suitable optical and electronic structures. ZnO, TiO_2, CdS, WO_3, Cu2O, ZnS, and $SrTiO_3$ are extensively employed as photocatalysts in the literature due to their stability and appropriate band structure [68], [69]. The wurtzite phase of zinc oxide (ZnO) [70]–[72] and the anatase phase of titanium dioxide (TiO_2) [73], [74] are the most frequently used metal oxide photocatalysts due to their electronic band structure and appropriate photocatalytic properties.

Layered perovskites possess a unique structure, with individual layers separated by structural units. This layered arrangement offers the potential to adjust the material's properties and functions. For instance, the ability to vary the band gap is imperative for enhancing light absorption in the solar spectrum, which plays a crucial role in photocatalytic processes. Layered perovskites can typically be synthesized using simple techniques, enabling affordable manufacturing and scale-up opportunities that are significant for potential industrial applications. The stratified arrangement facilitates the

efficient separation of electron-hole pairs generated by light absorption, which is a crucial step in achieving efficient photocatalysis. This separation averts immediate charge recombination, permitting their involvement in redox reactions.

The structure and composition of layered perovskites can be customized to satisfy the specific needs of various photocatalytic reactions. This allows researchers to design materials with optimal properties for energy conversion processes.

Layered perovskites consist of two-dimensional perovskite metal oxide layers held together by cations or cationic groups, as shown in Figure 1.9. The cations or cationic structures between the layers balance the negative charge of the perovskite metal oxide layer. Layered oxides can generally be classified as Ruddlesden-Popper ($A_{(n-1)}B_nO_{3n+1}$), Dion-Jacobson ($A'[A_{(n-1)}B_nO_{3(n+1)}]$), and Aurivillius ($A_{(n-1)}Bi_2B_nO_{3n+3}$) phases.

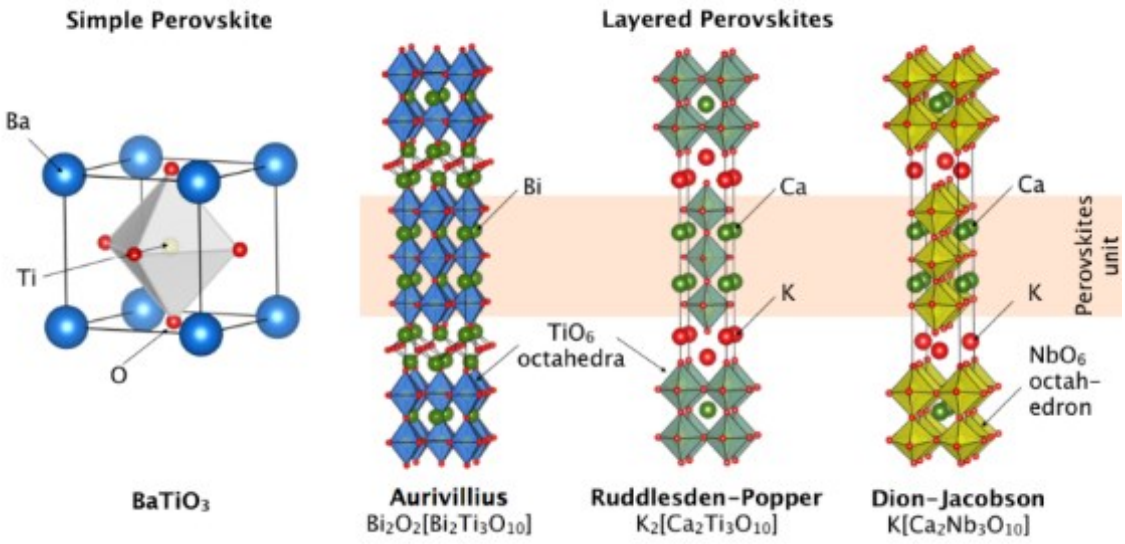

Figure 1.9: Structure of simple perovskite and layered perovskites types as named Aurivillius, Ruddlesden-Popper and Dion-Jacobson phases [75].

The Ruddlesden-Popper phase consists of two-dimensional perovskite-like slabs interleaved with cation. The general formula is $A_{n+1}B_nX_{3n+1}$ can be written $A_{n-1}A'_2B_nX_{3n+1}$, where "A" represents the cations located between the perovskite layers, "B" represents the metal cations in the perovskite layers, "X" represents the anions, and "n" the number of octahedral layers in the structure. $Sr_{n+1}Ti_nO_{3n+1}$ is a well-known compound in the Ruddlesden-Popper phase.

The Aurivillius phase is another layered structure with perovskite layers separated by Bi_2O_2 layers. This phase is represented by the general formula $(Bi_2O_2)_{An-1}B_nX_{3n+1}$, where "A" represents the cations between perovskite layers, "B" represents the metal cations in the perovskite layers, "X" represents the anions, and "n" denotes the number of perovskite layers between the Bi_2O_2 layers [76]. $Bi_4Ti_3O_{12}$ (Bismuth Titanate) is a well-known compound in the Aurivillius phase.

The Dion–Jacobson phase is an A′/A cation-ordered layered perovskite with a general formula of A′ $[A_{n-1}B_nO_{3n+1}]$ (A′ = K, Cs, Rb, Li, H, Ag; A = La, Ca, Sr, Bi; and B = Ti, Nb, Ta, etc.), where n denotes the number of the corner-sharing BO6 octahedral layers, and the A′ cation separates the $A_{n-1}B_nO_{3n+1}$ perovskite layers [77]–[79]. The well-known KCa2Nb3O10 Dion Jacobson phase structure is presented in Figure 1.10 in detail.

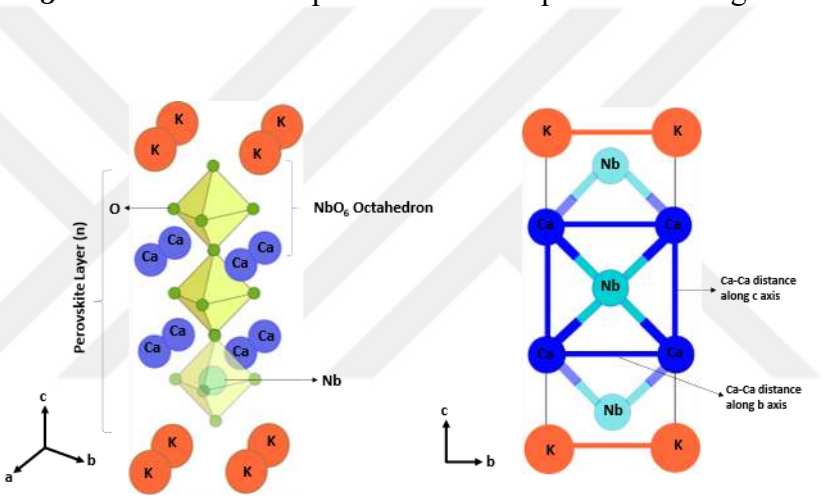

Figure 1.10: Layered perovskite oxide Dion Jacobson phase $KCa_2Nb_3O_{10}$ structure in details.

Nevertheless, the industrial application of pristine layered perovskites in photocatalytic applications remains a challenge. This is due to their wide band gaps, which restrict the absorption of visible light, and their insufficient charge separation efficiencies [80].

1.6 Methods of Enhancing Photocatalytic Activity

Many 2D layered perovskite oxides exhibit promising photocatalytic activity; however, their energy conversion efficiencies remain insufficient for application. Thus, interface engineering and materials science (specifically, the adjustment of band gaps) have the potential to improve conversion efficiency. The optical and electrical properties of these materials can be effectively modified by altering the band gap through the inclusion of dopants, surface functionalization, and thickness reduction.

Transition metals are frequently employed in photocatalytic CO_2 reduction and photocatalytic hydrogen evolution reactions due to their high stability, low cost, and high catalytic activity. Specifically, cobalt and nickel metal ions can effectively inhibit the formation of high-energy intermediates and support the multi-electron reduction of CO_2, making them preferred components in photocatalytic CO_2 reduction processes. Specifically, cobalt and nickel metal ions can effectively inhibit the formation of high-energy intermediates and support the multi-electron reduction of CO_2, making them preferred components in photocatalytic CO_2 reduction processes. It has been reported that defect engineering can alter the band structure and optical properties of semiconductor photocatalysts, thus enhancing their light absorption capacity and carrier separation efficiency.

Surface modification is one of the most effective solutions, as it can optimize the surface atomic states, surface structures and charge properties of semiconductor photocatalysts, making it a promising technology for photocatalytic reactions. Photocatalysts have been modified with valuable metals. These metals can play a replacement role and provide more catalytic active sites for the photocatalytic reduction of CO_2 and photocatalytic hydrogen evolution reactions.

Another way to improve the photocatalytic activity to use materials with different morphologies and enhance the charge separation and transfer. Recently, two-dimensional (2D) nanosheets with unique properties such as high surface area, porous structures, multiple active sites on the surface, and high crystallinity, have found wide applications in various fields such as photocatalysis, electrocatalysis, energy storage and sensors. High-surface-area, 2D structures are effective in separating and transporting light-generated electron-hole pairs to the electrode surface due to their shortened time and distance of charge transfer.

CHAPTER 2: EFFECT OF HOLE SCAVENGERS ON PHOTOCATALYTIC WATER SPLITTING

2.1 Introduction

Using semiconductor-based photocatalytic hydrogen evolution as a sustainable way to capture light energy has been significantly noticed. This strategy serves to meet the continuously growing global energy requirements, providing a promising route for generating clean energy. Photocatalytic hydrogen evolution mechanism given in Figure 2.1 and it can be briefly explained as follows: Photocatalytic processes utilize semiconductor materials that capture light energy to generate electron-hole pairs. The light energy incident on the semiconductor material (if the band gap is equal to or larger than the light energy) excites the electrons in the valence band. Excited electrons migrate from the valence band to the conduction band and participates in reduction reactions, leading to the splitting of water and subsequently resulting in the production of H_2 gas, while the positively charged holes in the valence band engage in oxidation reactions. Meanwhile, exited electrons may revert to vacancies in the valence band or in the structure, a process referred to as electron-hole recombination.

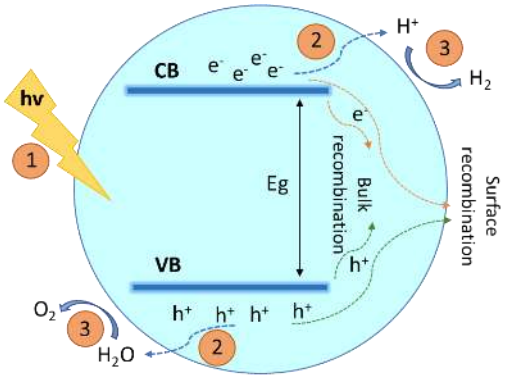

Figure 2.1: Photocatalytic Water Splitting Mechanism

Summary of water splitting mechanism in key points step by step:

Step 1: Absorption of light by photocatalyst and generation of electron (e^-) and hole (h^+) pairs

Step 2: Charge separation and migration to the surface of semiconductor photocatalysts

Step 3: Surface redox reactions: Reduction of H^+ and oxidation of water.

The efficiency of photocatalytic reactions is reduced by this undesired recombination [81]. To maximize the efficiency of photocatalytic reactions, it is essential to minimize recombination by various means, such as using co-catalyst [82]–[86], creating heterojunctions [87]–[89], employing quantum dots or nanostructures [90]–[93] and using hole scavengers [94]–[98] that promote the separation and utilization of electron-hole pairs for the desired chemical transformations. Sacrificial agents are becoming more popular due to their simplicity in application, material accessibility, and cost-effectiveness [64]. Hole scavengers work to minimize recombination by capturing and neutralizing positively charged holes prior to their recombination. The use of hole scavengers is important to enhance the catalytic efficiency during photocatalytic reactions. Hole scavengers are especially effective at capturing the photogenerated holes, thus reducing charge carrier recombination and extending the lifespan of electrons for various reactions, for example, the reduction of water to produce H_2. Alongside water splitting, the photocatalytic reduction of CO_2 is another demanding reaction which may require a hole scavenger to increase the efficiency of the photocatalytic CO_2 reduction reaction [99]–[101]. The fundamental purpose of hole scavengers is to impede the recombination of electrons and holes, a procedure which could negatively impact the total efficiency of the photocatalytic reaction. Hole scavengers retain the positively charged holes in the valence band, preventing photogenerated electrons from returning to them, and facilitating a greater proportion of active participation in the desired redox reactions [102].

Hole scavengers also known as sacrificial hole acceptor or electron donors. In the literature, many organic and inorganic hole scavengers have been reported for semiconductors to efficient photocatalytic reactions. Well-known hole scavengers are alcohols, including methanol, ethanol and isopropyl alcohol, and soluble salts (e.g. sodium formate), amines (e.g. triethanolamine) as well as ions such as iodide (I^-) or sulfide (SO_3^{2-}), certain acids (Ascorbic acid, Oxalic acid) and H_2O_2 which can conveniently accept holes and form stable products [103]–[113].

The suitability of hole scavengers for both photocatalytic water splitting, and photocatalytic CO_2 reduction reactions depends on the specific requirements and conditions of each reaction. Different redox reactions have different demands in terms

of energy levels and electron transfer kinetics. Selection of the hole scavenger often involves consideration of redox potentials, reaction kinetics, and the specific requirements of the photocatalytic system. Tailoring the hole scavenger to the targeted reaction can optimize the overall efficiency of the process.

For this, the reduction and oxidation potentials of water vs NHE at pH=7 are -0.41 V and 0.82 V respectively. In photocatalytic CO_2 reduction, CO_2 is reduced to produce valuable chemical compounds such as hydrocarbons or other carbon-based fuels. Reduction of CO_2 to various products are approximately between -0.2 and -0.65 V [114]. In Figure 2.2 is represents schematic diagram of photocatalytic reduction of CO_2.

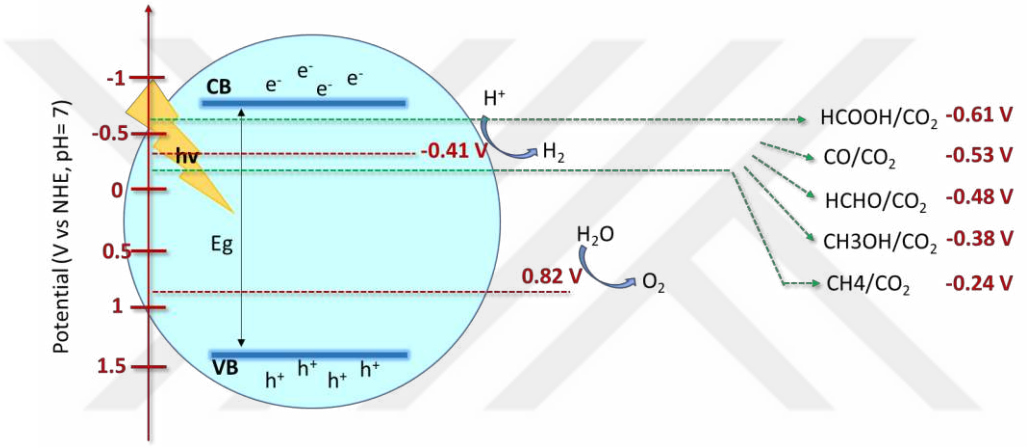

Figure 2.2: Schematic diagram of photocatalytic CO_2 reduction mechanism.

Izawa et al [94] conducted a study on the impact of methanol as a hole scavenger on photocatalytic activity with different nanosheet electrodes. The $Nb_6O_{17}^-$ and $[Ca_2Nb_3O_{10}]^-$ nanosheets exhibited the highest photooxidation current. It was demonstrated that the degree of methanol photooxidation influenced the performance of water photolysis. They reported that the highest photooxidation current on the $Nb_6O_{17}^-$ nanosheet indicated a substantial separation between electrons and holes when exposed to light. Additionally, the rate of hole capturing by methanol has been shown to be significantly faster than surface recombination in the $Nb_6O_{17}^-$ nanosheet.

Berr et al [115] employed Pt-decorated CdS nanorods as photocatalysts and examined the impact of four distinct hole scavengers: sodium sulfite (SO_2^{3-}), triethanolamine (TEOA), disodium ethylenediaminetetraacetic acid (EDTA-Na_2) and methanol (MeOH) on photocatalytic hydrogen generation. This study presents a

significant discovery for selecting a hole scavenger and comparing the performance of various photocatalytic nanosystems. The findings demonstrate that the redox potential of the hole scavengers predominantly influences the photocatalytic efficiency of hydrogen production and stability of colloidal Pt-decorated CdS nanorods. The authors reported that higher hydrogen production efficiency was observed with stronger oxidation power of the hole scavenger.

For example, Denisov et al [95] investigated effect of hole scavengers such as methanol, isopropanol, ethylene glycol, EDTA-Na_2, as well as Na_2SO_3 and H_2O_2 on photocatalytic water splitting for Pt decorated TiO_2 nanotubes used as a photoanode. The results indicate that H_2 production performance was increased by up to 28.8 times in the presence of MeOH.

In another study, Pan and Heagy [96] examined the photocatalytic reduction of bicarbonate to formate by using six different hole scavengers on Cu_2O and TiO_2. To compare, they selected hole scavengers comprising glycerol, ethylene glycol, 2-propanol, sodium sulfite, triethanolamine, and ethylenediaminetetraacetic acid. Glycerol was shown to be the most efficient h^+ scavenger for this study. They reported that TiO_2 showed the highest quantum efficiency with 5.04 ± 0.3%, according to the test performed in glycerol.

In another study, Nguyen et al.[97] performed photoreduction of graphene oxide on the surface of TiO_2 using three solvents: ethanol, isopropanol, and water under UV irradiation. The results indicated that isopropanol exhibited better scavenging behavior than ethanol.

Tahir (2023) [98] synthesized vanadium carbide (V_2C) MXene combined with exfoliated graphitic carbon nitride (ECN) for the photocatalytic conversion of CO_2. Methanol was introduced as a hole scavenger at a concentration of 5% for the photocatalytic reduction of CO_2 to CO and CH_4. Methanol was found to be highly effective as a sacrificial reagent, resulting in increased CO yield.

This study aims to mechanistically investigate the photocatalytic performance of hole scavengers on 2D layered nanosheets (NS), using $[Ca_2Nb_3O_{10}]^-$ nanosheets of 2D layered $KCa_2Nb_3O_{10}$ perovskite. A range of hole scavengers were added to the photocatalytic system to observe how they influence the charge carrier dynamics and overall photocatalytic efficiency. To analyze the behavior of hole scavengers on a single $[Ca_2Nb_3O_{10}]^-$ perovskite nanosheet, photoelectrochemical characterization techniques

were utilized. We examined various hole scavengers, including methanol, triethanolamine, ascorbic acid, and EDTA-Na_2, in K_2SO_4 electrolytes. To evaluate their impact on the behavior of the semiconductor's 2D nanosheets, we conducted cyclic voltammetry and chronoamperometry tests under chopped light. This study offers useful insights into devising and refining hole scavengers to improve $[Ca_2Nb_3O_{10}]^-$ nanosheets' photocatalytic efficacy, and these findings can also apply to a range of other photocatalysts. Additionally, this research adds to our fundamental comprehension of charge carrier dynamics in the context of photocatalytic water splitting.

2.2 Experimental

2.2.1 Materials

K_2CO_3 (ACS, 99.0% min, Alfa Aesar), $CaCO_3$ (98.5-100.5 mass%, pro analysis, Merck), Nb_2O_5 (99.9%, Sigma-Aldrich), Potassium sulfate (≥ 99.0% for analysis), Tetrabutylammonium hydroxide (~40% in water, Sigma-Aldrich), Polyethylenimine (branched average Mw ~25 000 BY LS, average Mn ~10 000 by GPC, Sigma-Aldrich), Triethanolamine (GR for analysis, Millipore Corporation), ethylene glycol (99.9%, WWR Chemicals), Ascorbic Acid (L(-) CPure, Tekkim), and Methanol (≥ 99.8% ACS Reagent). All other chemicals were of reagent grade. Milli-Q filtered ultrapure water (>18 MΩ cm) was used throughout.

2.2.2 Preparation of Photocatalyst

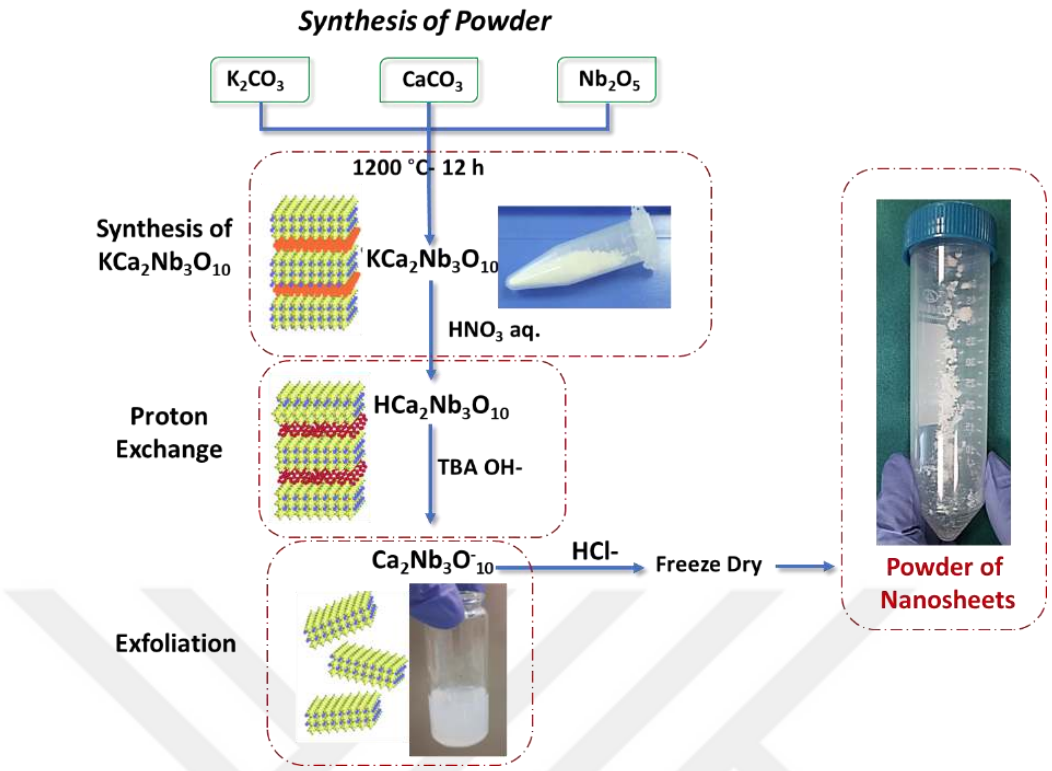

Figure 2.3: Synthesis steps of $[Ca_2Nb_3O_{10}]^-$ nanosheet powder as a photocatalyst.

Flow chart of preparation of photocatalyst is given in Figure 2.3. The layered perovskite oxide $KCa_2Nb_3O_{10}$ (KCNO) powders were prepared using analytical grade powders of $CaCO_3$, Nb_2O_5, K_2CO_3, according to the stoichiometric ratio (K/Ca/Nb= 1.2:3) as the starting materials by solid state method. Nb_2O_5 (3.572 g), $CaCO_3$ (1.792 g), and K_2CO_3 (0.618 g) were used as precursors materials. The amount of K_2CO_3 was 20 mol % (0.136 g) in excess to compensate for the loss of potassium due to volatilization during calcination. All the materials were mixed by mechanical grinding in an agate mortar for 30 minutes. The obtained powder mixture was calcined 1200 °C in air for 12 hours with a heating rate of 10° min^{-1} and cooled naturally.

The resultant powder was mixed in a solution of 5 M aqueous nitric acid and stirred for 3 days. The acid solution was replaced daily. The product was isolated by centrifugation and washed with distilled water at the end of the 3 days. Finally, protonated powder which is $HCa_2Nb_3O_{10}$ (HCNO) was obtained by drying at room temperature overnight.

In order to obtain nanosheet powders which is $[Ca_2Nb_3O_{10}]^-$ ($[CNO]^-$), these protonated powders have been separated into layers by using an exfoliation method. 40% wt Tetrabutylammonium hydroxide (TBA OH^-) aqueous solution was used for the exfoliation reaction. The OH^- and H^+ ratio was set to 1:1 for exfoliation The mixtures were subjected to shaker-assisted exfoliation at a speed of 150 rpm for 7 days, resulting

in the formation of colloidal nanosheet suspensions. The solution was left for 24 hours to allow the unexfoliated particles to precipitate, and then the top of the colloidal solution was collected. The nanosheet colloids were restacked by adding a small amount of 2.5 M aqueous hydrochloric acid. The restacked nanosheet powder was thoroughly washed with distilled water to remove any remaining traces of TBA Cl^- and HCl. After that, the powder was freeze-dried overnight.

2.3 Characterization

2.3.1 Characterization of 2D Layered Material

The composition of the phases, the crystallinity, and the purity of the $KCa_2Nb_3O_{10}$ were analyzed using the X-ray diffraction technique. XPS was used to evaluate the chemical state and describe the chemical composition of the photocatalyst. The valence band level was estimated by analyzing the valence band spectra using X-ray photoelectron spectroscopy (XPS). The band gap was determined by UV-Vis spectroscopy. Subsequently, the conduction band was derived by computational means, utilizing the obtained valence band and band gap data.

2.3.2 Film Preparation

$[CNO]^-$ nanosheets were coated onto fluorine-doped tin oxide (FTO) -coated glass used as a working electrode for photoelectrochemical experiments. The steps were followed to prepare working electrodes: FTO substrates were ultrasonically cleaned before deposition by rinsing them in intermediate water containing acetone and ethanol for ten minutes each and dried by N_2 flow. The substrates were immersed for 15 minutes in an aqueous Polyethylenimine (PEI) solution (2.5 g/L). PEI-coated FTO substrates were dipped in nanosheet colloidal solution for 15 minutes, and then they were washed with deionized water. Finally, the films were at 60°C for one hour.

2.3.3 Photoelectrochemical Experiments

To investigate the photoelectrochemical behavior, cyclic voltammetry (CV) and chronoamperometry tests were carried out. A typical three-electrode electrochemical quartz cell was used in the photoelectrochemical tests. In these experiments, $[Ca_2Nb_3O_{10}]^-$ nanosheet coated 1x1 cm^2 fluorine-doped tin oxide (FTO) films were utilized, which had been fabricated using a layer-by-layer technique. A platinum spiral wire used as the

counter electrode, a saturated calomel electrode (SCE) was employed as the reference electrode, and a 300W Xenon lamp used as the light source. The electrolytes were individually prepared using combinations formed by the individual addition of 2.5% volume methanol, 2.5% volume isopropanol, and 0.1 M Ethylene diamine tetra acetic acid disodium salt dihydrate (EDTA-Na_2) to a 0.5 M K_2SO_4 aqueous solution. Prior to the experiments, the solutions were bubbled with Argon gas for a 20-minute to eliminate dissolved oxygen.

Chronoamperometry test was carried out by chopping the light on and off for 300 seconds at a constant potential of 1.2 V vs Saturated Calomel Electrode (SCE). CV tests were recorded under light illuminations between at -0.5 V-1.4 V.

2.3.4 Photocatalytic Experiments

The photocatalytic hydrogen evolution reaction (HER) experiments were carried out in 10 mL quartz cell. 10 mg of the photocatalyst was added into 5 mL of water-hole scavenger aqueous solution include separately 2.5% volume methanol, 2.5% volume isopropanol, and 0.1 M Ethylene diamine tetra acetic acid disodium salt dihydrate (EDTA-Na_2) hole scavengers. The cell illuminated horizontally with a 300 W xenon light source (Newport, 66901) and it was stirred during the test to homogenize the catalyst. No co-catalyst was used in the experiments. To control the temperature and prevent thermal effects during the experiment, a cooling water bath was used. Prior to the start of the experiments, the solution was purged with argon gas with 20 ml/min flow for 30 min to eliminate dissolved oxygen under dark conditions. Two rubber septa have been used to ensure a tight seal, which effectively prevents any leakage of gas out of the cell. The cell was initially sealed with the first septum, followed by the placement of the second septum on top of the first. This procedure created a gap between the two septa. Throughout the experiment, argon gas was passed through this gap to prevent any possible leakage.

The hydrogen amount from the experiments were detected by a gas chromatogram (GC-2014 Shimadzu, equipped with a thermal conductivity detector (TCD), argon as a carrier gas, and 5 Å molecular sieve column. A H_2 peak was observed at a retention time of 0.8 minutes, under the following parameters of GC: The temperature of the MS 5A column (Teknokroma, NF-38427-FS) was 65 °C, the inlet temperature was 150 °C, and the temperature of the thermal conductivity detector (TCD) was 150 °C. Argon was used as a carrier gas, and the flow rate was set at 20 ml/min. A sample of the gas from the

headspace was taken using a 100 µL gas-tight syringe and it was then injected into the gas chromatograph per hour.

For the H_2 calibration of the GC, a cell with a total volume of 10 ml was prepared that contained 5 ml of water and H_2 was bubbled for 30 minutes. After that, different volumes of gas were taken using gas tight syringe and injected into GC with 10µl intervals between 10 and 100 µl. A calibration curve was obtained to convert the area of the peak into amount of hydrogen. The areas of the peaks obtained from the GC for each volume were converted to mole according to the ideal gas equation. It was accepted as 1.0 mol of gas occupying 22.4 L of volume. The headspace volume was 5 ml. The calibration curve used is plotted in Figure 2.4.

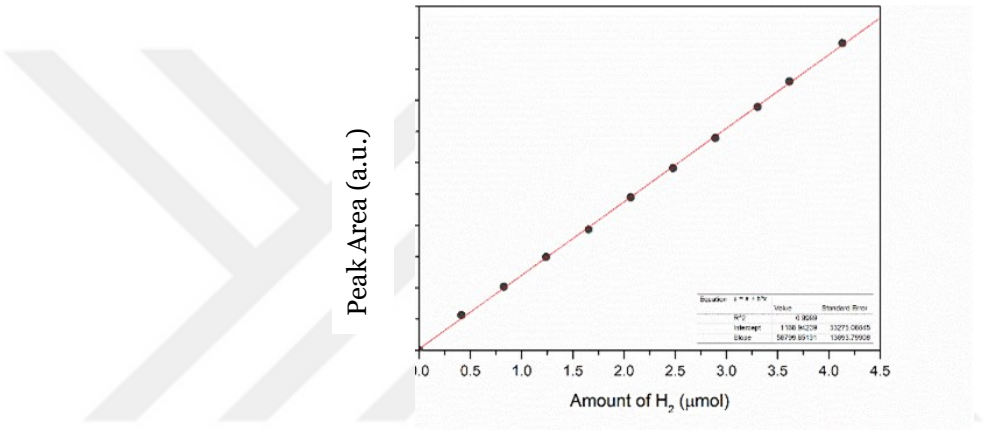

Figure 2.4: Calibration curve of H_2 showing the relationship between the amount of hydrogen injected, and the area of peak.

The area of the peak belonging to H_2 of samples injected can be converted to the actual amount of hydrogen injected into the GC from the 100 µl sample using this calibration curve.

2.4 Results and Discussion

2.4.1 Characterization of the Photocatalyst

The powder XRD patterns of the parent structure ($KCa_2Nb_3O_{10}$) and the structure after proton exchange ($HCa_2Nb_3O_{10}$) are displayed in Figure 2.5. The crystal structure of the material did not significantly change after proton exchange. The (00l) reflection peaks at the lower theta angles belong to layered materials. The distance between two adjacent layers. Reason for Replacement of H+ Ions with K^+ ions might be the XRD pattern of the $Hca_2Nb_3O_{10}$ structure shifts to lower theta angles, causing an increase in the d space

distance between the nanolayers. This occurs as a result of the replacement of H^+ ions with K^+ ions [78], [116].

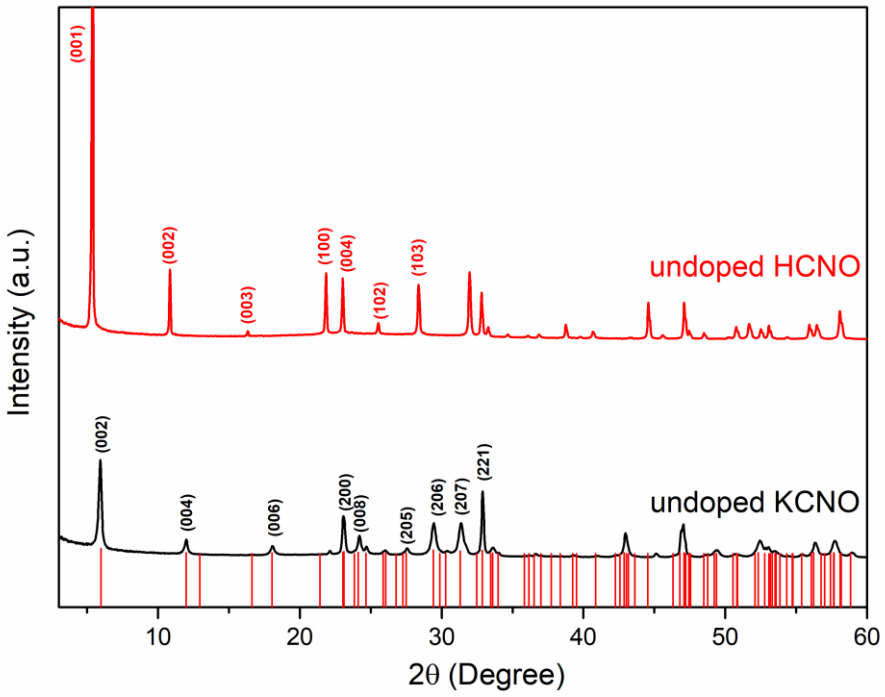

Figure 2.5: XRD Pattern of $KCa_2Nb_3O_{10}$ and its protonated version $HCa_2Nb_3O_{10}$.

In brief, to obtain $[Ca_2Nb_3O_{10}]^-$ nanosheets, starting from the synthesis of $KCa_2Nb_3O_{10}$, the steps of obtaining protonated powder by acid treatment and exfoliation are followed. Figure 2.6 a-c shows scanning electron microscopy (SEM) images of each step of the powders. SEM images confirm the layered nature of $KCa_2Nb_3O_{10}$ and protonated $HCa_2Nb_3O_{10}$ are well-crystallized with large lateral grain size. The layered structure can be seen more clearly in the protonated species that results from the displacement of potassium with proton or hydronium ions. Figure 2.6 c shows SEM images of restacked $[Ca_2Nb_3O_{10}]^-$ nanosheets after the exfoliation process. It was observed that the surface area increased significantly. The addition of protons into the exfoliation solution of nanosheets restacks the nanosheets as a result of electrostatic attraction between the cation and the negatively charged nanosheets. The random packing was clearly observed in the SEM image.

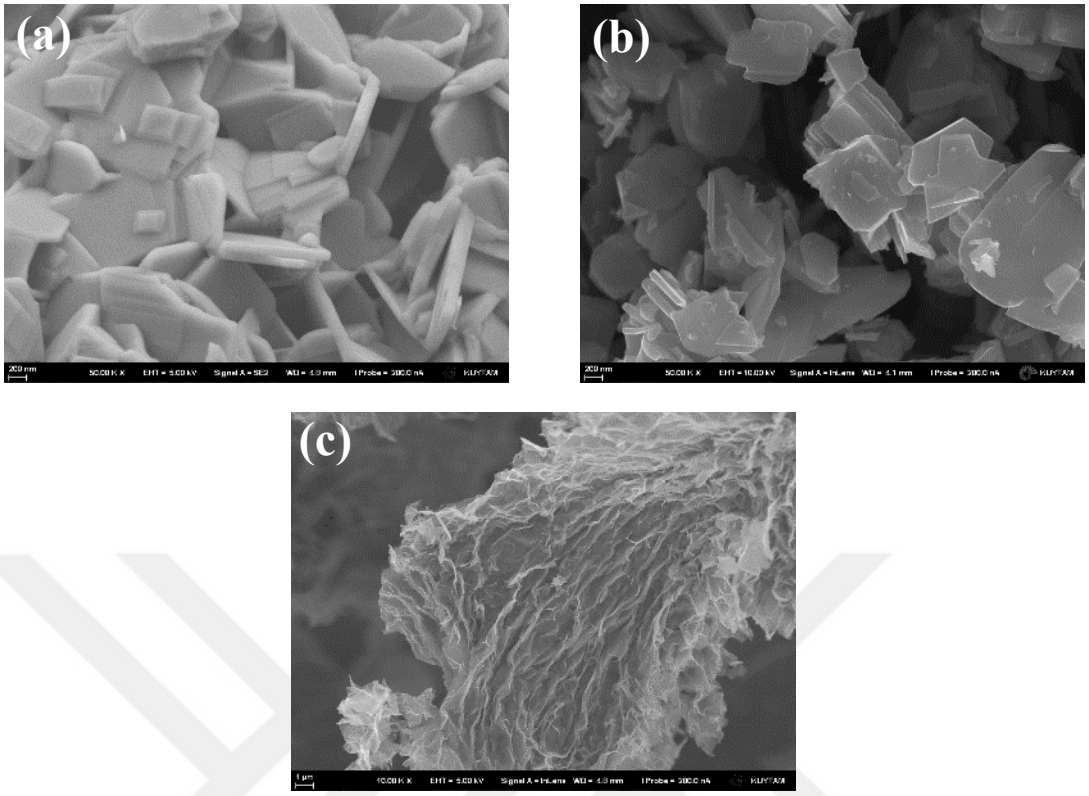

Figure 2.6: SEM Images of $KCa_2Nb_3O_{10}$ (a), $HCa_2Nb_3O_{10}$ (b) and $[Ca_2Nb_3O_{10}]^-$ nanosheet (c) powders

After the structural characterization, the optical characterization was performed to determine the band structure and band positions of the layered perovskite. To evaluate the optical energy band gap of the materials, Kubelka-Munk absorption data is transformed into a Tauc plot as follow:

$$(ahv)^{1/n} = A(hv - E_g) \quad (2.1)$$

The absorption coefficients, Planck constant, light frequency, proportionality constant, and band gap energy are represented by α, h, ν, A, and Eg, respectively. The exponent 'n' signifies the semiconductor's transition properties, where n = 1/2 and n = 2 correspond to direct and indirect transitions, respectively. Extrapolation of the linear portion of the curve to the x-axis determines the band gap energy [117].

The Tauc plots derived from the reflectance data obtained with an integrated sphere attached to the UV−vis absorption spectroscopy show that, the bandgap of KCNO and HCNO are 3.57eV and 3.49 eV respectively, as shown in Figure 2.7 a, b. In addition, valence band level estimated 2.75 V (vs NHE) for KCNO and 1.8 V (vs NHE) for HCNO from XPS Valence band spectra analysis (Figure 2.7 c, d). The conduction band was estimated by subtracting the band gap value from the valence band value obtained from

the XPS data. With this calculation, the conduction bands of KCNO and HCNO were found to be -0.82 V and -1.69 V, respectively.

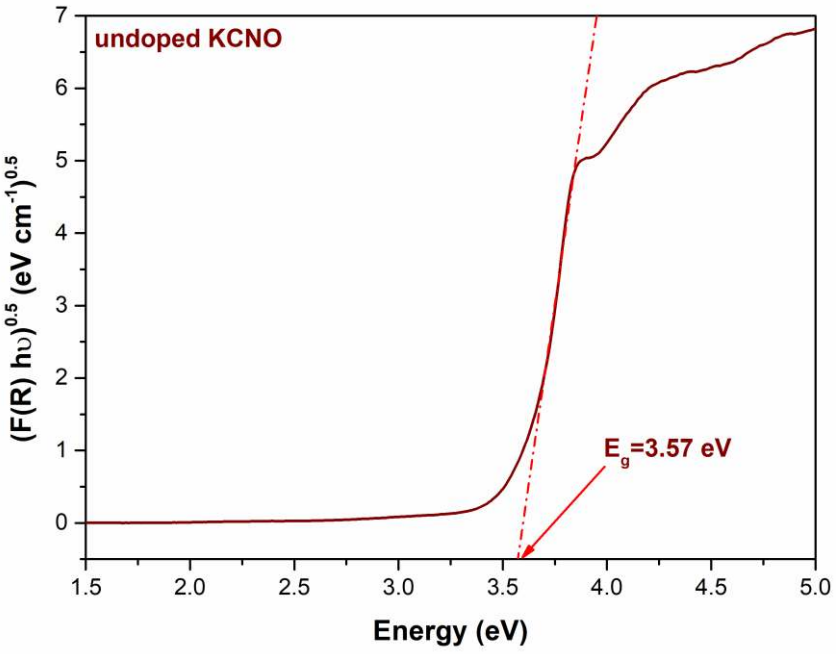

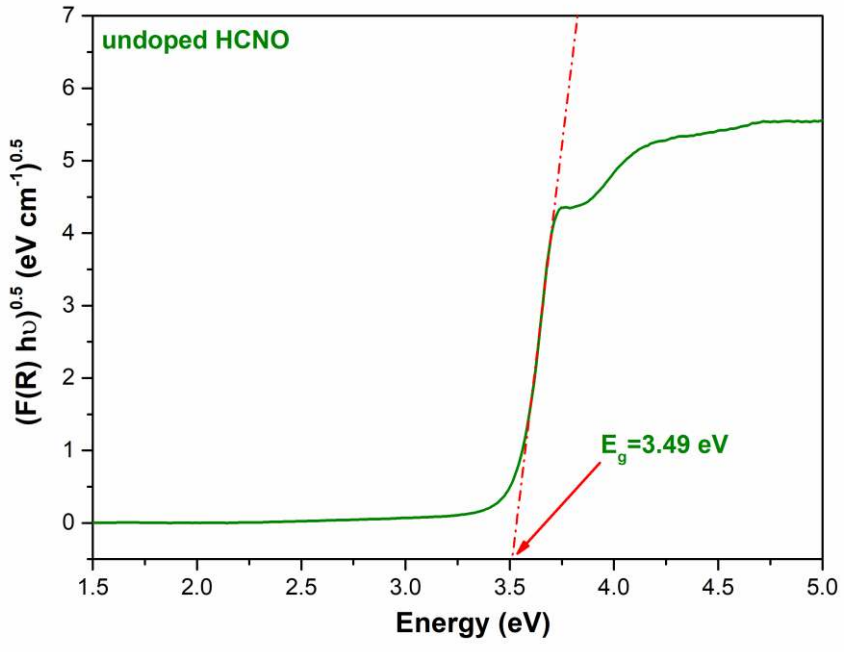

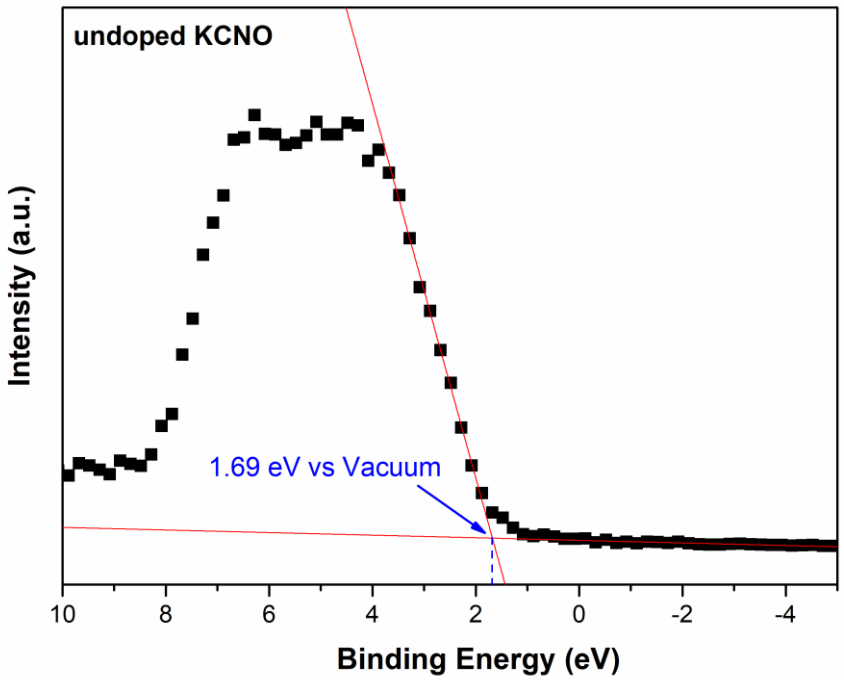
undoped KCNO
Intensity (a.u.)
1.69 eV vs Vacuum
10
8
6
4
2
0
-2
-4
Binding Energy (eV)

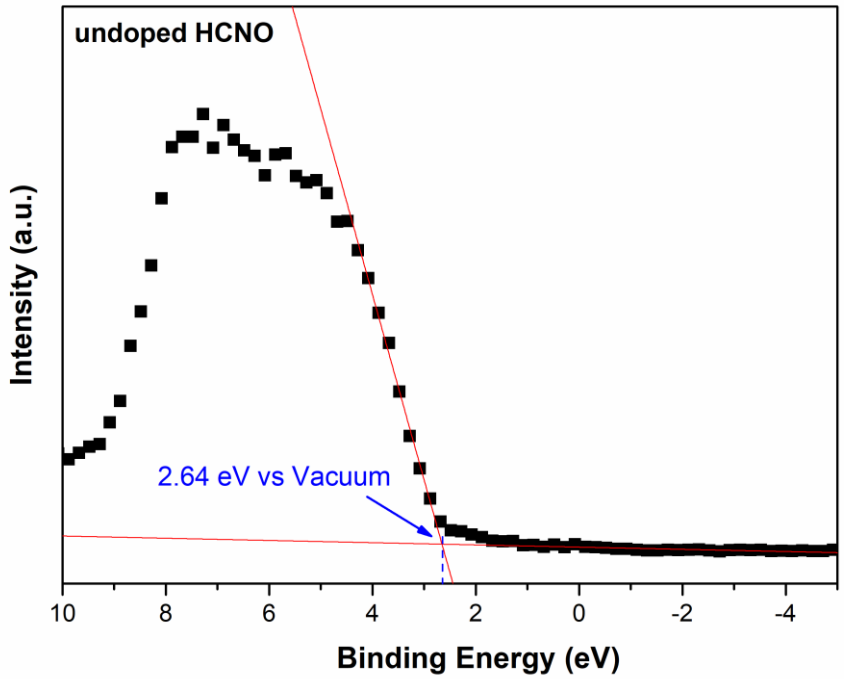
undoped HCNO
Intensity (a.u.)
2.64 eV vs Vacuum
10
8
6
4
2
0
-2
-4
Binding Energy (eV)

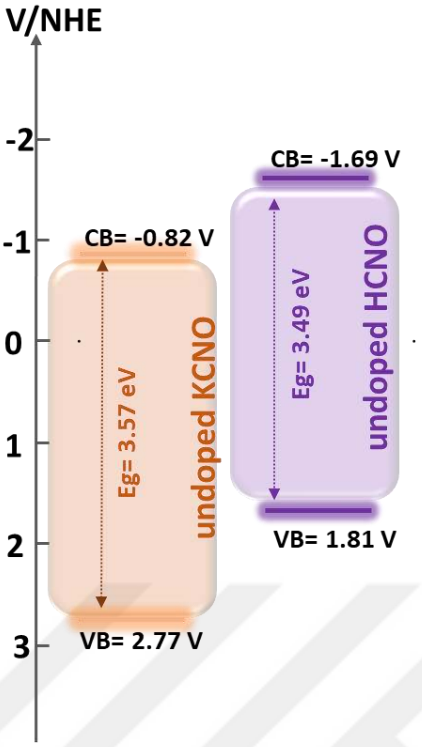

Figure 2.7: Tauc's plots of $KCa_2Nb_3O_{10}$ (KCNO) phase (a) and its protonated version $HCa_2Nb_3O_{10}$ (HCNO) phase (b) for the estimation of the band gap, XPS Valence band spectra of KCNO (c) and HCNO (d) and band structure of KCNO and HCNO for determination of the valence band level.

2.4.2 Electrochemical Characterization of Hole Scavengers

The behavior and effect of hole scavengers on photocatalytic activity were investigated in the means of electrochemical and photoelectrochemical tests. The six different hole scavengers were chosen from the literature and 0.5 M K_2SO_4 solution was used as a reference solution to investigate impact of hole scavengers on photocatalytic activity. Initially, 3 of them, which exhibited superior performance, were identified for a detailed analysis of photocatalytic behavior, utilizing cyclic voltammetry and photocurrent experiments.

In our investigation, cyclic voltammetry tests were initially conducted to determine the photoelectrochemical behavior of hole scavengers. As discussed before, during the photocatalytic water splitting reaction, the transition of valence band electrons to the conduction band is induced by the incident light on a photocatalyst (Figure 2.2). While some of these electrons participate in water reduction reactions, those lacking the

necessary energy results in e^--h^+ recombination. This phenomenon hinders the photocatalytic activity. A highly effective strategy for mitigating recombination is the utilization of hole scavengers. Introduced hole scavengers have higher oxidation potentials and thus readily accept these holes. They prevent recombination by capturing the holes, allowing the electrons to participate in the reduction half-reaction, while the scavengers themselves undergo oxidation.

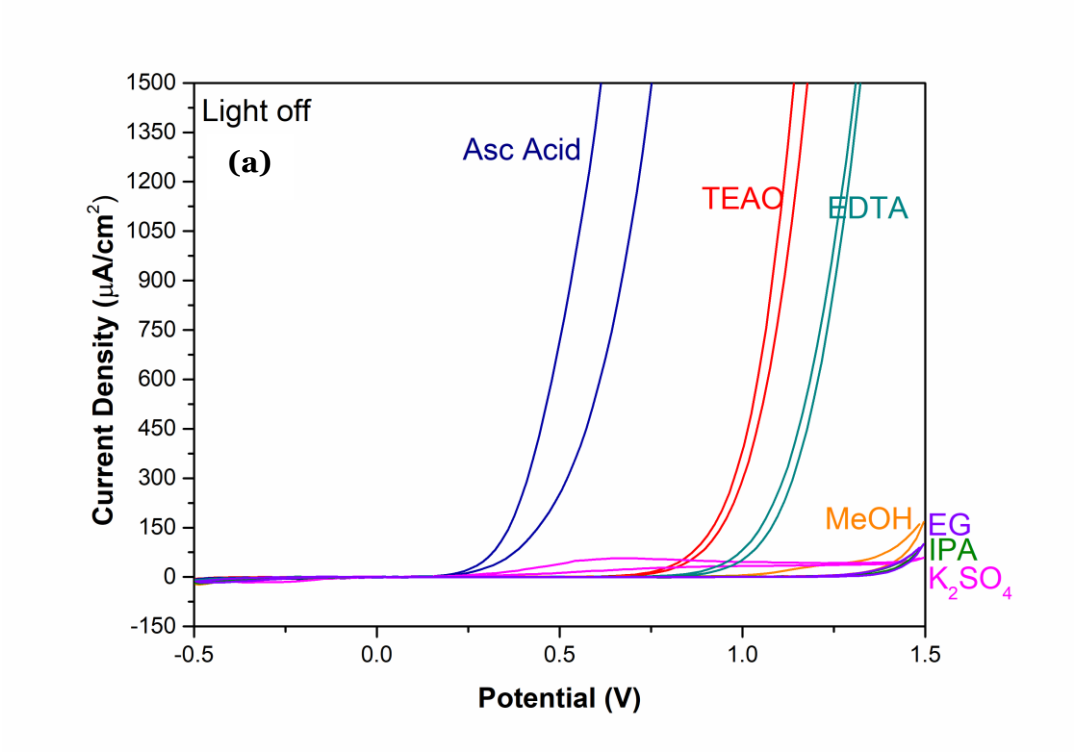

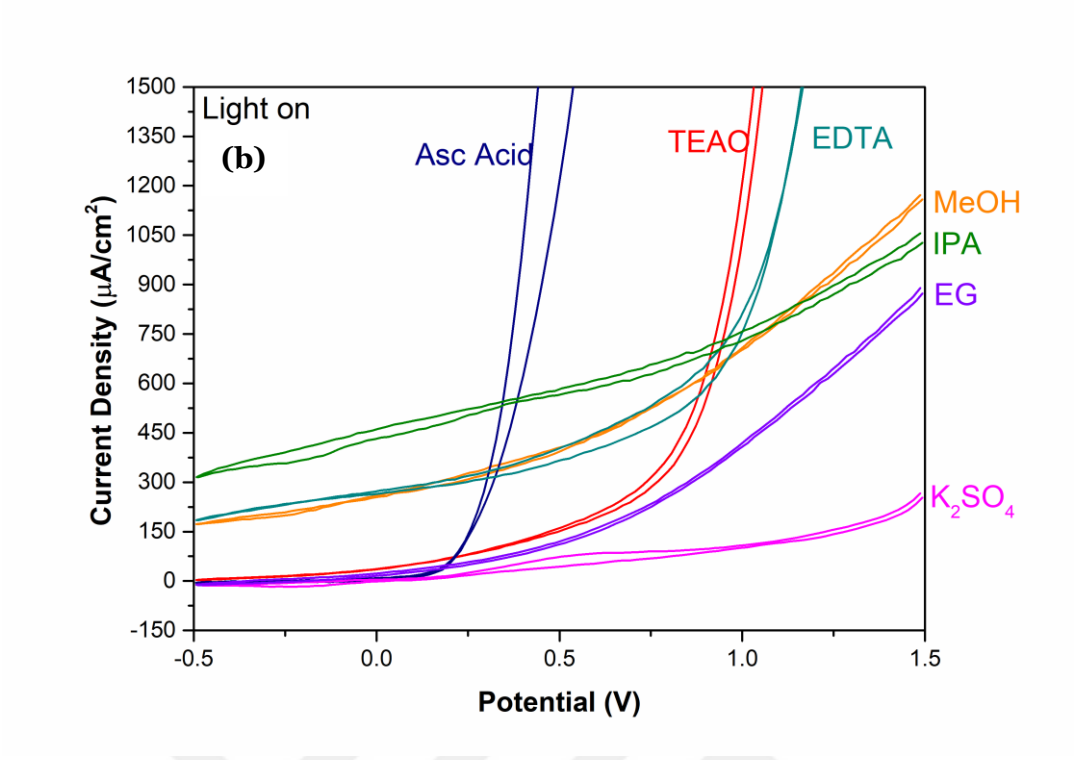

Figure 2.8: CV tests between -0.5 V-1.5V vs SCE dark (a) and under illumination (b) conditions

Cyclic voltammetry test for ascorbic acid, EDTA-Na_2, triethanolamine, MeOH, IPA, EG and K_2SO_4 at concentration of 0.1 M, 0.1 M, 0.5 M, 0.5 M, 0.5 M and 0.5 M respectively. The working electrode is an FTO electrode coated with a single layer of $[Ca_2Nb_3O_{10}]^-$ nanosheet. The Figure 2.8 a shows the CV curves in the dark and Figure 2.8 b shows the CV curves under illumination. All solutions were saturated with Ar or N_2 before starting the CV tests.

CV was performed in the range of -0.5 V-1.5 V vs SCE to investigate the oxidation potentials of hole scavengers 2D nanosheets of $[Ca_2Nb_3O_{10}]^-$. A 0.5 M K_2SO_4 solution used as a reference electrolyte, without hole scavenger. Other electrolytes were prepared with 0.5 M K_2SO_4 as a supporting solution and each incorporating a specific hole scavenger: 0.5 M methanol, 0.5 M isopropyl alcohol, 0.5 M vol triethanolamine, 0.5 M ethylene glycol, 0.1 M EDTA-Na_2, and 0.1 M ascorbic acid. To maintain the same pH in all the electrolytes, the EDTA-Na_2 and ascorbic acid solutions were prepared at 0.1 M and the other solutions at 0.5 M. Prior to each experiment, the electrolytes were purged with Argon for a duration of 15 minutes. Here, it is worth mentioning that the pH value for

each solution, particularly for ascorbic acid, triethanolamine and EDTA-Na_2, are different from each other. Ascorbic acid and EDTA-Na_2 results in slightly acidic solution, whereas triethanolamine solution is slightly basic. Alcohol solutions and K_2SO_4 solution possess neutral pH. The illumination produced anodic photocurrents on the surface of nanosheets as a result of photoinduced oxidation of molecules. Methanol, isopropyl alcohol and EDTA-Na_2 produced photocurrent even at negative potentials at which other molecules did not show any activity. Thus, it was decided to use methanol, isopropyl alcohol and EDTA-Na_2 for photocatalytic experiments because they both have appropriate oxidation potentials and give current response even at 0.0 V.

2.4.3 Photoelectrochemical Characterization of Hole Scavengers

After CV measurement, chronoamperometric photocurrent responses were examined 0.0 V vs SCE for these molecules. Chronoamperometry experiments were conducted by applying a constant potential of 0 V vs SCE on the working electrode, with chopping light (10 second off-10 second on) throughout the experiment. The current responses were recorded over a 300 second period. The chronoamperometry (current density-time) graphs are presented in Figure 2.9. The current density amplitudes for all the samples can be seen from the Table 1. Methanol, isopropyl alcohol and EDTA-Na_2 produced the highest photocurrents in accordance with the CV tests. In addition, the current−time (I−t) curves of the methanol, isopropyl alcohol and EDTA-Na_2 show outstanding stability. Photocurrents increase to 200 μA/cm^2, 250 μA/cm^2, and 480 μA/cm^2 as the UV light is turned on and off for methanol, EDTA-Na_2, and isopropyl alcohol, respectively.

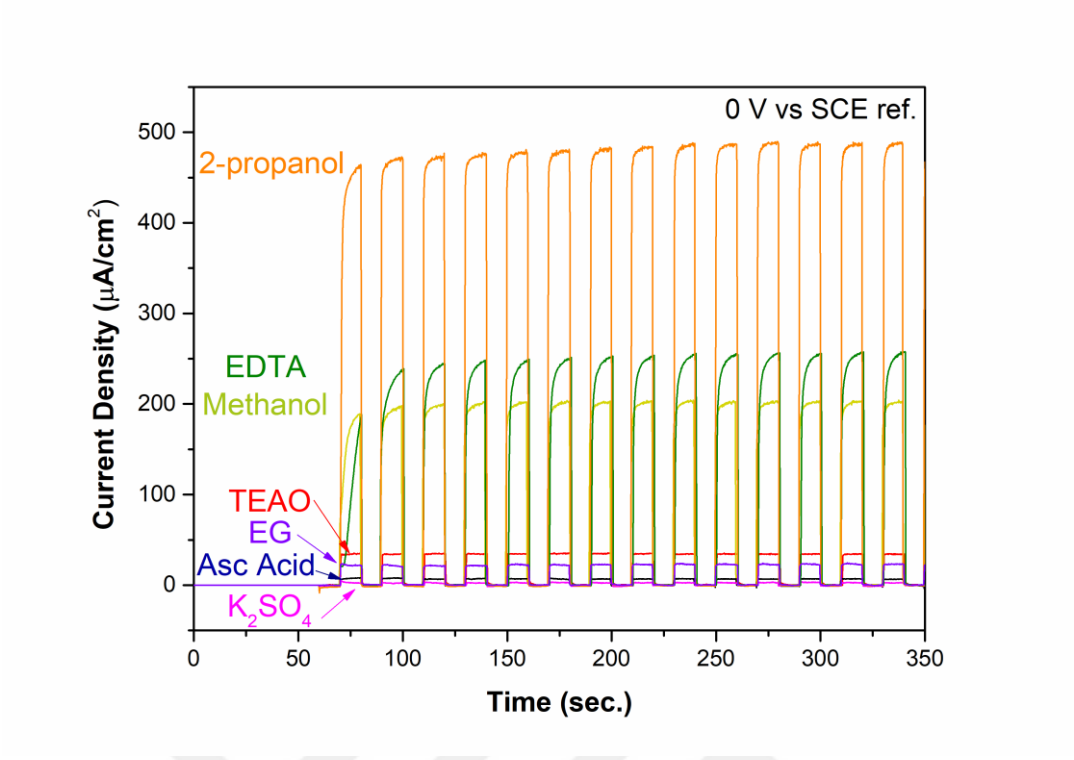

Figure 2.9: Chronoamperometry analysis: I-t graphs of hole scavengers

Table 1 The current density amplitudes for all the samples

		Current Density (µA/cm2)
Isopropyl alcohol	0.5 M	480
Methanol	0.5 M	200
Triethanolamine	0.5 M	33.2
Ethyleneglycol	0.5 M	25
EDTA-Na_2	0.1 M	250
Ascorbic Acid	0.1 M	8.6
K_2SO_4	0.5 M	2.5

This result confirms the ability of the added hole scavengers to capture holes photogenerated on $[Ca_2Nb_3O_{10}]^-$. In this way, by preventing the recombination of holes with electrons, electrons have been proven to contribute to the photocurrent. The highest current density was obtained by the $[Ca_2Nb_3O_{10}]^-$ film with the 2-propanol hole scavenger. The lowest current density is obtained from the 0.5 K_2SO_4 solution in the absence of a hole scavenger, in accordance with expectations. Among all the hole scavengers, the

lowest current density is achieved with Ascorbic Acid. Upon evaluation of CV and photocurrent data, the highest current density results were obtained with the isopropyl alcohol (IPA), methanol and EDTA-Na_2.

The CV curves for the chosen hole scavengers on the nanosheets under illumination and dark are given in Figure 2.10. Fresh solutions of 2.5% vol IPA, 2.5% vol MeOH, 0.1 M EDTA-Na_2 in 0.5 M K_2SO_4 solution and 0.5 M K_2SO_4 solution as reference were prepared for CV tests. The electrochemical response was examined under dark conditions, and the photoelectrochemical response was examined under illumination with Xe lamp.

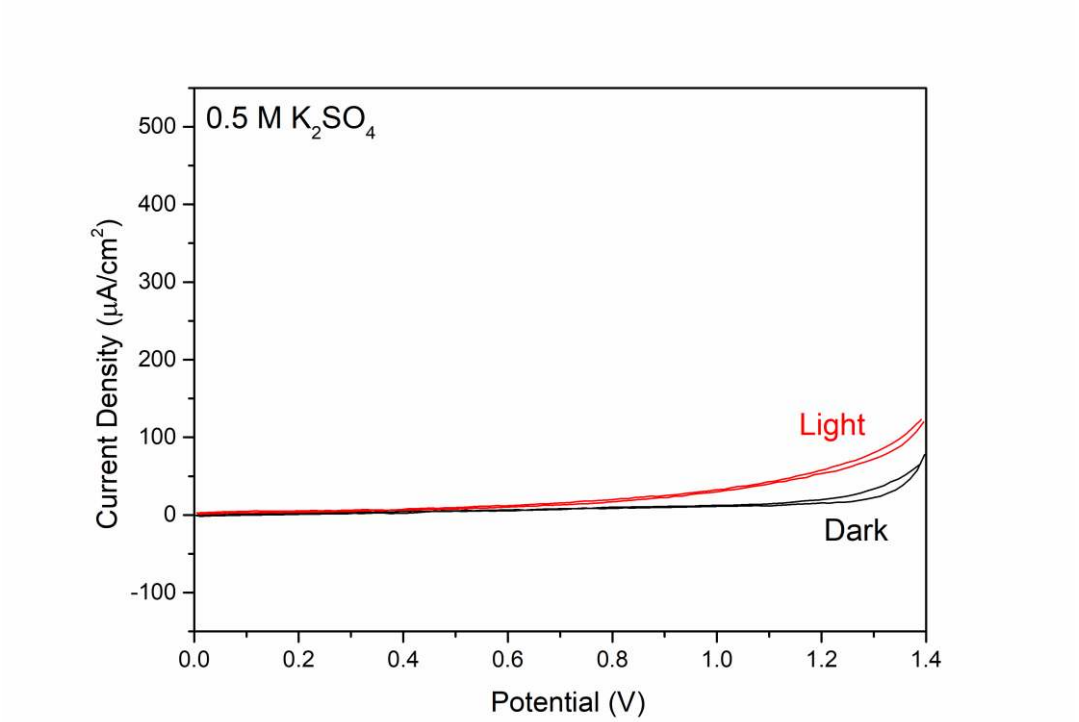

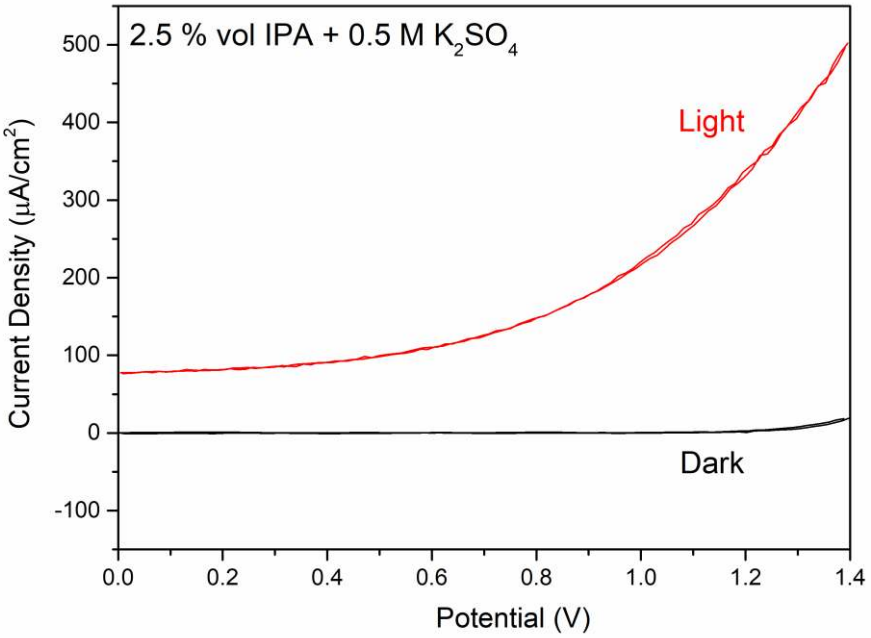
2.5 % vol IPA + 0.5 M K_2SO_4
Light
Dark
Current Density (μA/cm²)
Potential (V)
500
400
300
200
100
0
-100
0.0
0.2
0.4
0.6
0.8
1.0
1.2
1.4

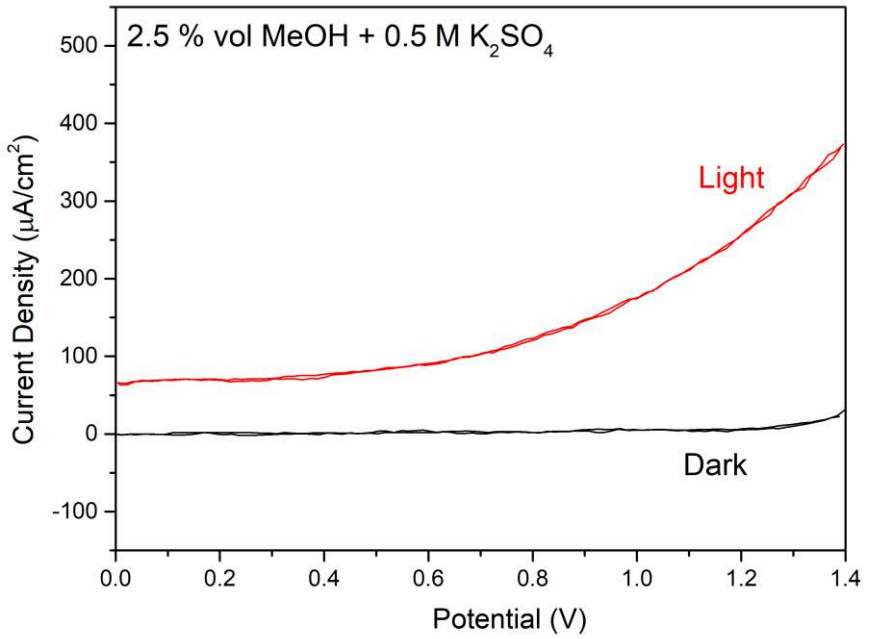
2.5 % vol MeOH + 0.5 M K_2SO_4
Light
Dark
Current Density (μA/cm²)
Potential (V)
500
400
300
200
100
0
-100
0.0
0.2
0.4
0.6
0.8
1.0
1.2
1.4

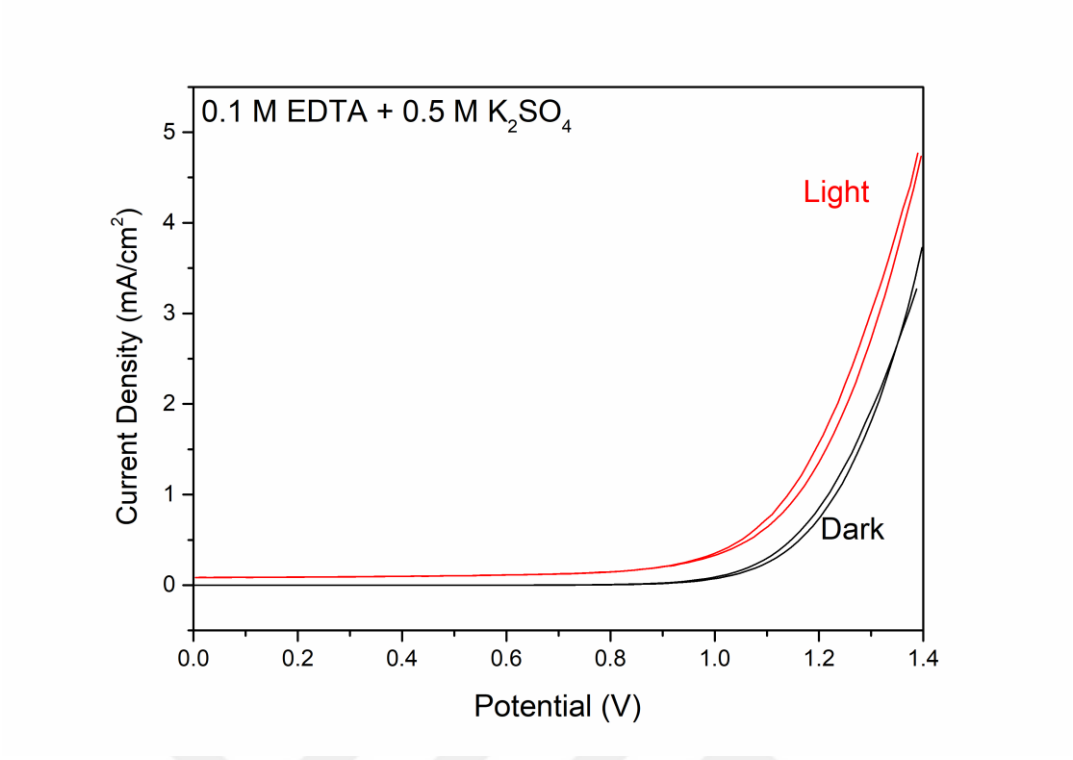

Figure 2.10: Cyclic voltammetry analysis of 0.1 M EDTA-Na_2, 2.5% vol IPA, 2.5% vol MeOH in 0.5 M K_2SO_4 and 0.5 M K_2SO_4 at between 0-1.4 V vs SCE.

As demonstrated by the graph in the Figure 2.10 there was an increase in photocurrent with increasing potential. This is due to the occurrence of band bending with increasing potential, leading to a decrease in electron-hole recombination at higher potentials [118]. The photocurrents of K_2SO_4, MeOH, IPA and EDTA-Na_2 at 1.4 V vs SCE are 110 µA/cm^2, 376 µA/cm^2, 504 µA/cm^2 and 4.6 mA/cm^2, respectively.
Thermodynamically, a determining factor for the positive impact of various hole scavengers on the rate of photocatalytic H2 evolution is their oxidation potential in comparison to that of water[119], [120]. To analyze the surface reaction kinetics of $[CNO]^-$ nanosheets, current densities were examined at around 0.575 vs SCE (equivalent to 1.23 VS NHE) for MeOH, IPA, and K_2SO_4, and approximately 0.756V vs SCE for EDTA-Na_2, as illustrated in the Figure 2.11. the applied potentials (E_{SCE}) were converted to the normal hydrogen electrode (NHE) with the Nernst equation:

$$E_{NHE}=E_{SCE}+0.059 \times pH+ E^0_{SCE} \quad (2.2)$$

where E_{NHE} is potential estimated vs. NHE, E_{SCE} is measured potential vs. SCE electrode,

and $E°_{SCE}$ = 0.244 V is the standard electrochemical potential of the SCE electrode.

The rationale for testing EDTA-Na_2 and others at different potentials is due to variations in the pH levels of the electrolytes; the pH is roughly 4 for EDTA-Na_2 and 7 for MeOH, IPA, and K_2SO_4. This phenomenon arises from the electron transfer process occurring between the photocatalyst and H_2O molecules. Consequently, a higher current density signifies the enhanced transfer of electrons from the photocatalyst to H_2O, leading to increased catalytic activity. In this context, the use of EDTA-Na_2 as a hole scavenger allows for the capture of a greater number of holes, facilitating the involvement of a larger number of electrons in the reactions.

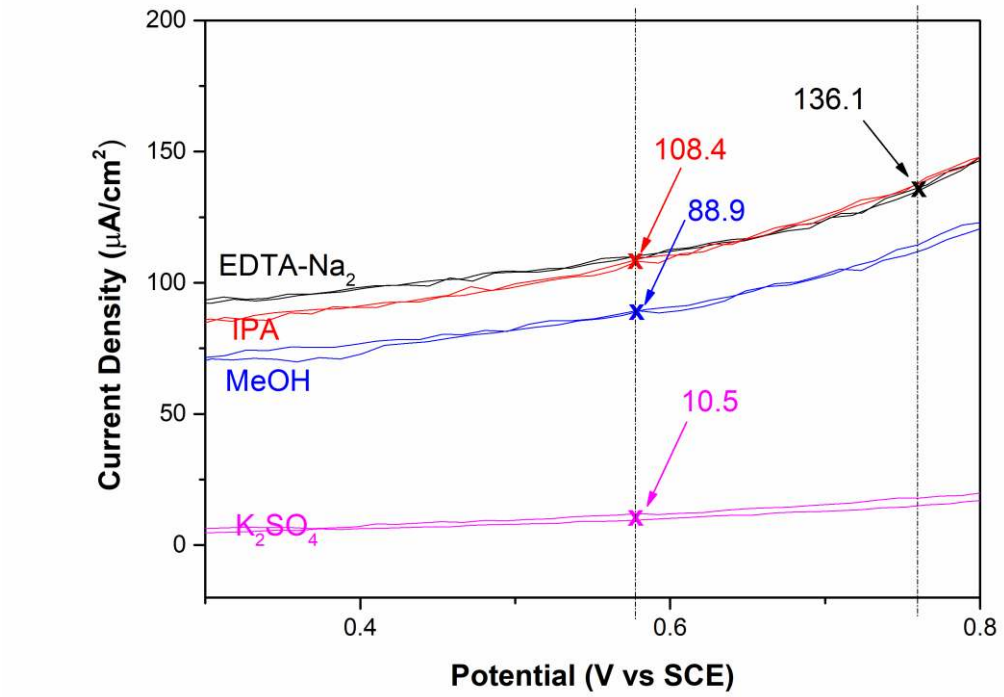

Figure 2.11 The current densities at ~0.575 vs SCE (equivalent to 1.23 vs NHE) for MeOH, IPA, and K_2SO_4, and at ~ 0.756V vs SCE for EDTA-Na_2 (equivalent to 1.23 vs NHE)

Current doubling effect may be present for EDTA-Na_2, for which we obtained the highest current density from CV results. Briefly, the current doubling effect is the formation of unstable radicals during the reaction in the presence of an organic molecule in a photoelectrochemical cell, and then the additional free electrons from the reaction move to the conduction band of the photocatalyst and contribute to the current [121]–[124]. Additionally, Hykaway et al. [125] reported that the doubling of current depends

on the pH value of the electrolyte. Specifically, they found that the current doubling rate increases with increasing acidity (decreasing pH) of the electrolyte due to removal of the hydroxyl layer on the photocatalyst surface using acidic solvents. Since the solution prepared with EDTA-Na_2 (pH = 4) has a lower pH value than the solutions prepared with other hole scavengers (pH = 7), it is possible that one reason for its higher current output is due to the current doubling effect.

The oxidation potential of the molecule determines the efficiency of hole scavenging, which entails the elimination of photogenerated holes. A more negative oxidation potential results in a stronger driving force for hole scavenging, thereby leading to a faster process[115]. Thus, hole scavengers with a redox potential more negative than water effectively capture photogenerated holes at a faster rate. This rapid capture reduces electron recombination losses, leading to increased H_2 formation rates. The plots show that the oxidation potentials of the scavengers are estimated 0.845V, 0.618V, 0.510V and 0.461V versus SCE for K_2SO_4, MeOH, IPA and EDTA-Na_2 respectively. These values have been adjusted to a pH=7 compared to the standard hydrogen electrode to facilitate clearer and simpler comparisons. Accordingly, the oxidation potentials of hole scavengers were calculated as 1.174 V for methanol, 1.264 for IPA and 1.322 V for EDTA-Na_2. The Figure displays the process of scavenging holes and the oxidation potentials.

To summarize, the semiconductor photocatalyst is activated by light, causing electrons in the valence band to transfer to the conduction band. Photogenerated electrons leave behind gaps in the valence band, thereby creating e^- -h^+ pairs. This process facilitates the formation of H_2 through electron reduction reactions that occur via the conduction band in photocatalytic water splitting. Photogenerated holes are involved in oxidation reactions. Furthermore, recombination, which refers to the return of electrons to the holes, may take place. As a result, photocatalytic activity is decreased.

The holes within the valence band lead to the oxidation of water and generate hydroxyl radicals, which then combine with the electrons within the conduction band to create hydroxide ions. In other words, the electrons intended for reduction reaction and hydrogen formation contribute to an undesirable reaction instead.

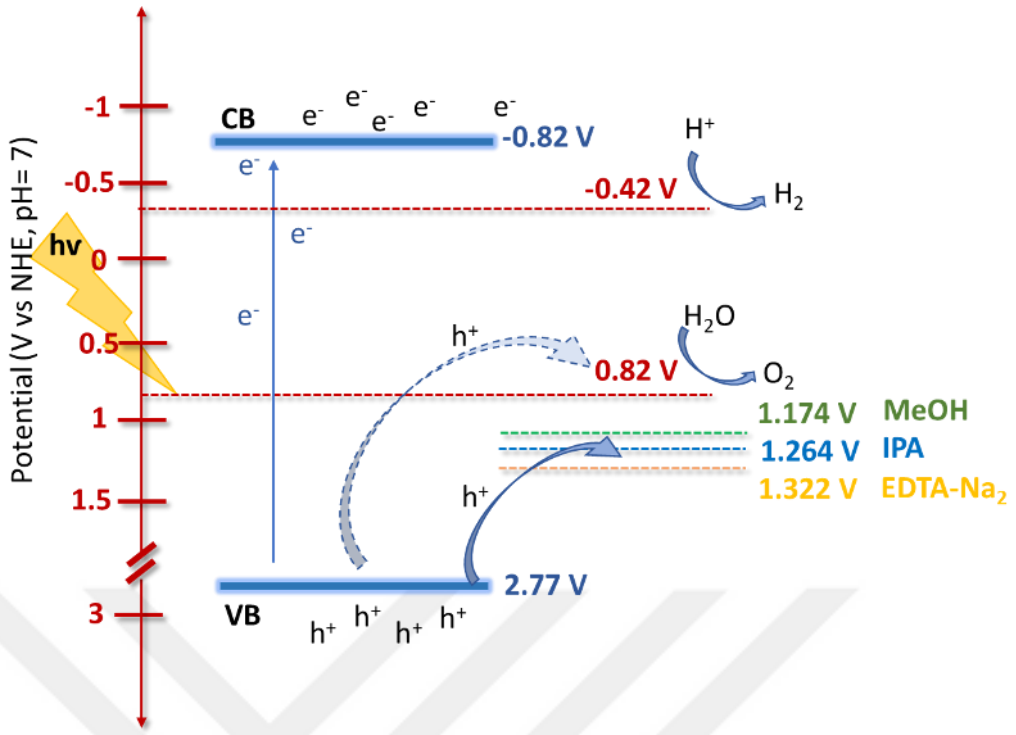

Figure 2.12: Oxidation potentials of MeOH, IPA and EDTA-Na_2 at ph=7 (V vs NHE)

Hole scavengers adsorbed on the surface of the photocatalyst capture the holes before they oxidize water. The oxidation potential of hole scavengers is more positive than water, which leads them to capture holes prior to the water. For instance, if methanol is used as a hole scavenger, the hole oxidizes the methanol and the methanol converting into methyl hydroxyl radical. Moreover, the hole scavenger may follow another pathway whereby methanol captures the hydroxyl radical from water that has already undergone oxidation, preventing it from attending the reaction with the electron [126]. This mechanism is represented in the Figure 2.13.

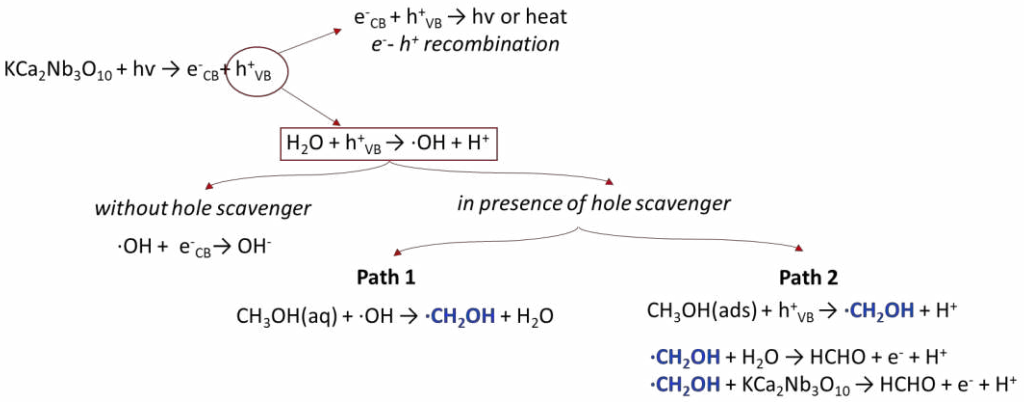

Figure 2.13: Photocatalytic mechanism of behaviors of holes in hole scavenger-free system and in presence of methanol as a hole scavenger by using $KCa_2Nb_3O_{10}$

photocatalyst.

Photoresponse comparison at 0 V is given in the Figure 2.14. As can be seen, while for 0.5 M K_2SO_4 (no-hole scavenger) this value was about 1.72 µA/cm^2, it showed a positive shift with the addition of hole scavenger as MeOH (64.9 µA/cm^2), IPA (76.9 µA/cm^2) and EDTA-Na_2 (84.37 µA/cm^2) respectively at 0 V. Although no potential is applied here, hole scavengers are still expected to give a current response, especially for EDTA-Na_2, which gave the highest value, the resistance to cross the oxidation barrier is expected to be less.

After detailed electrochemical and photoelectrochemical analysis of hole scavengers on $[Ca_2Nb_3O_{10}]^-$ nanosheets, we have performed photocatalytic hydrogen evolution tests on the nanosheets in the presence of different hole scavengers to validate their behavior.

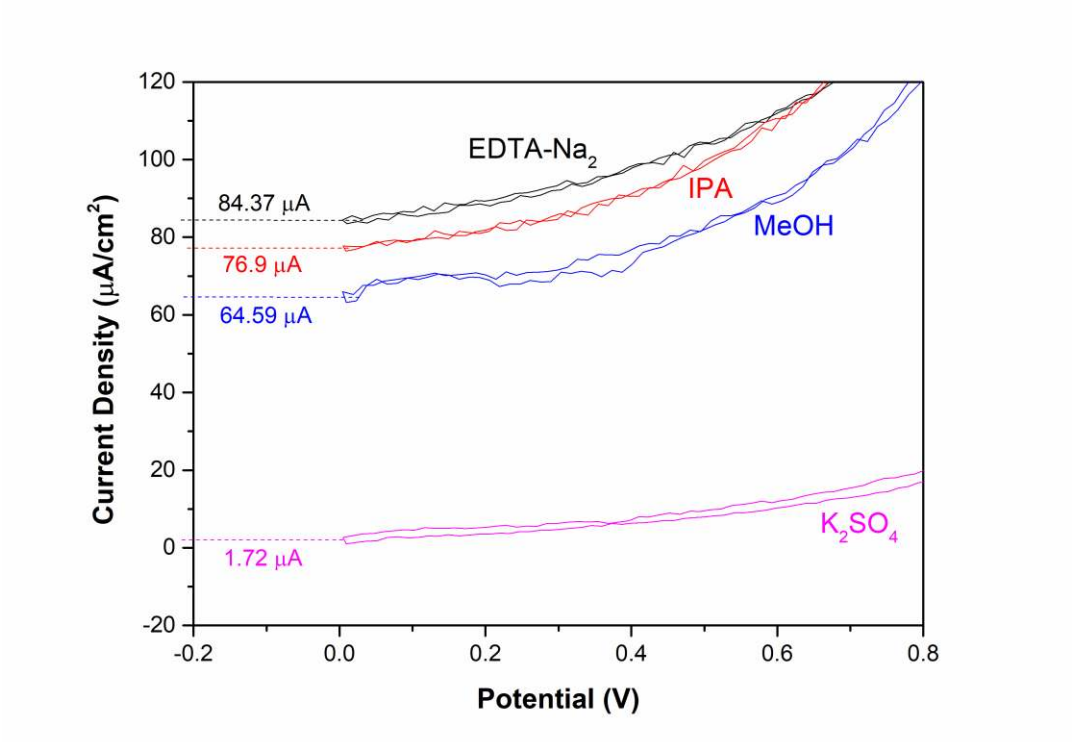

Figure 2.14: The current density values of K_2SO_4, MeOH, IPA and EDTA-Na_2 at 0 V.

Figure 2.15 illustrates the comparison of the H_2 amounts generated by $[Ca_2Nb_3O_{10}]^-$ nanosheets without hole scavengers and in the presence of hole scavengers in the electrolyte. $[Ca_2Nb_3O_{10}]^-$ nanosheets produced 4.3 µmol/g H_2 under UV irradiation in a hole scavenger free 0.5 M K_2SO_4 electrolyte. Notably, a significantly higher amount of H_2 was generated in the presence of 0.1 M EDTA-Na_2 (63.68 µmol/g), followed by 2.5

vol% IPA (25.89 µmol/g) and MeOH (16.8 µmol/g). It can be suggested that the greater the oxidative potential of the hole scavenger, the more efficient the production of hydrogen. The photocatalytic trend is in accordance with the observed photoelectrochemical behavior. Higher photocatalytic H_2 evolution from the EDTA-Na_2 solution may be attributed to the lower pH of the EDTA-Na_2 solution. At lower pH values,

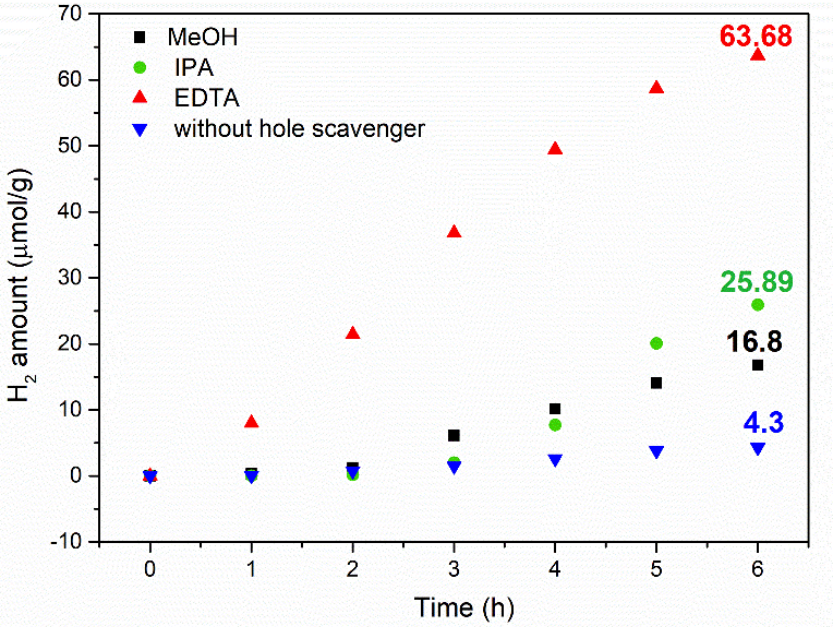

Figure 2.15: Photocatalytic hydrogen evolution rates on $[CNO]^-$ nanosheets for without hole scavenger and in the presence of methanol, IPA and EDTA-Na_2 as a hole scavenger under illumination with an unfiltered 300 W Xe lamp.

H^+ concentration is higher, which is beneficial for the photocatalytic H_2 evolution reaction.

2.5 Conclusion

The aim of this study was to understand mechanistically the effect on photocatalytic efficiency of hole scavengers, which are used to prevent electron-hole recombination, one of the major problems that severely reduce photocatalytic activity. The photocatalyst selected for this experiment is $[Ca_2Nb_3O_{10}]^-$ nanosheet. Six different hole scavengers, selected from the literature, were compared alongside a reference solution of 0.5 M K_2SO_4 to evaluate their effect on photocatalytic activity. Three hole scavengers, exhibiting superior performance, underwent comprehensive analysis of their photocatalytic behavior through cyclic voltammetry and photocurrent experiments. The

photocurrents, IPA, MeOH, EDTA-Na_2 and K_2SO4 as a reference were 480 µA/cm2, 250 µA/cm2, 200 µA/cm^2 and 2.5 mA/cm^2, respectively. It can be seen from here that the photocurrent of using hole scavenger increases significantly. The introduced scavengers possessed higher oxidation potentials, which readily accepted the holes and prevented recombination by capturing them. For this purpose, the CV was set in the range of 0-1.4 V vs. SCE and the oxidation potentials of hole scavengers were calculated as 1.174 V for methanol, 1.264 for IPA and 1.322 V for EDTA-Na_2. Photocatalytic H_2 evolution experiments were performed to examine photocatalytic behavior and kinetics. EDTA-Na_2, as expected, also gave the highest amount of 63.68 µmol/g, followed by 2.5 vol% IPA (25.89 µmol/g) and MeOH (16.8 µmol/g). This can be attributed to the fact that the oxidation potential is more positive than others and the current doubling effect increases in more acidic solutions. The findings underscore the importance of strategic scavenger choice in advancing the performance of photocatalytic systems. The success of EDTA-Na_2 prompts further research into tailored scavenger agents to drive efficient hydrogen evolution.

CHAPTER 3: EFFECT OF PALLADIUM DOPING ON PHOTOCATALYTIC HYDROGEN EVOLUTION (HER) REACTIONS

3.1. Introduction

Clean and renewable hydrogen is found to be an alternative fuel by replacing the existing fossil fuels over the deep carbonization of global energy systems. Hydrogen energy is promising for renewable energy to meet the challenges of an energy crisis. The photocatalytic production of hydrogen is a promising approach for splitting water using solar energy and offering a sustainable solution.

Semiconductor materials are commonly selected as photocatalysts in photocatalytic water splitting reactions because of their distinctive characteristics. They are favored for their unique electronic band structures and tunable bandgap properties, efficiently separating, and transporting, high surface areas, their durability and compatibility.

Numerous semiconductor materials, including metal oxides (TiO2, CoO, ZnO, WO^3 etc), metal sulfides (MoS_2, CdS, ZnS, WS etc), g_3N_4 and nanocomposites have been developed for the photocatalytic water splitting process over the past few decades.

Among the various semiconductor materials, 2D layered materials have garnered special attention and importance. The 2D materials offer tunable band gaps by adjusting their thickness, allowing for a customizable light absorption range. The reduced thickness of these materials has the advantage of shortening the migration distance of charge carriers, thereby mitigating the recombination of photo-generated carriers. Additionally, the high surface atom proportion in 2D materials provides an abundance of surface active sites, promoting the activation of reaction substrates [127].

2D layered materials, such as transition metal dichalcogenides (TMDs), graphitic carbon nitride (g-C_3N_4), hexagonal boron nitride (h-BN), black phosphorus (BP), metal–organic layers (MOLs), covalent organic frameworks (COFs) and 2D layered perovskite oxides have emerged as good candidates within the semiconductor family. Their atomic-thin nature and large surface areas provide abundant active sites for catalytic reactions, resulting in enhanced photocatalytic activity. Additionally, these materials often exhibit tunable bandgaps, enabling them to absorb a broader range of light. This feature is crucial

as it maximizes light absorption and utilization, making them efficient photocatalysts. Furthermore, 2D layered materials offer efficient charge separation and transport due to their unique crystal structures. Electrons and holes are confined to distinct layers, minimizing the chance of recombination, and extending the lifetime of charge carriers.

2D layered perovskite oxides, have been studied intensively to date. Dion–Jacobson (DJ) phase has often been used as photocatalysts among the layered perovskite oxides. These materials consist of negatively charged perovskite layers and interlayer cations that compensate the negative charge, and the general compositions for the DJ as $A'[A_{n-1}B_nO_{3n+1}]$. These materials are reported to exhibit unique photocatalytic properties derived from the layered structures, which involve ion-exchange and their doped structures. Additionally, the exfoliation of layered materials into monolayer 2D nanosheets enhances the specific surface area and generates more active catalytic sites. Additionally, the ultrathin layer structure of 2D materials facilitates charge and mass transfer [127].

However, the overall conversion efficiency is still insufficient for practical applications. To increase water splitting efficiencies, strategies such as control of size and morphology, metal oxide heterostructure, surface modification, integration of additives like metal doping, addition of plasmonic metal nanoparticles (NPs), co-catalyst, exfoliation method and formation of heterojunctions are used.

Among these various methods, metal doping stands out as a notable and widely use strategy. Single-site atom doping offers certain benefits in comparison to conventional doping methods. Single-atom catalysts represent an innovative approach to catalysis, allowing for enhanced utilization of scarce atoms and improving catalytic activity and stability [128]. Single-site doping allows for the precise inclusion of dopant atoms at specific lattice sites within the crystal structure of the photocatalyst. This leads in a more uniform distribution of dopants throughout the material. Single-site dopants can act as active sites for the photocatalytic reactions and enhancing the photocatalytic activity. Surface doping may result in the saturation of dopants at the catalyst's surface or agglomeration of the surface, limiting further improvement in catalytic activity. In contrast, single-site doping eliminates this problem by achieving a more even dispersion of dopant atoms within the crystal structure. In this study, Pd noble metal was chosen for single site atom doping. The incorporation of Pd as a single-site atom dopant can alter the electrical band structure of photocatalyst. Depending on the doping concentration, this might cause the narrowing or shifting of the bandgap to visible spectrum. Also, it can

serve as a catalytic site for redox reactions, facilitating the transfer of charge carriers. Pd doping can reduce the recombination rate of electron-hole pairs by providing additional recombination pathways, leading to more efficient charge utilization.

Single-site doped Pd doped bulk $KCa_2Nb_3O_{10}$ phase was synthesised at doping rates of 1.5% and 3%. Subsequently, nanosheet powders were obtainged via proton exchange, followed by exfoliation. The photocatalytic and photoelectrochemical properties of all samples were examined. The impact of the single site Pd doping on the amount of photocatalytic H_2 produced has been reported.

3.2. *Experimental*

3.2.1. Materials

All chemical reagents and solvents were purchased from commercial suppliers and and were used without further purification. KCl (≥ 99 %, Isolab Chemicals), $CaCO_3$ (98.5-100.5 mass%, pro analysis, Merck), $NbCl_5$ (99+ mass%, Merck), $PdCl_2$ (crystalline soluble, Alfa-Aesar), Methanol (≥ 99.8% ACS Reagent), ethylene glycol (99.9%, WWR Chemicals) and Citric acid (Anhydrous, Sigma-Aldrich), Potassium sulfate, K_2SO_4 (≥ 99.0% for analysis), Tetrabutylammonium hydroxide (~40% in water, Sigma-Aldrich), and Polyethyleneimine (branched average Mw ~25 000 BY LS, average Mn ~10 000 by GPC, Sigma-Aldrich) and Hydrochloric Acid Fuming 37%. Milli-Q UV filtered ultrapure water (≥18.2 MΩ·cm) was used in the experiments.

3.2.2. Synthesis of Catalysts

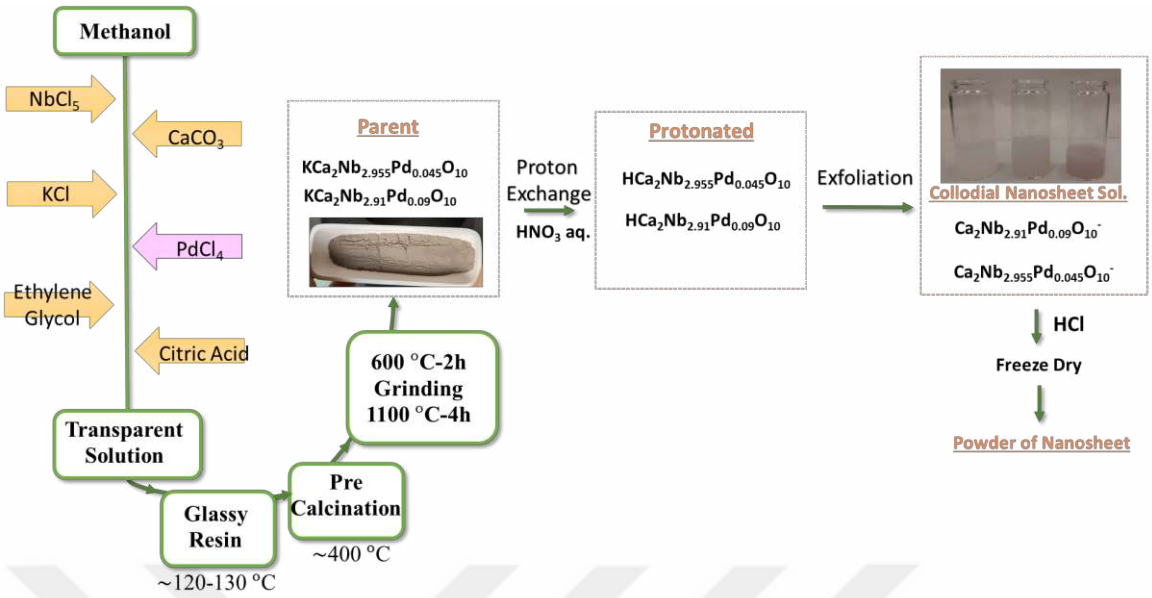

Figure 3.1: Synthesis steps of undoped and Pd doped (1.5% and 3%) photocatalysts.

$KCa_2Nb_3O_{10}$ was prepared by the polymerized complex (PC) method. The all steps of synthesis are given in Figure 3.1. Initially, stoichiometric amounts of $NbCl_5$, $CaCO_3$, and KCl were dissolved in 100 ml methanol in the presence of ethylene glycol. After complete dissolution of the salts, anhydrous citric acid in methanol were added to the solution under continuous stirring. The reaction mixture was heated at ~80 °C to achieve complete dissolution. To compensate for volatilization during the calcination, an excess of KCl (10 mol% K) was added to the solution. The as-obtained transparent solution was heated to ~120-130 °C to promote esterification between EG and CA, yielding a glassy resin. The resin was pre-calcined in the air at ~ 400 °C. After that, it was further heated at 600°C for 4 hours in air to get rid of the residual carbon-containing species. Finally, the resulting powder heated in air at 1100 C for 2 h in an Al_2O_3 crucible (ramp rate: 5 °C min^{-1}).

The single site Pd metal doped $KCa_2Nb_3O_{10}$ were prepared by using the same method except $PdCl_2$ salt was added into the initial solution. The stoichiometry of $PdCl_2$ and $NbCl_5$ was adjusted in a way that the stoichiometric amount of Pd is 1.5 and 3.0% of Nb in the structure. The compositions are $KCa_2Nb_{2.955}Pd_{0.045}O_{10}$ and $KCa_2Nb_{2.91}Pd_{0.09}O_{10}$.

3.2.3. Protonation and Exfoliation of $KCa_2Nb_3O_{10}$

All undoped and doped powders were placed in a solution of 5 M aqueous nitric

acid for 3 days. In a typical synthesis 0.5 gr of a powder was mixed in 20 ml of 5 M HNO_3 solution and was shaked on a shaker for 3 days. The acid solution was replaced daily with a fresh solution. Protonated powders ($HCa_2Nb_3O_{10}$) were isolated by centrifugation, washed with pure water to pH=7, and finally dried at room temperature overnight.

To obtain colloidal nanosheets, these protonated powders were separated into layers using an exfoliation method. The 0.25 gr of protonated powders were mixed in 7.3mmol/dm^3 Tetrabutylammonium hydroxide (TBA^+ OH^-) aqueous solution so that the OH^-:H^+ ratio is 1:1 for exfoliation.

The mixtures were subjected to shaker-assisted exfoliation at a speed of 150 rpm for 7 days, resulting in the formation of colloidal nanosheet suspensions. The solution was left for 24 hours to allow the unexfoliated particles to precipitate, and then the top of the colloidal solution was collected. The photographic images of colloidal solutions are given in Figure 3.2.

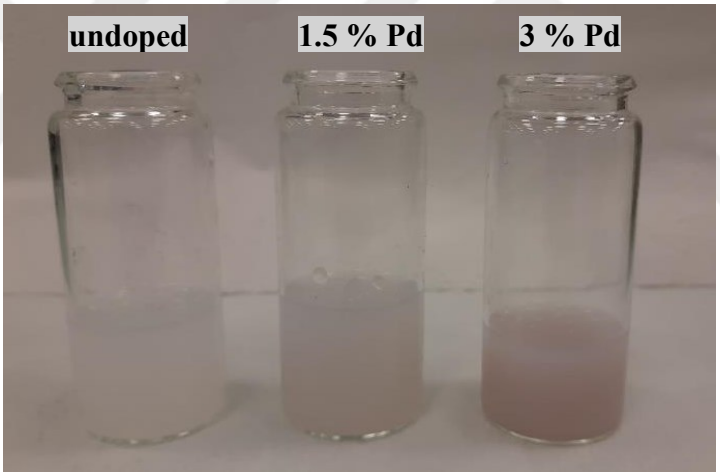

Figure 3.2: Colloidal nanosheet solutions of undoped, 1.5%Pd and 3%Pd doped samples

The nanosheet colloids were restacked by adding a small amount of 2.5 M aqueous hydrochloric acid into the colloidal solution. The produced restacked nanosheet powder was thoroughly washed with distilled water to eliminate any remaining traces of TBA^+ , Cl^- and H^+. After that, the powder was freeze-dried overnight.

3.2.4. Preparation of Films

In the photoelectrochemical experiments, as-synthesized powder, and the other derivations of parent powder (protonated powder, and restacked nanosheets) were applied as coatings onto fluorine-doped tin oxide (FTO with 7 Ω sq^{-1} surface resistivity and

~80% transmittance) coated glass substrates. The film of parent and protonated powders were prepared by the electrophoretic deposition method (EPD), whereas the single layer of 2D nanosheets were coated onto the substrate using the dip coating technique.
Before coating, FTOs were cleaned in ethanol for 10 minutes and then in distilled water (Milli-Q filtered ultrapure water >18 MΩ cm) for 10 minutes in an ultrasonic bath. The FTO substrates were dried in an oven at 80 °C.

A mixture of 10 mg of the powders and 5 mg of iodine (Sigma-Aldrich, 99.8% ACS reagent) was ultrasonically dispersed in 30 mL of acetone within a beaker for electrophoretic deposition. The FTO-coated glasses were used as both the cathode and the anode. The cathode and anode were placed approximately 1 cm apart, and the deposition process was performed at 100 V for 3 minutes utilizing a DC power source (RIGOL DP811). Following the coating, the films were rinsed with deionized water to remove excess iodine before being dried under a N_2 flow.

Regarding the dip coating method, the cleaned FTO substrates were pre-treated in an aqueous solution of PEI (2.5 g/L) for 15 minutes. Following that, the PEI-coated FTO substrates were immersed in the nanosheet colloid (0.5 mg/mL) for 15 minutes before being rinsed with deionized water. The films were dried in blowing N_2.

3.2.5. Structural Characterization

X-ray diffraction analysis was carried out with a Rigaku Mini Flex 600 X-ray diffractometer. The diffractometer produced X-rays from Cu anode Kα radiation (λ=1.5406 Å) at 40 kV beam voltage and 15 mA current. The XRD patterns were measured between 2°-80° 2-theta (2θ), at scanning rate $5°\cdot s^{-1}$. The ICDD PDF4+ database were used to analyze the purity and phases in the samples.

X-ray photoelectron spectroscopy (XPS) analysis was performed using a Thermo Scientific K-Alpha Spectrometer with an Al K (1486.6 eV) source. Thermo Avantage v5.973 was used to deconvolute the collected XPS data. All XPS spectra were adjusted for any shifts due to charging at 284.5 eV according to C1s.
FESEM images were captured using a Zeiss Ultra Plus field emission scanning microscobe. Secondary electron and in-lens detectors were utilized for imaging. an accelerating voltage of 5.00 – 10.00 kV and working distances of 5.4 to 5.8 mm were favored.

The ultraviolet-visible diffuse reflection absorption spectra (UV–vis) were

collected by a Shimadzu UV-3600 UV-VIS-NIR Spectrophotometer equipped with an integrated sphere. $BaSO_4$ plates were used as a reference. The UV-Vis data were taken as a function of the wavelength of the light reflected from the sample (reflectance mode), then they converted to absorption spectra by using Kubelka-Munk function. The band gap energies of the samples were also obtained from the Tauc plots (αhν vs. hν).
Raman spectroscopy measurements were taken with a Renishaw in Via Raman Microscope with a 633 nm laser as an excitation source.

3.2.6. Photoelectrochemical Characterization

All photoelectrochemical measurements are conducted in a typical three-electrode electrochemical cell. A Pt wire used as a counter electrode and Saturated Calomel Electrode (SCE, sat'd KCl) as a reference electrode. A working electrode was coated on 1 x 2.5 cm FTO glass. The electrolyte was 0.5 M K_2SO_4 aqueous solution purged with Argon for 20 min before each experiment. A 300 W Xenon lamp (Newport, 66901) was used to illuminate the sample. All photoelectrochemical measurements were performed by Princeton Applied Research VersaSTAT MC electrochemical workstation, of which set-up is given in Figure 3.3.

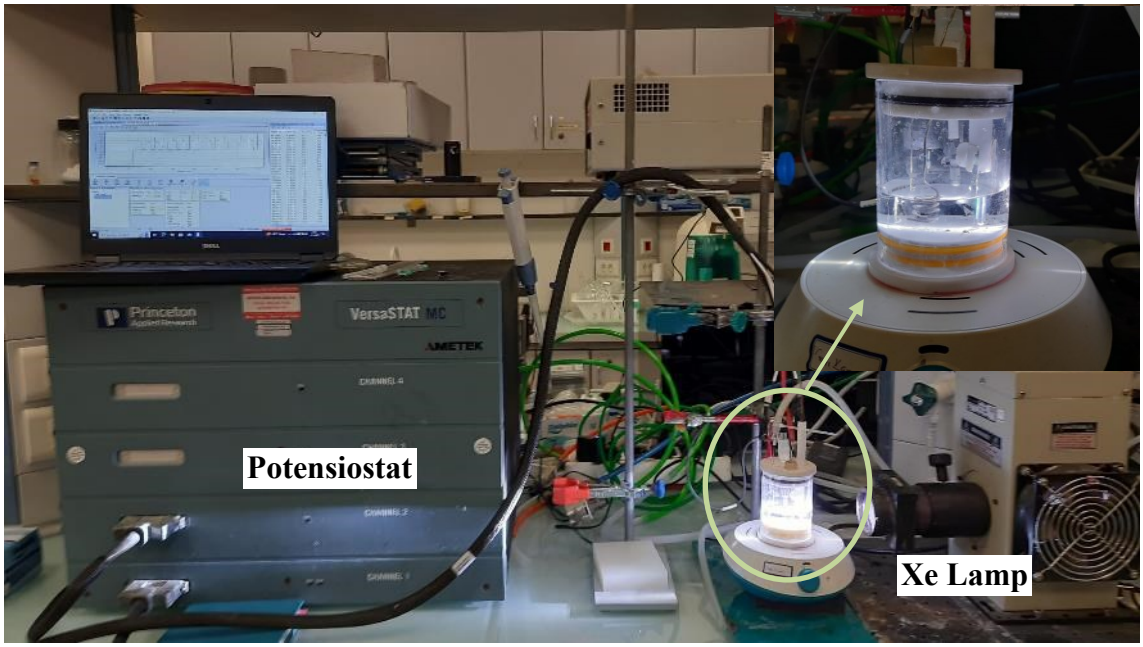

Figure 3.3: Photoelectrochemical Experiment Setup

Chronoamperometry (CA) and Linear Sweep Voltammetry (LSV) techniques were used to examine the photocurrent response of the films deposited from samples. Chronoamperometric transient photocurrent response of the samples were analyzed under chopped illumination at a fixed potential of 1.2 V vs saturated calomel electrode (SCE).

3.2.7. Photocatalytic Characterization

Photocatalytic setup is given in Figure 3.4. Photocatalytic reactions were carried out in 10 ml quartz cell with cooling bath jacket to keep the temperature constant at 25-30 ^{o}C. Furthermore, the suspension stirred during experiment and cooling bath was used to prevent any thermal catalytic effect. 300 W Xe lamp used as light source. In each experiment, 10 mg of the powder was suspended in a 5 ml aqueous solution containing methanol (10% v/v) as a hole scavenger. Before the irradiation, system degassed with Argon gas to remove the dissolved O_2 from the solution. The amount of H_2 gas product was analyzed by gas chromatography (Shimadzu, GC-2014 with a TCD detector and an MS-5A column, argon carrier gas). All experiments were performed for 6 hours by taking injections from the headspace of cell every 1 h using a gastight syringe (Figure 3.5).

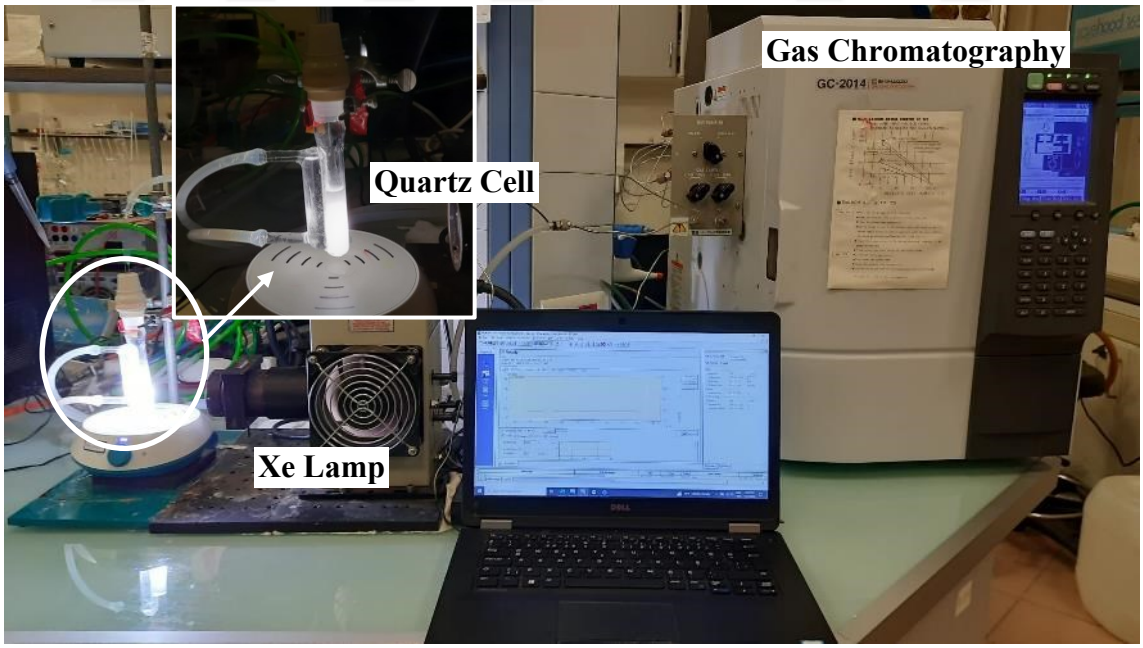

Figure 3.4: Photocatalytic Water Splitting Experiment Setup

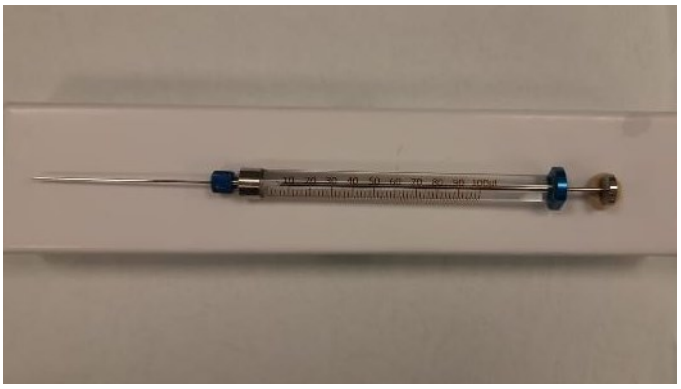

Figure 3.5: Gas Tight Syringe

3.3. *Results and Discussion*

3.3.1. X-ray diffraction (XRD)

The powder XRD patterns of the parent ($KCa_2Nb_3O_{10}$) and proton exchanged ($HCa_2Nb_3O_{10}$) compounds are shown in Figure 3.6.

In the XRD pattern of layered materials, (*00l*) reflections are typically observed at low theta angles. This reflection might reveal the distance between two adjacent layers.[129] The replacement of K^+ ions from the interlayer and the insertion of hydronium (H_3O^+) ions after the proton exchange reaction raised the c-lattice parameter of the $KCa_2Nb_3O_{10}$ (KCNO) structure, causing the *(00l)* reflection to move to lower 2θ values [129]. The $HCa_2Nb_3O_{10}$ (HCNO) diffraction pattern of 3%Pd doped sample given in Figure 3.7 as a representative sample. XRD pattern of 3% Pd doped $HCa_2Nb_3O_{10}$ shows a shift to lower 2θ angles in the (002), (004), and (006) reflections (Figure 3.7) which can signify the expansion of the interlayer distance with water intercalation as a result of ion exchange process[78], [116]. The peak shift was observed for all samples after proton exchange.

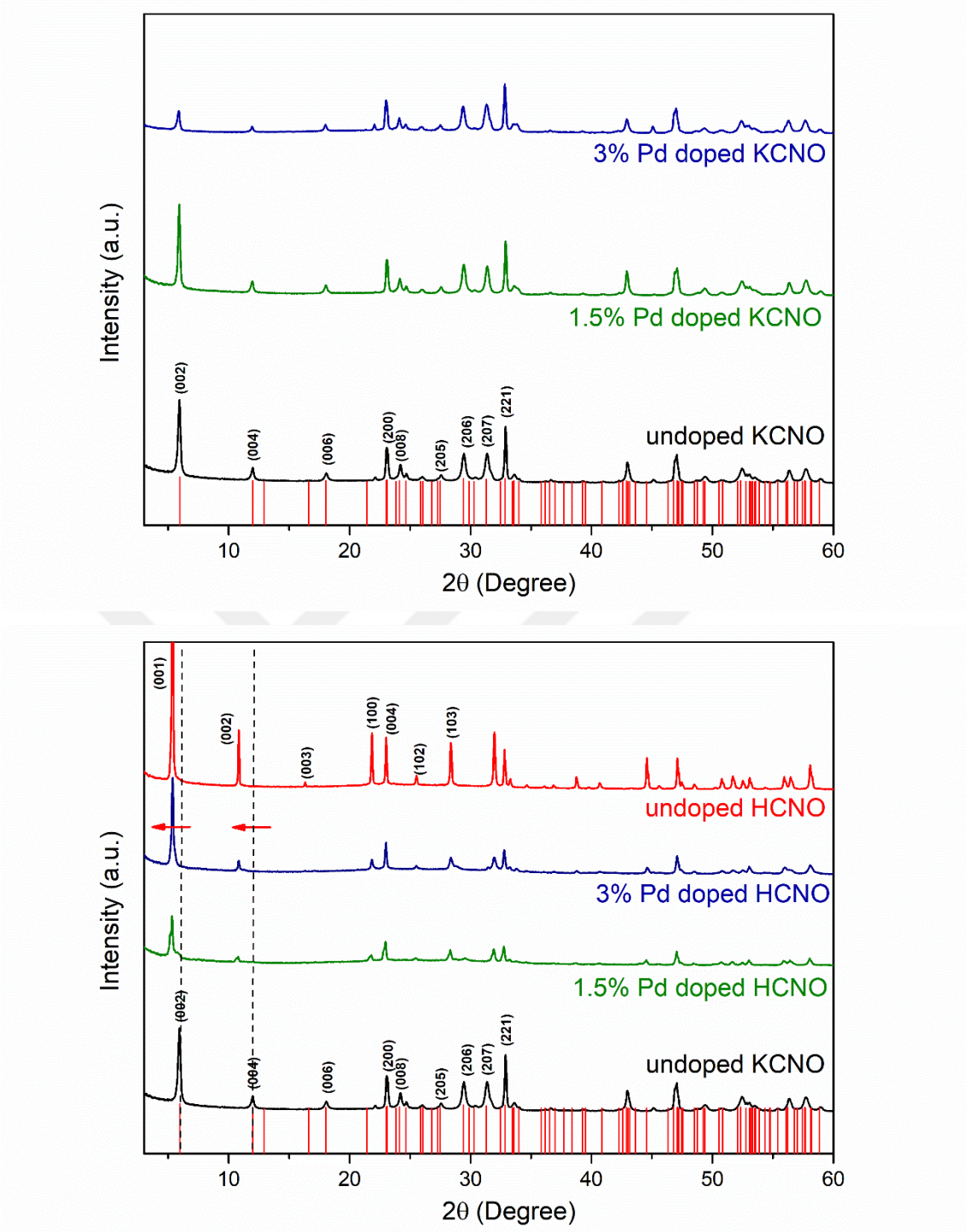

Figure 3.6: XRD patterns of undoped, 1.5% Pd and 3%Pd doped $KCa_2Nb_3O_{10}$ phase and their protonated versions ($HCa_2Nb_3O_{10}$). Literature data on $KCa_2Nb_3O_{10}$ and $HCa_2Nb_3O_{10}$ (ICDD PDF4+ database, minor intensity reflections included) are marked with red sticks correspondingly.

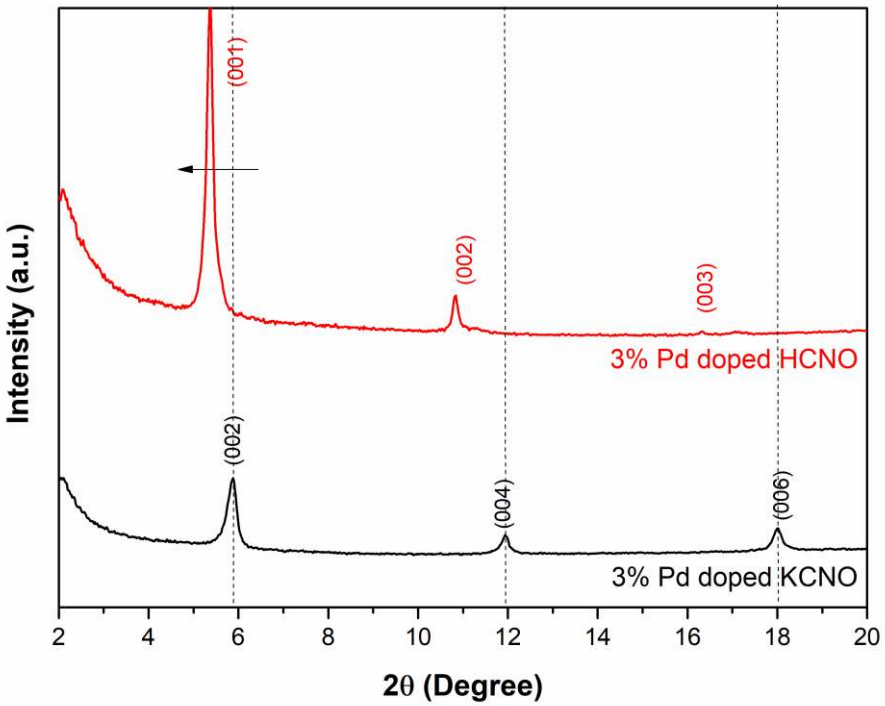

Figure 3.7: The peak shift belongs to 3%Pd doped sample in (002), (004), and (006) reflections after the proton exchange process.

XRD peaks of 1.5% and 3% Pd-doped phase highly overlap with the undoped KCNO phase and exhibited no extra peaks when compared to the undoped KCNO phase. In six-coordination geometry, ionic radii of Nb (5^+) and Pd (2^+) are 0.780 Å and 1.00 Å respectively. Because of difference of ionic radii, when Nb is replaced by Pd, it did cause a change in the interplanar spacing. As a result of this change influencing the crystallographic planes associated with NbO_6 octahedrons in the crystal structure, which are mainly (220) and (200) planes, a corresponding shift in the X-ray diffraction (XRD) peaks occurs. When an atom with a larger atomic radius, such as palladium (Pd), substitutes niobium, it leads to an expansion in the corresponding planes. Consequently, the relevant peaks in the XRD pattern shift towards lower 2theta angles as given in Figure 3.8.

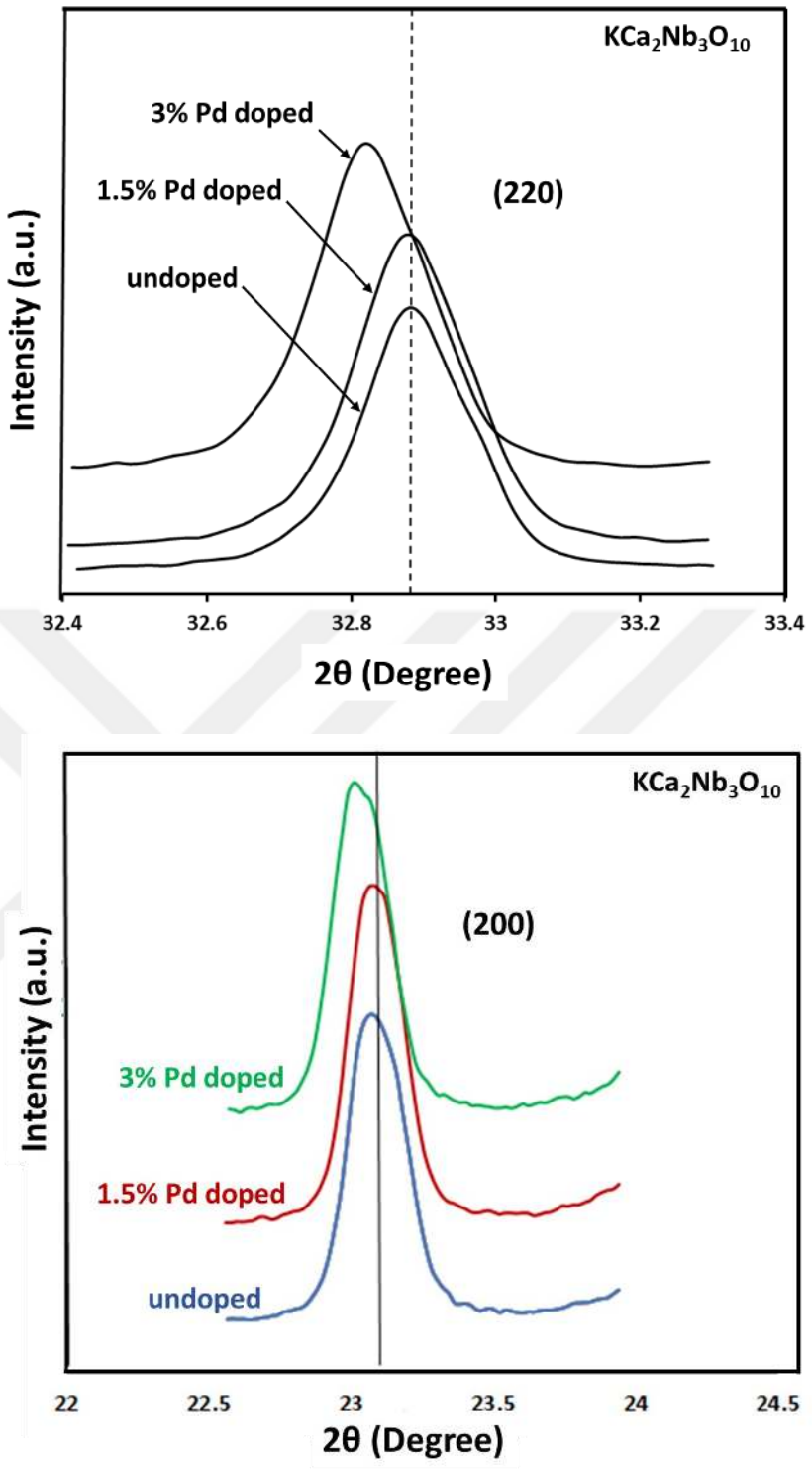

Figure 3.8: The relative peak shift in (220) and (200) peaks of $KCa_2Nb_3O_{10}$ with respect different ratio of Pd-doping concentrations.

The shift for 3% Pd doped $KCa_2Nb_3O_{10}$ sample showed more pronounced shift in comparison to 1.5% Pd doped sample. In accordance with the Raman and UV-vis spectra data, we can claim that Pd was successfully doped on Nb (5^+) (B-site) of the layered perovskite.

SEM images of 1.5% and 3% Pd-doped $KCa_2Nb_3O_{10}$ phase given in Figure 3.9. The SEM images are in the form of agglomerated plate as for $KCa_2Nb_3O_{10}$ in accordance with the literature [130] .

When the nanosheet powder is examined, nanoflake-like structures with a high surface area, resembling crumpled paper, are observed. No metallic Pd particles were detected in the SEM images of the Pd-doped samples and Pd dope did not cause any change in morphology. This can be interpreted as evidence that Pd has been incorporated into the structure as a single site.

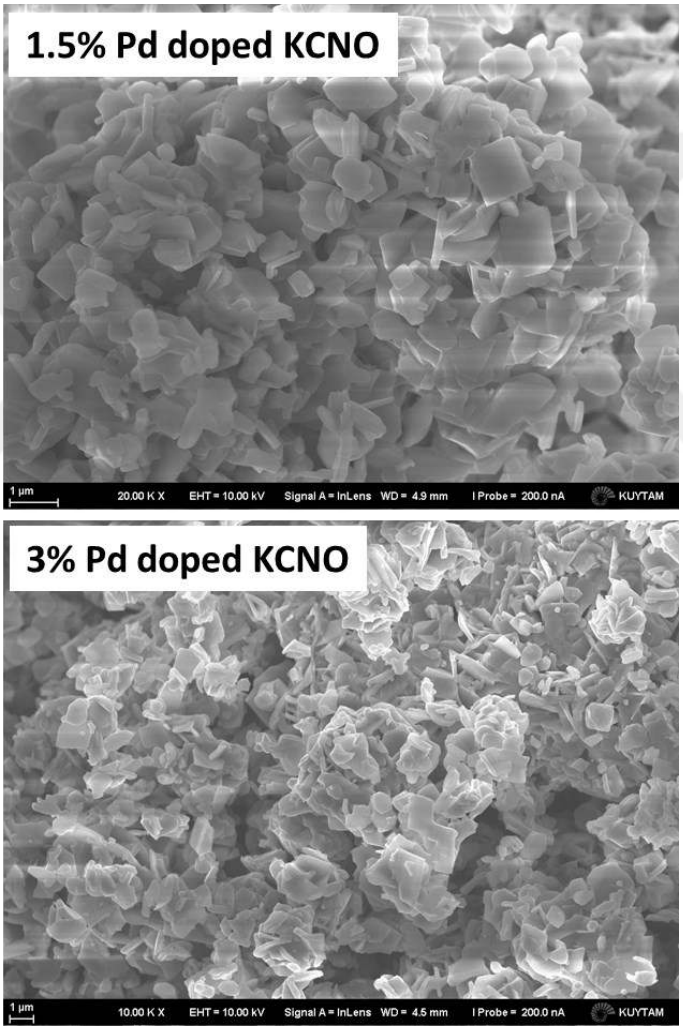

Figure 3.9: SEM images of 1.5%, and 3% Pd doped $KCa_2Nb_3O_{10}$.

3.3.2. X-Ray Photoelectron Spectroscopy (XPS)

The X-ray photoelectron spectroscopy of undoped and doped samples were taken to determine whether the proton exchange reaction and Pd doping were successful or not.

As it can be seen in the K2p spectra of all samples in the Figure 3.10 the proton exchange reaction was successful as no K2p peak was observed for the protonated form of the undoped, 1.5% Pd doped and 3%Pd doped samples. We can claim that all K^+ cations in the interlayer were exchanged with H^+ or H_3O^+ ions. The Figure 3.11 shows the Pd3d spectra of 1.5% and 3% Pd doped samples in the proton exchanged form. It is evident from the XPS spectra that Pd exist in the structure of the protonated layered perovskites in the oxide form, which is in accordance with the Raman spectrum data. In addition, the peak intensity of Pd3d spectrum increases when the dope amount increased from 1.5% to 3%. It is worth to mention that the XPS data in the Figure 3.10 belongs to the proton exchanged form of the samples. Existence of the Pd3d peaks in the XPS spectra of the proton exchanged powders clearly reveals that the proton exchange reactions in highly acidic environment did not change the chemical state of Pd atoms and did not result in leaching of Pd atoms. The XPS spectra proves that Pd was successfully doped into the structure of the layered perovskite.

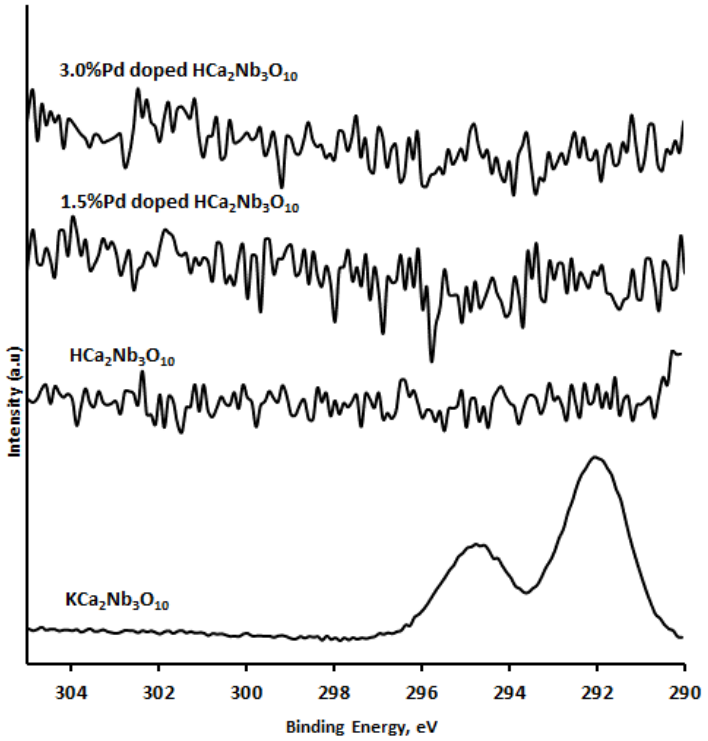

Figure 3.10: XPS spectrum of K2p peaks of $KCa_2Nb_3O_{10}$, $HCa_2Nb_3O_{10}$, 1.5% Pd doped $HCa_2Nb_3O_{10}$ and 3% Pd doped $HCa_2Nb_3O_{10}$.

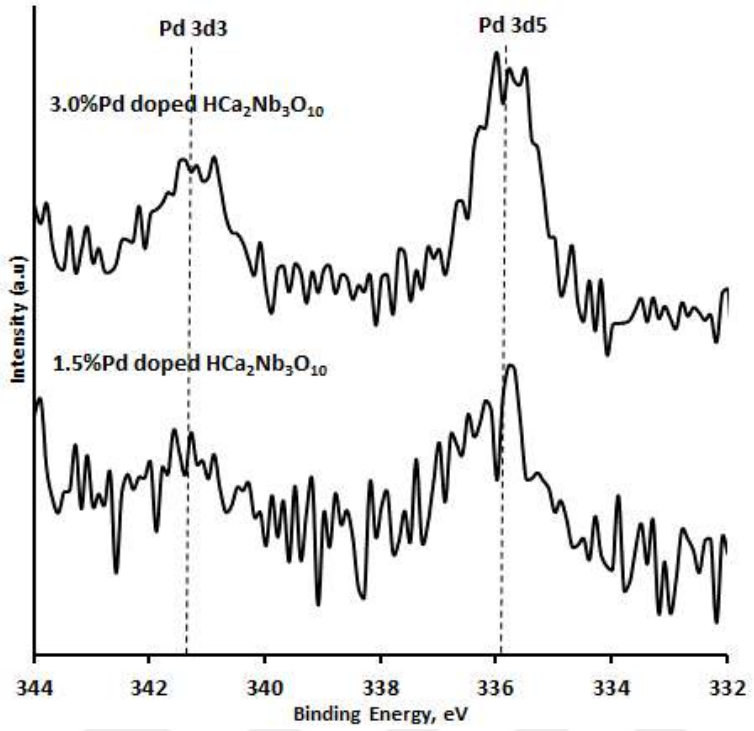

Figure 3.11: XPS spectrum of Pd 3d peaks of 1.5% Pd doped $HCa_2Nb_3O_{10}$ and 3% Pd doped $HCa_2Nb_3O_{10}$.

3.3.3. Raman Spectroscopy

The Raman spectra of undoped and 1.5% and 3% Pd doped $KCa_2Nb_3O_{10}$ and their protonated version ($HCa_2Nb_3O_{10}$) are shown in Figure 3.12. $KCa_2Nb_3O_{10}$ Raman peaks of niobate oxide was described by Jehng et al.[131]. The structure of triple-layered perovskites like $KCa_2Nb_3O_{10}$ consists of highly distorted outer NbO_6 octahedral layers and slightly distorted central NbO_6 octahedral. These highly distorted outer NbO_6 octahedral are associated with the band around 930 cm^{-1} for $KCa_2Nb_3O_{10}$. The bands with relatively lower intensity at 760 and 580 cm^{-1} are assigned to the slightly distorted central NbO_6 site modes. The bands below 400 cm^{-1} are assigned to external modes located in the alkali-metal layer.

The absence of the peak at 246 cm^{-1} in protonated $HCa_2Nb_3O_{10}$ suggests that the K^+ ions have been removed through ion exchange. This is inferred from the fact that vibrations in 100-300 cm^{-1} frequency range typically correspond to the transversal vibration of K^+ and Nb^{5+} ions [132].

It can be seen in the Figure 3.12 that Raman bands became broader and shifted to

higher wavenumbers after proton exchange process. Jehng [131] showed the in-situ Raman spectrum of the $Nb_2O_5.nH_2O$ structure with different water ratios. An increase in the intensity of the peak at around 930 cm^{-1} was observed as the water in the phase was removed. In addition, this peak shifted to higher wavenumbers with the removal of water. In reverse, an increase in the water ratio in the phase will lead to a shift of the peak towards lower wavenumbers, accompanied by a broadening and reduction in size. According to light of this information, the broader peaks in the Raman spectrum of $HCa_2Nb_3O_{10}$ indicate that the $HCa_2Nb_3O_{10}$ structure is more hydrated than $KCa_2Nb_3O_{10}$ phase. The broadening can be attributed to the increasing in interlayer distance due to the displacement of K^+ with H_3O^+ ions during the proton exchange process. This is further supported by the shift of the XRDs to lower 2θ angles, as lower angles indicate increased d-spacing [116] and SEM images of protonated samples.

Raman spectroscopy also confirmed the presence of PdO in Pd-doped samples. The Raman analysis revealed a sharp peak of PdO at 647 cm^{-1} which is strong B_{1g} mode of Pd-O vibration [133]–[135] in the presence of a Pd and this peak is not present in undoped Raman spectra of $KCa_2Nb_3O_{10}$.

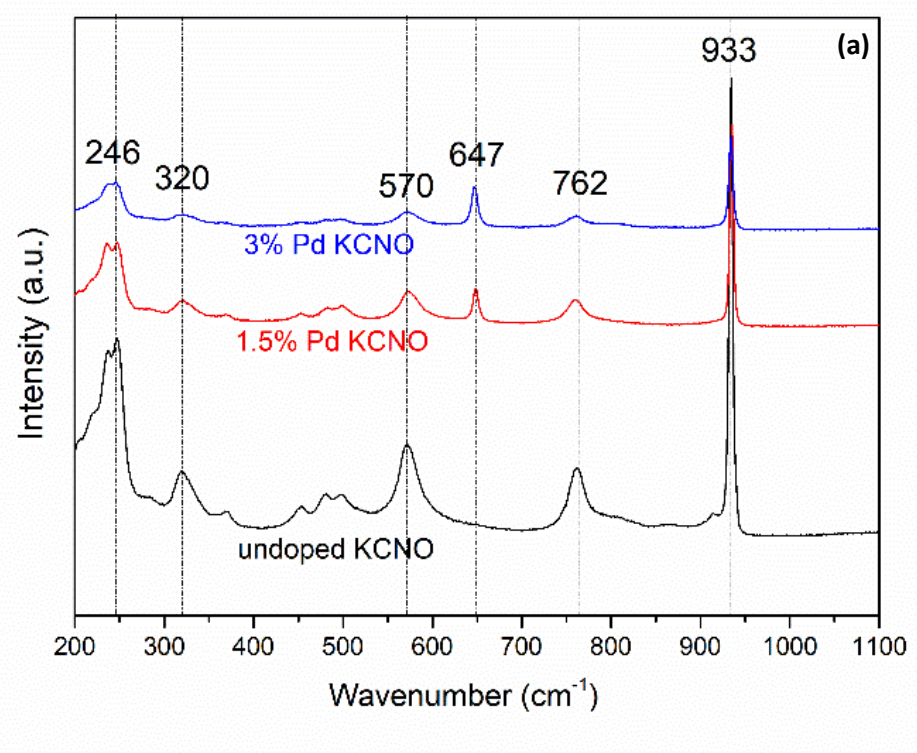

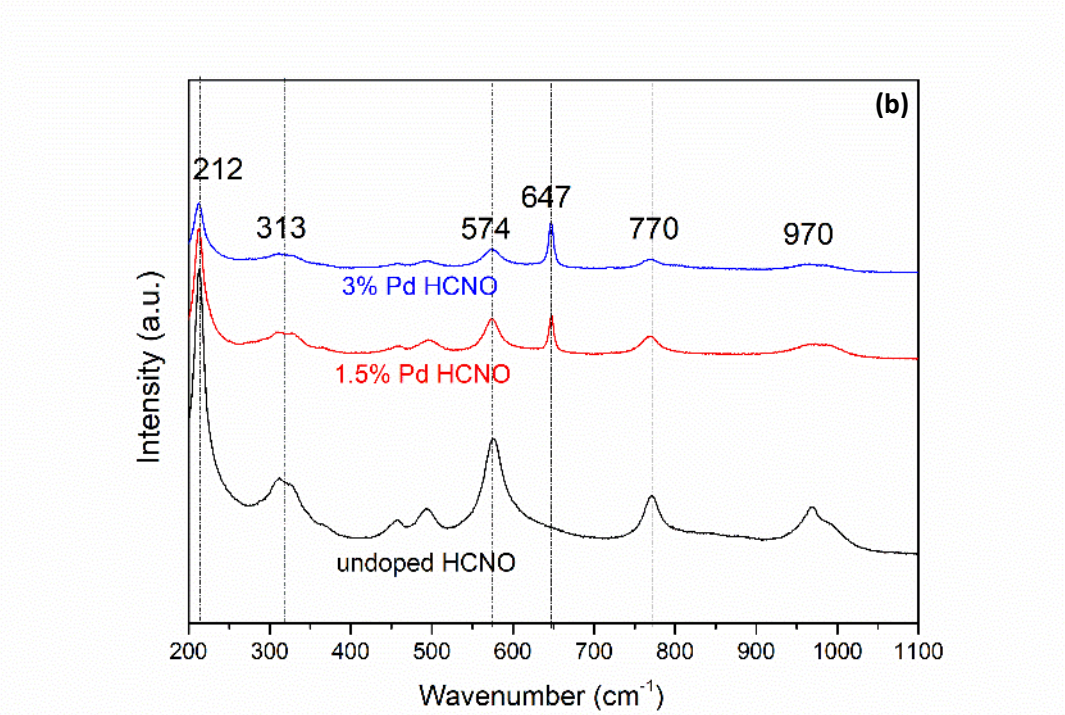

Figure 3.12: Influence of Pd doping on Raman Spectra of KCNO (a) and HCNO (b) samples.

Ascencio et al [136] analyzed the Raman spectra at 3 different wavelengths and reported that the peaks were better defined when the sample was measured with a 633 nm laser source. They reported that new peaks appeared at different frequencies, which could be a resonance effect. Therefore, Raman analysis was performed at 633nm.

With increasing percentages of Pd doping, the intensities of the peaks related to the Nb-O bonds in the Raman spectrum of the $KCa_2Nb_3O_{10}$ phase decrease, and the intensity of the Raman peak of PdO (647 cm^{-1}) increased. This indicates successful Pd doping in the structure.

3.3.4. UV-Visible Spectroscopy

UV-Vis diffuse reflection spectrophotometer and Tauc plots were used to investigate the optical properties of photocatalysts and determine their bandgaps. Diffuse ultraviolet-visible spectroscopy was employed to examine the optical adsorption characteristics of both undoped and Pd-doped samples, and the respective spectra are depicted in Figure 3.13. The figure illustrates that undoped $KCa_2Nb_3O_{10}$ exhibits distinctive ultraviolet light absorption owing to its inherent structural features [137].

Pd-doping causes a visible color shift from white KCNO powder to dusty pink and red violet powders for 1.5%Pd and 3%Pd, respectively. The absorption edge shows red shift along with the increasing amounts of Pd ratio. Therefore, the sample should have absorption in the visible light region. The results demonstrated that Pd single atom doping improved the visible light absorption of KCNO samples, and thus the photocatalytic activity could be increased by doped samples absorbing more visible light across the full spectrum.

DRS spectra of Pd-doped powders are given in Figure 3.14. When compared to the undoped powders indicate a strong absorption between 380-800 nm. Specifically, the large absorption tail provides a proof of the existence of oxygen vacancies [138]–[140] in the Pd-doped samples. Moreover, it can be concluded that the sample filled with 3% Pd contains more oxygen vacancies in comparison to the 1.5% Pd-doped sample. The increase in oxygen vacancies is also associated with the high electron concentration. [138]. It can be stated that Pd-doped photocatalysts are capable of absorbing a greater number of photons compared to undoped ones during the photocatalytic reaction.

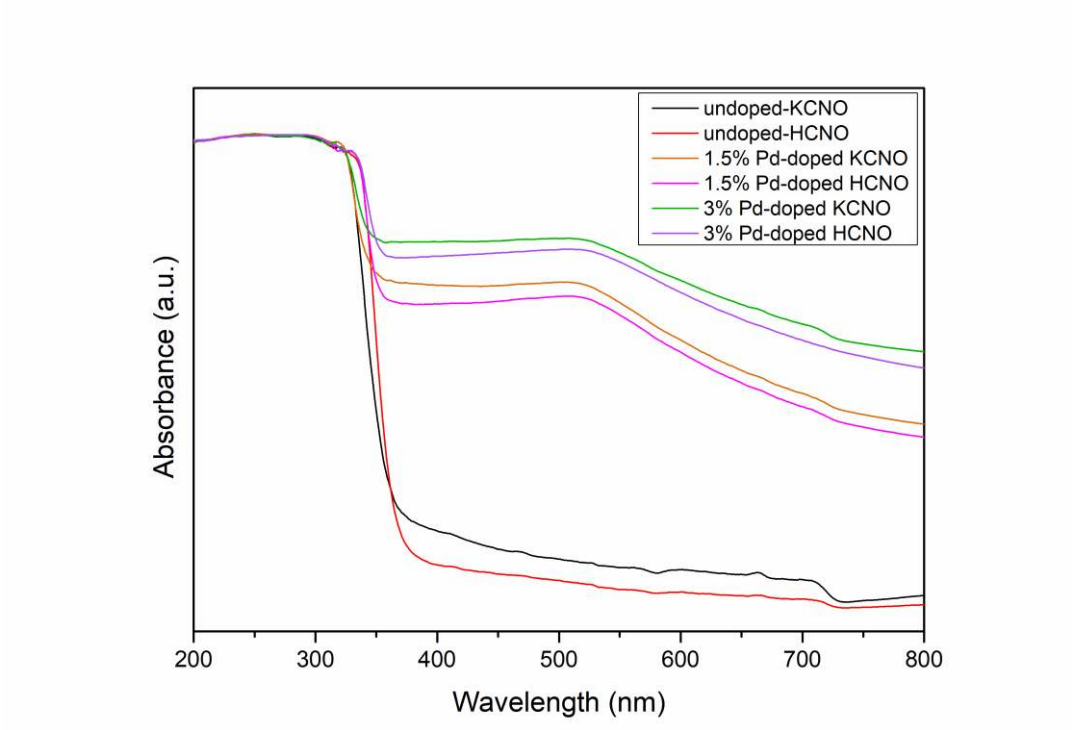

Figure 3.13: UV−vis diffuse reflectance spectra (DRS) of all as-prepared catalyst both version of KCNO and HCNO.

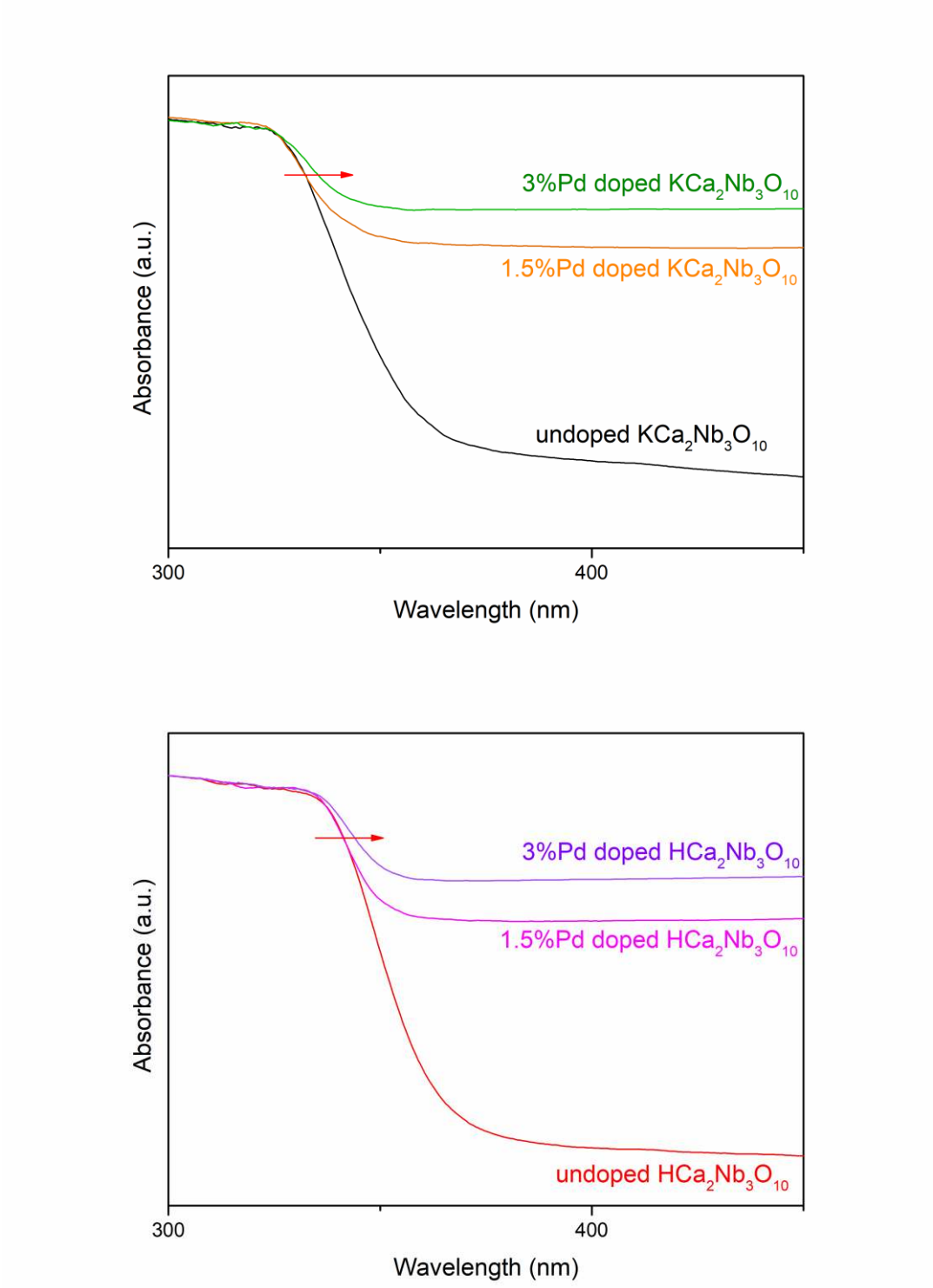

Figure 3.14: A slightly change of absorption band edges with Pd dope for 1.5% and 3% Pd doped KCNO and HCNO samples.

Single site Pd doped samples shows two absorption band. One at is around 330–530 nm due to the electronic transition from the valance band (O 2p) to conduction band (Nb 4d) and the other around 530–800 nm from background absorption which can be due to the formation of oxygen defects during Pd^{2+} substitution into the structure [141], [142].

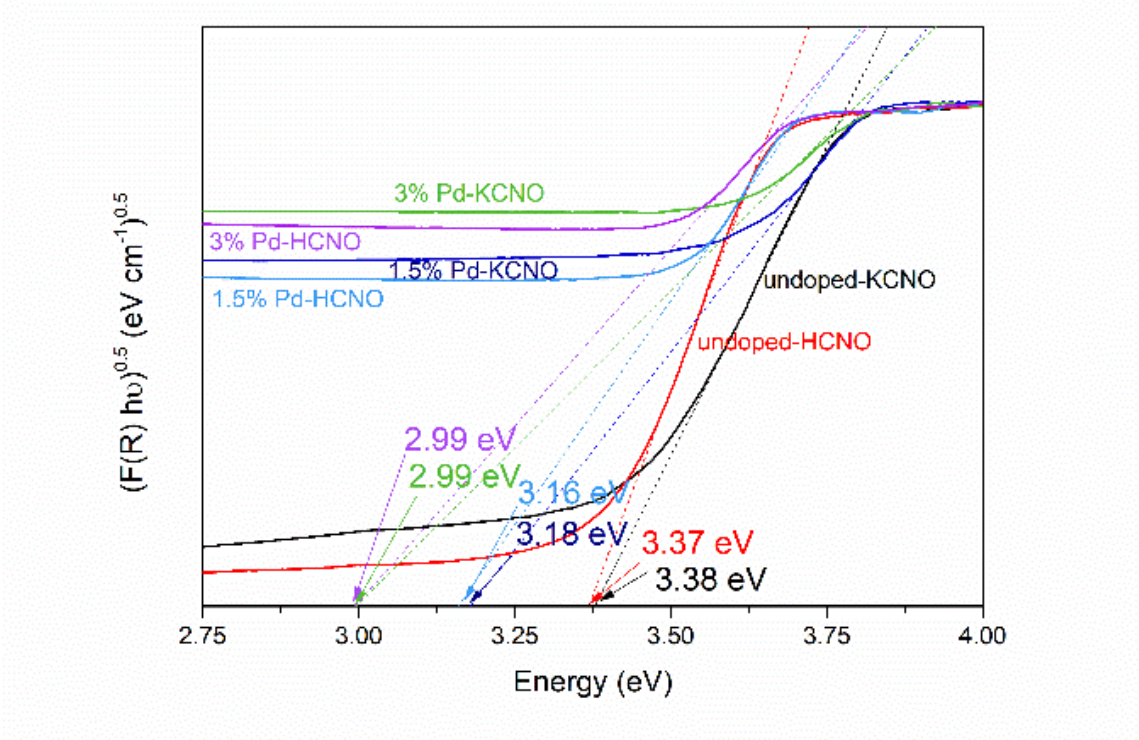

Figure 3.15: Tauc plot for determining the optical band gap (Eg) for all samples.

Figure 3.15 shows the Tauc plots of the parent $KCa_2Nb_3O_{10}$ and their proton-exchanged versions according to the direct bandgap feature of $KCa_2Nb_3O_{10}$.

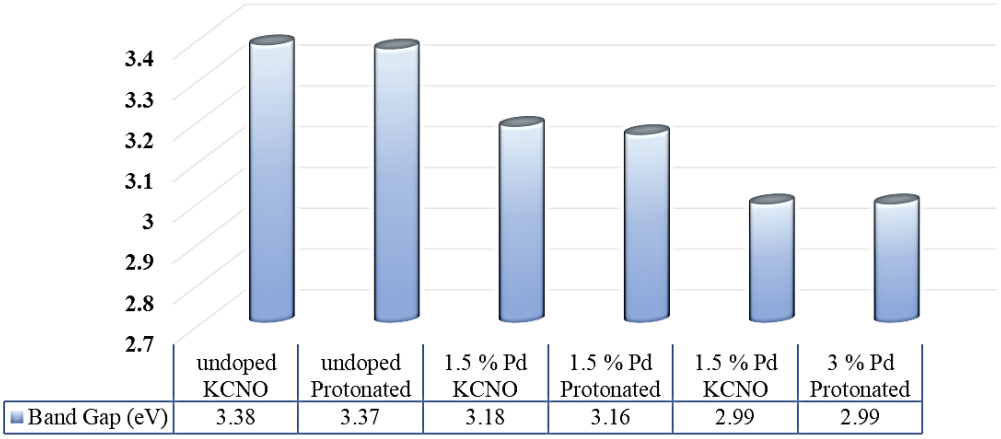

Figure 3.16: Band gap change of undoped, 1.5% and 3% Pd doped $KC_{a2}Nb_3O_{10}$ with proton exchange process.

The Figure 3.16 presents a comparison between the band gaps of all the samples calculated from Tauc Plots. It can be observed that the limited impact of the proton exchange process on the band gaps of the samples. However, the difference of Pd-dope ratio exhibits a significant influence, leading to a systematic decrease in band gap energy

as the Pd ratio increases. When we compared these samples, we observed a decrease of approximately 0.2 eV in the band gap with an increase in the Pd dope ratio. There is a shift of the bandgap from 3.38 eV for KCNO to 3.18 eV and 2.99 eV for 1.5% and 3%Pd doped parent KCNO samples, respectively. As illustrated in Figure 3.17, this narrowing of the band gap can be ascribed to the formation of bands containing energy levels from Pd 4d within the gap.

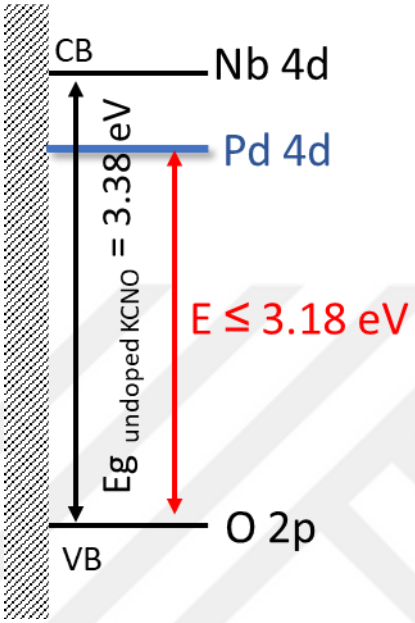

Figure 3.17: Representative image of effect of Pd doping on the electronic band structure of undoped KCNO.

Light absorption and electron and hole migration are essential factors regarding photocatalytic processes, which are influenced by a material's electrical structure. Photons are directly absorbed by the material's band gap in semiconductor photocatalysis, resulting in electron-hole pairs within semiconductor particles. A smaller band gap allows more photons to be absorbed, promoting electron excitation from the valence band to the conduction band [143].

The energy band structure of samples with the highest photocatalytic activity were constructed to understand the photocatalytic mechanism. XPS Valence band spectra was used for the determining valence band of samples given in Figure 3.18.

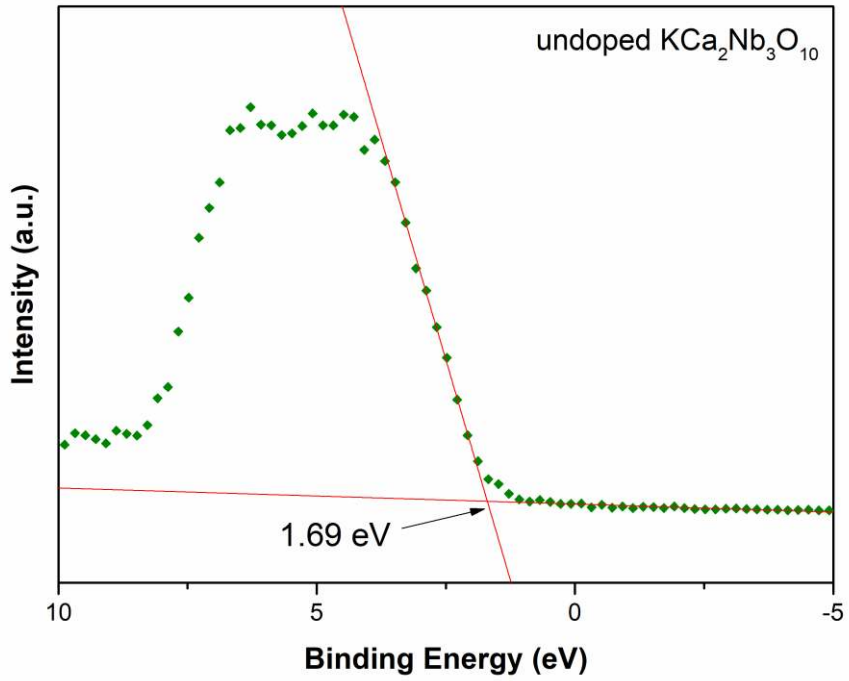
undoped $KCa_2Nb_3O_{10}$
Intensity (a.u.)
1.69 eV
10
5
0
-5
Binding Energy (eV)

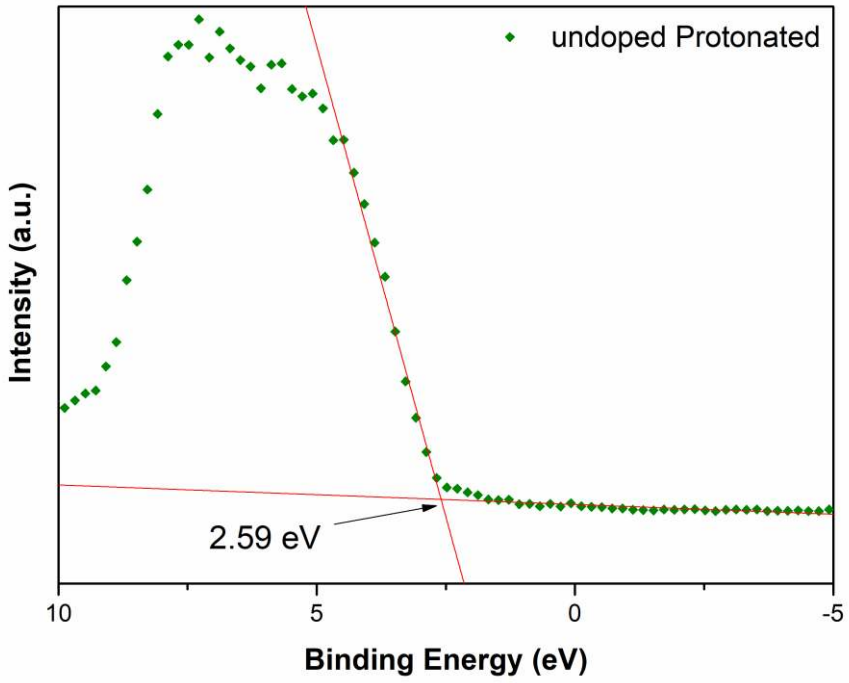
undoped Protonated
Intensity (a.u.)
2.59 eV
10
5
0
-5
Binding Energy (eV)

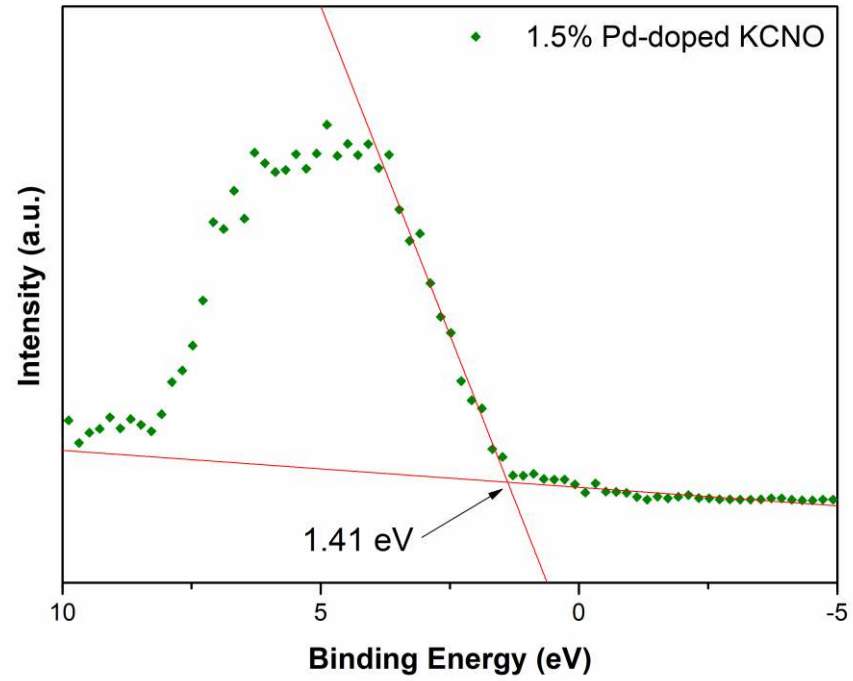
1.5% Pd-doped KCNO
Intensity (a.u.)
1.41 eV
10
5
0
-5
Binding Energy (eV)

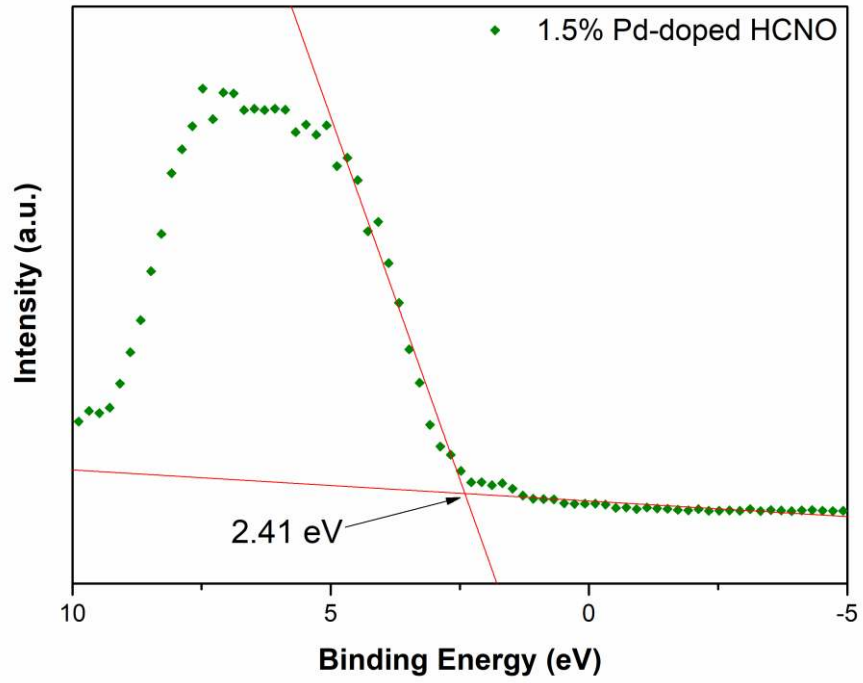
1.5% Pd-doped HCNO
Intensity (a.u.)
2.41 eV
10
5
0
-5
Binding Energy (eV)

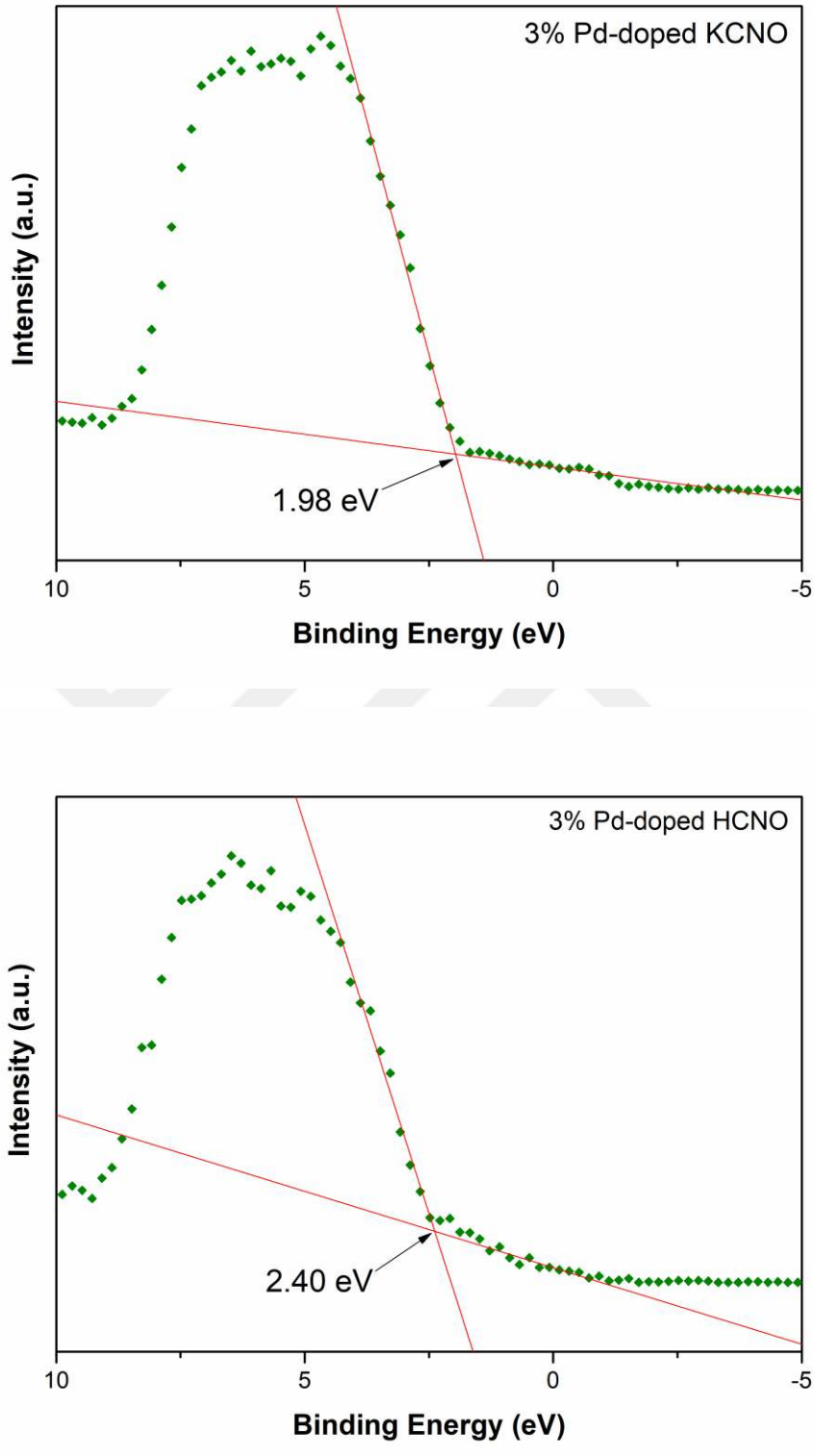

Figure 3.18 XPS Valence Band Spectra of undoped, 1.5% and 3%Pd doped KCNO and their protonated (HCNO) versions.

Combination of valence band potentials obtained from the XPS spectrum with the band-

gap energies, the position of conduction bands vs NHE were estimated. Estimated band structures of samples given in Figure 3.19. The potential of the valence band edge of KCNO becomes more positive and the conduction band edge shifts to more positive after the proton exchange process. Although 3% Pd samples have more positive conduction band values showed higher photocatalytic activity than the others. It can explain that a smaller band gap can compensate for a more positive conduction band position [126].

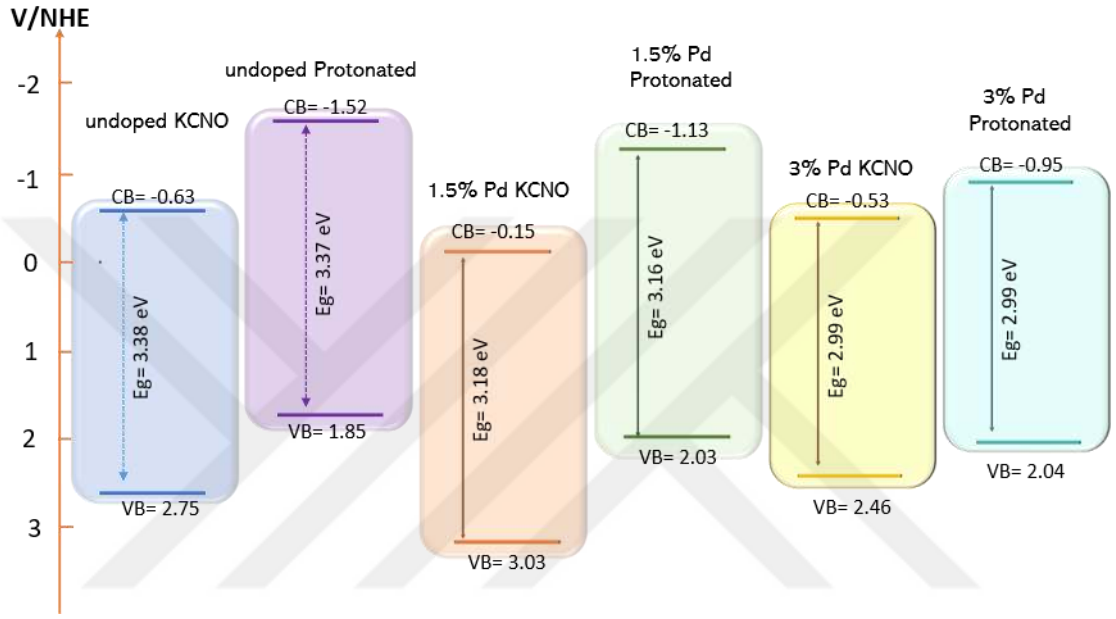

Figure 3.19: Schematic diagram of electronic band structure of undoped, 1.5% and 3% Pd doped $KCa_2Nb_3O_{10}$ and their protonated version.

3.3.5. Photoelectrochemical Measurements

Photocurrent experiments were performed to obtain information about charge carrier mobility and e-hole separation properties. Chronoamperometry analyses are shown in Figure . The photocurrent densities of all the samples have been evaluated under UV-light at 1.2 V vs SCE. It has been observed that the photocurrent density increases systematically from 1.5% to 3% with doping. This can be explained by the successful implementation of single site atom doping, which is one of the methods of increasing charge mobility [144]. Furthermore, increasing in the Pd ratio can be attributed to an increase in charge carrier density. Because Pd atoms doped into the structure as a single site act as active sites for reactions and leading to an increment in charge carrier density

[145]. In protonated samples, as the band gaps have remained almost same, the enhanced photocatalytic performance is most probably a result of improved separation of charge carriers.

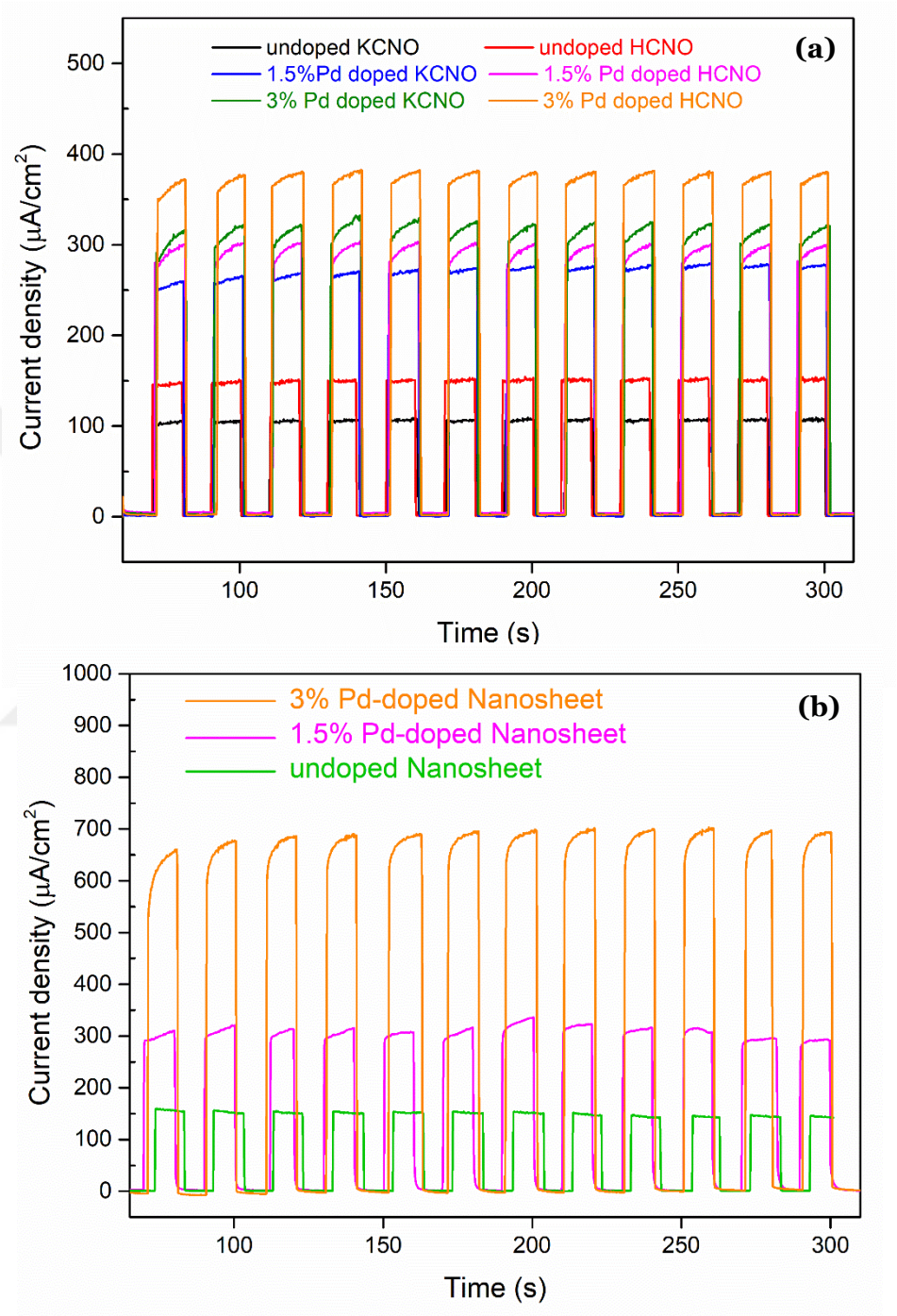

Figure 3.20: Chronoamperometry measurements of (a) parent and protonated versions of both undoped and Pd-doped samples and (b) all [CNO]- nanosheets samples.

In EIS, the diameter of the arc in a Nyquist plot indicates the amount of resistance to charge transfer at the critical interface between the electrode and the electrolyte [146]. A reduced arc, specifically, indicates decreased charge-transfer resistance, resulting in an environment that promotes more efficient movement of charge carriers, including electrons or holes [147]. An enhanced number of active sites on the semiconductor surface provides additional opportunities for carriers to engage in effective transfer. Furthermore, the addition of co-catalysts or dopants into semiconductor materials can enhanced conductivity, leading to reduced resistance during charge transfer.

EIS characterization was performed to investigate the charge transfer process taking place on the photocatalyst. EIS Nyquist plots of the Pd-doped nanosheet samples are shown in Figure 3.21. The 3%Pd doped nanosheet samples displayed a smaller arc than undoped and 1.5% Pd doped $[Ca_2Nb_3O_{10}]^-$. Similarly, with the increase in Pd amount, the arc diameter reduces, signifying lower resistance at the photoelectrode/electrolyte interface and improved charge transfer efficiency[148]. The increased Pd doping may have resulted in a higher number of active sites, leading to more effective charge transfer [149].

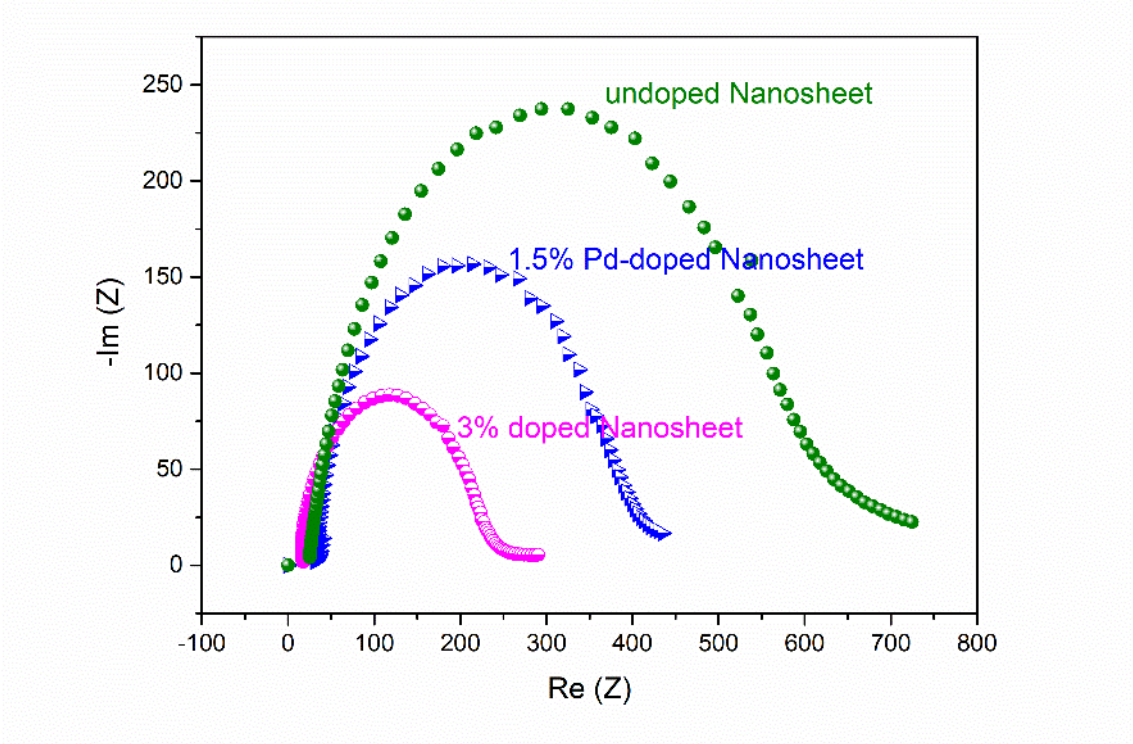

Figure 3.21: Electrochemical impedance spectra of undoped, 1.5% Pd doped and 3% doped $[CNO]^-$ nanosheets.

3.3.6. Photoluminescence

Time-resolved transient photoluminescence spectra were employed to investigate the dynamic electron migration process of the charges at the related steady-state emission peaks. As shown in Figure 3.22 the broad emission peaks around 545 nm can be observed in the PL spectra of KCNO and their protonated and nanosheets version under an excitation wavelength of 360 nm at room temperature.

The average radiative lifetimes of approximately 3.91, 3.45, and 2.89 for undoped, 1.5%, and 3% Pd-doped samples in aqueous suspensions respectively. We estimated the average radiative lifetimes by using time-correlated single-photon counting (TCSPC) as given in Figure 3.23. Decay curves were fitted exponentially to obtain the decay time. The shortest average weighted lifetime of 3% Pd doped KCNO indicates the fast migration and separation of photoinduced charge carriers namely the effective charge transfer [150]. The significant reduction in exciton lifetime strongly indicates a notable acceleration of photoexciton dissociation. This proves that the single site palladium serves as an extra active site for the separation of charges [151].

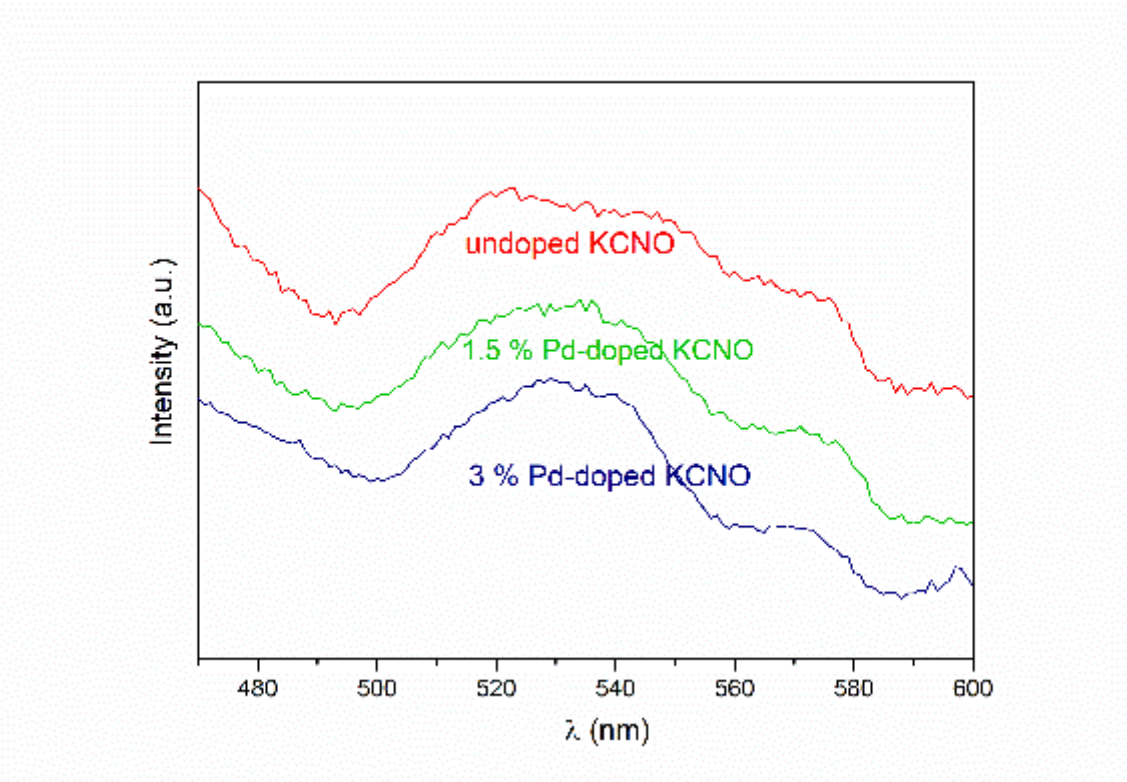

Figure 3.22: Fluorescence emission spectra of undoped, 1.5% Pd doped and 3% Pd doped

KCNO at room temperature ($\lambda_{excitation}$=360nm).

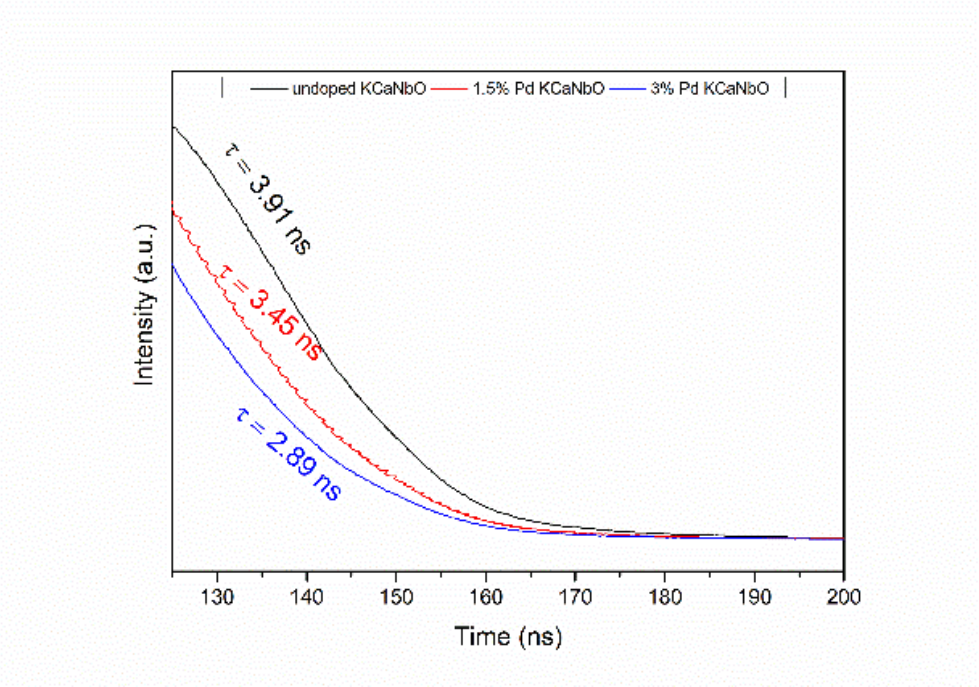

Figure 3.23: Photoluminescence decay lifetime curves of undoped, 1.5% Pd doped and 3%doped KCNO.

3.3.7. Photocatalytic Hydrogen Evolution Reactions

Figure 3.24 shows the results of photocatalytic H_2 evolution experiments carried out under full spectral range for 6-hour in the presence of 10% methanol without the use of any co-catalysts. The results indicate that the undoped parent layered structure had a low efficiency in photocatalytic HER (4.88 µmol/g). The addition of single-site Pd doping resulted in a significant increase in photocatalytic activity within the parent samples. Notably, when protonated samples were compared to parent samples, the former showed a dramatically increase in the catalytic activity. The amounts of H_2 obtained from protonated powders were 150.16 µmol/g, 461.17 µmol/g and 588.10 µmol/g for undoped 1.5% Pd doped, and 3% Pd doped samples after 6 hours, respectively. The protonated sample doped with 3% Pd produced nearly ten times more H_2 than the undoped parent samples. The exfoliated and restacked nanosheets exhibited even further increase in the H_2 production rate. As can be seen in the Figure 3.24, the nanosheets of 3% Pd doped layered perovskite produced approximately 3 times more H_2 than the proton exchanged and 30 times more H_2 than the parent materials. According to the results, the amount of

H_2 obtained from undoped, 1.5% Pd doped and 3% Pd doped nanosheets was 294.26 µmol/g, 1166.2 µmol/g and 1688.24 µmol/g, respectively. The result can be assigned to the availability more reactive sites since the exfoliation and restacking gives higher surface area. In addition, we can claim that all Pd sites on the nanosheets of the layered perovskite will be available in comparison to parent and proton exchanged photocatalyst in the powder form.

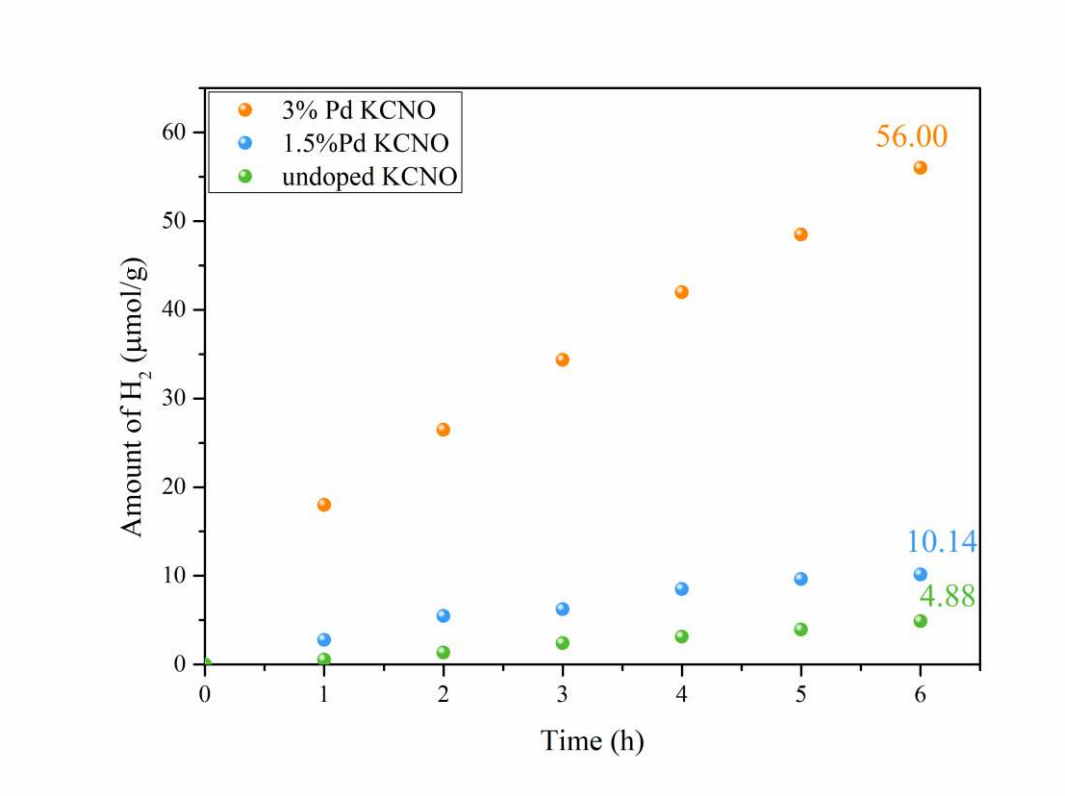

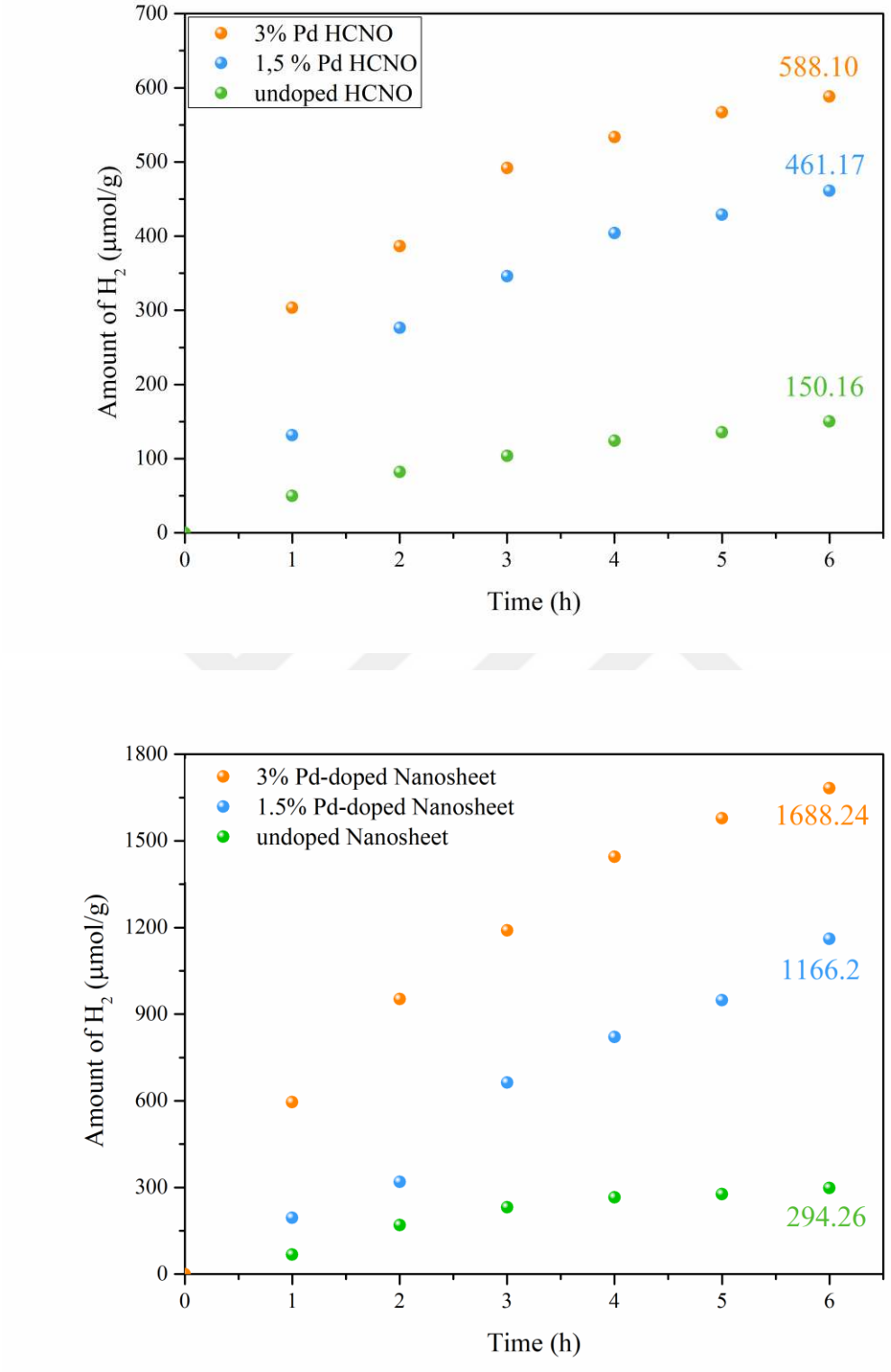

Figure 3.24: Photocatalytic hydrogen evolution rates on undoped and doped parent, proton exchanged and restacked nanosheets of $KCa_2Nb_3O_{10}$. The photocatalytic reaction was carried out in a 5 ml quartz cell in the presence of 10%v/v methanol under illumination with an unfiltered 300 W Xe lamp.

3.4. *Conclusion*

Undoped, 1.5% and 3% Pd doped $KCa_2Nb_3O_{10}$ phases were successfully synthesized by the Pechini method. Then, proton exchange was performed and protonated $HCa_2Nb_3O_{10}$ phase was obtained. Their morphological and optoelectronic characteristics, as well as their photoelectrochemical and photocatalytic hydrogen activity, were determined. XRD analyses are consistent with literature, indicating no significant change in crystal structure upon the doping of Pd. The observed shift of the XRD peaks can be attributed to the larger atomic radius of Pd compared to Nb^{5+}. The further shift observed with an increase in the Pd ratio confirms the successful doping of Pd on a single site within the structure. SEM results show similar morphology for the parent and protonated materials, presenting as plate-like particles. In the nanosheet version, the presented image displays nanoflakes with significant surface area, resembling crumpled paper. The absorbance properties were determined using UV-VIS spectroscopy. The electronic band structures were obtained from Tauc plot graphs, which were initially drawn using UV-Vis analysis data to acquire band gaps for band structure determination. Subsequently, valence band estimation was performed through XPS analysis for the valence band.

The results indicate that the undoped parent layered structure had a low efficiency in HER (4.88 μmol/g). The addition of single-site Pd doping resulted in a significant increase in photocatalytic activity within the parent samples. Notably, when protonated samples were compared to parent samples, the former showed dramatically increased photocatalytic activity. The amounts of H_2 obtained from protonated powders were 150.16 μmol/g, 461.17 μmol/g and 588.10 μmol/g for undoped 1.5% Pd doped, and 3% Pd doped samples after 6 hours, respectively. The protonated sample doped with 3% Pd produced nearly ten times more H_2 than the undoped parent samples. The nanosheets of 3% Pd doped layered perovskite produced approximately 3 times more H_2 than the proton exchanged and 30 times more H_2 than the parent materials. According to the results, the amount of H_2 obtained from undoped, 1.5% Pd doped and 3% Pd doped nanosheets was 294.26 μmol/g, 1166.2 μmol/g and 1688.24 μmol/g, respectively. The results showed that single site Pd doping, and exfoliation method are quite efficient ways to increase hydrogen production rates.

CHAPTER 4: EFFECT OF RUTHENIUM DOPING ON PHOTOCATALYTIC CO_2 REDUCTION

4.1 Introduction

The developing industry, the rapidly increasing world population and using of fossil fuels have also caused an increase in the amount of carbon dioxide in the atmosphere. The steady increase of CO_2 level led to many problems such as global warming and brings environmental problems with it. In recent years, the development of efficient and sustainable methods for mitigating CO_2 emissions has become a critical area of research. In this context, the quest for highly effective photocatalysts capable of transforming CO_2 into valuable fuels or feedstocks has gained significant attention. [152]–[156]

Researchers and industries are pursuing two main approaches to the challenge of reducing CO_2 emissions. Primarily, they aim to address CO_2 emission problems at the production level by reducing reliance on fossil fuels and investigating alternative energy sources, including solar, wind, biomass, geothermal, hydro, and biofuels, which are renewable, clean, and, crucially, do not generate harmful CO_2 by-products. Hence, the significance of moving towards clean energy to address the issue of CO_2 emission is apparent. The subsequent method focuses on trapping and employing carbon dioxide by converting it into valuable chemicals, for instance, carbon monoxide (CO), formic acid (HCOOH), methanol (CH_3OH), and methane (CH_4). This approach can efficiently curtail the amount of CO_2 in the atmosphere while creating fuels that can produce sought-after industrial products.

Recently, photocatalysis has gained popularity in converting CO_2. Furthermore, the energy used in electrochemical reduction comes from light, avoiding the generation of CO_2. Photocatalytic systems require low maintenance, making them suitable for large-scale implementation. Finally, in photocatalytic reduction, the reactants used are simple substances like water and CO_2, while the unused components (photocatalyst) can be reused, thus reducing cost and pollution. However, some drawbacks still exist in photocatalytic CO_2 reduction.

One of the significant problems is the decrease in photocatalytic activity due to the recombination of photogenerated electrons (e^-) and holes, which is referred to as recombination. Due to the linear structure of the CO_2 molecule, it needs to adopt a bent

conformation, $CO_2^{\bullet}$, to be activated during the photocatalytic reduction process. This requirement results in a significant energy barrier for the formation of the $CO_2^{\bullet}$ intermediate, leading to a substantial overpotential that reduces the energy efficiency of the process.

In the literature, semiconductor materials used for photochemical, electrochemical, and thermochemical conversion of carbon dioxide into useful chemicals such as CO, CH_4, CH_2O_2, alcohols, low and high hydrocarbons[157], [158]. Among these are perovskite oxides be noticeable attributable to their high activity, high thermal, mechanical and chemical stability as well as their easy modification of band gaps, photo excitation and the separation of electron-hole pairs[159], [160]Perovskite oxides can be categorized as Ruddlesden Popper (RP) phases[161], Dion Jacobson (DJ) phases[162], [163] and Aurivillius phases[164] where their general formulas can be written as $A'_2A_{n-1}B_nO_{3n+1}$, A' $[A_{(n-1)}B_nO_{3n+1}]$) and $(Bi_2O_2)(A_{(n-1)}B_nO_{3n+1})$, respectively ($A'$ = Cs, K, Li etc.; A = La, Ca, Sr, Bi; and B = Ti, Nb, Ta, etc.). In this study, we use the most typical member of the Dion–Jacobson-type layered perovskite niobates, $KCa_2Nb_3O_{10}$, as the host material.

Several strategies have been proposed to improve the photogenerated electron-hole pair separation performance and/or CO_2 capture capacity of layered perovskite oxide photocatalysts. These include metal co-catalyst loading [165], heterojunction construction [166], heteroatom doping [167], and defect engineering [168], [169].
Among these methods, the activity of photocatalytic activity relies strongly on both the cocatalyst and the chosen doping method or process. These cocatalysts play a vital role in generating active sites and facilitating the separation of charges. Many of co-catalysts dopants are used in perovskite oxides to enhance the photocatalytic activities. Almost all the dopants are present doped on the surface, rather than in the catalyst structure [170]–[172]. The strategic placement of Ru ions within the perovskite structure ensures optimal utilization of its catalytic activity, further enhancing the overall photocatalytic activity.
Another way to increase photocatalytic activities is to use materials with different morphologies. Developing its properties of perovskite oxides, 2-dimensional (2D) nanolayers wide use in various application areas such as photocatalysis, electrocatalysis, energy storage and sensors in the literature[173]–[177]. Their ultra-thin structure shortens the charge transfer time and distance, and the electron-hole recombination process could be retarded. Additionally, it is effective in the separation of electron-hole pairs produced by light and their transport to the electrode surface more easily.

In this chapter, photocatalytic CO_2 reduction performances and photocatalytic activities will be investigated by using ultrathin 2D layered Dion-Jacobson type perovskite oxide $KCa_2Nb_3O_{10}$ with single-site ruthenium doped. The findings presented in this study will shed light on the tremendous potential of ultrathin 2D layered Dion-Jacobson type perovskite oxide $KCa_2Nb_3O_{10}$ with single-site ruthenium doping as a promising photocatalyst for CO_2 reduction. This research holds significant implications for developing sustainable strategies to combat CO_2 emissions and foster a greener future.

4.2 Experimental

4.2.1 Materials

K_2CO_3 (ACS, 99.0% min, Alfa Aesar), $CaCO_3$ (98.5-100.5 mass%, pro analysis, Merck), Nb_2O_5 (99.9%, Sigma-Aldrich), RuO_2 (99.9% trace metal basis, Sigma-Aldrich), Potassium bicarbonate (ACS reagent, 99.7%), Potassium sulfate (≥ 99.0% for analysis), Tetrabutylammonium hydroxide (~40% in water, Sigma-Aldrich), and Polyethylenimine (branched average Mw ~25 000 BY LS, average Mn ~10 000 by GPC, Sigma-Aldrich) . All other chemicals were of reagent grade. Milli-Q filtered ultrapure water (>18 MΩ cm) was used throughout.

4.2.2 Synthesis of Catalysts

The layered perovskite oxide $KCa_2Nb_3O_{10}$ powders were prepared using analytical grade powders of $CaCO_3$, Nb_2O_5, K_2CO_3, according to the stoichiometric ratio (K/Ca/Nb= 1.2:2:3) as the starting materials by solid state method. The amount of K_2CO_3 was added 20 mol% excess to compensate for the loss of potassium due to volatilization during calcination. All materials were mixed by mechanical grinding in an agate mortar for 30 min. The obtained powder mixture calcined twice in alumina crucibles with intermediate regrinding, firstly at 650 °C in the air for 4 hours with a heating rate of 5° min^{-1} and natural cooling. Then, the second calcination was at 1150 °C in the air for 2 hours with a heating rate 10° min^{-1}. Similarly, in order to synthesize ruthenium-doped $KCa_2Nb_{(3-x)}Ru_xO_{(10-\delta)}$ (x=0.045, 0.09 and 0.15), the same starting materials and ruthenium oxide were prepared by mixing them by solid state method under same calcination conditions.

The obtained catalysts were treated in 5 M HNO_3 for 3 days for the proton exchange reaction. The acid was replaced with fresh acid every 24 h. After H^+ exchange

process, the catalyst powders were washed with water until the pH was about 7 and dried in air. An exfoliation process was performed to obtain nanosheets by separating these protonated forms of catalysts into layers. Tetrabutylammonium hydroxide (TBA^+ OH^-) aqueous solution was used with a 1:1 ratio of OH^- and H^+ for exfoliation. These mixtures were shaken in a shaker at a speed of 150 rpm for 7 days. Colloidal nanosheet suspensions were obtained after exfoliation. The solution was left for 24 hours for precipitation of the unexfoliated powders, and then the top of the colloidal solution was collected as given in Figure 4.1.

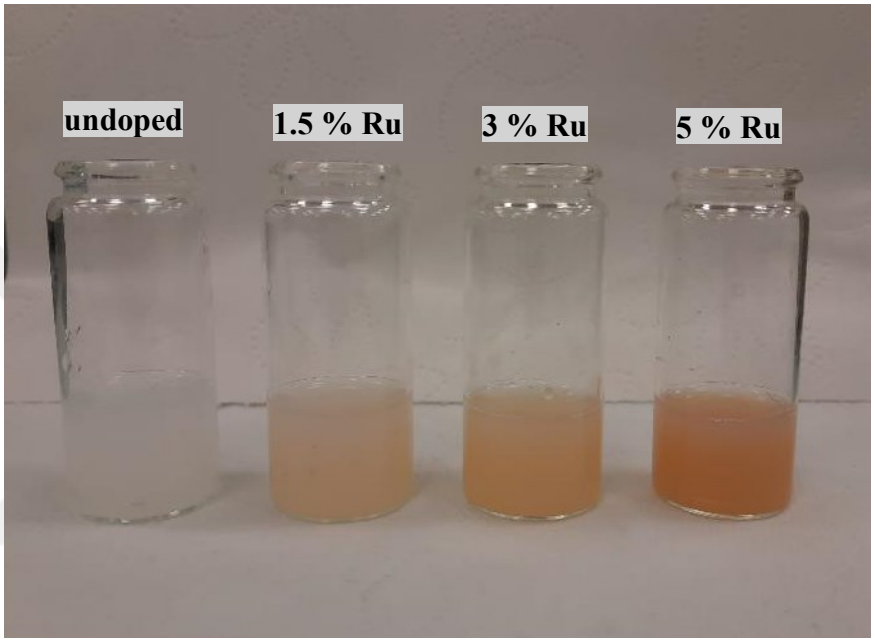

Figure 4.1: Colloidal nanosheet solutions of undoped and Ru-doped 1.5%, 3%, and 5% $KCa_2Nb_3O_{10}$ obtained after exfoliation process.

The resulting nanosheet colloids were restacked by adding 2.5 M aqueous hydrochloric acid to get the nanosheet form of protonated powder. As prepared nanosheet powder was rinsed with distilled water to get rid of residual TBA^+ Cl^- and HCl and dried overnight by freeze-drying.

4.2.3 Preparation of Films

The films were obtained by coating the conductive surfaces of Fluorine doped Tin Oxide coated glass, (FTO with 7 Ω sq^{-1} surface resistivity and ~80% transmittance). Before coating, FTOs were cleaned in isopropyl alcohol for 15 minutes and then in distilled water for 10 minutes in an ultrasonic bath and then dried in an oven at 80 °C. The films were prepared by the electrophoretic deposition technique. 20 mg of sample

powder and 10 mg of Iodine (Sigma-Aldrich, 99.8% ACS reagent) were mixed into 50 mL of acetonitrile in a beaker. The mixture was completely dissolved in ultrasonication for 10 minutes. FTO-coated glass served as the cathode, and a graphite rod was used as the anode. The distance between the two electrodes was approximately 1 cm. A DC power supply (RIGOL DP811) was used to apply a potential of 100 V to the electrodes for 3 minutes, depositing a thin film of the mixture onto the FTO surface on the cathode. After coating, the films were rinsed with deionized water to remove excess iodine and dried using a flow of nitrogen gas.

4.2.4 Characterization of catalysts

The patterns of X-ray diffraction (XRD) were collected using a Bruker D8 Advance X-Ray Diffractometer X-ray powder diffractometer in the range of 2-90◦ with Cu Kα (λ=0.154 nm) as radiation source.

The FESEM images were taken by a Zeiss Ultra Plus field emission scanning electron microscope to determine sample morphologies and particle sizes. The magnification ratio was 20000 and 100000. Secondary electron and In-lens detectors were used for imaging. 5.00 kV accelerating voltage and working distances between 5.4 to 5.8 mm were preferred under ultra-vacuum.

The chemical bonding characteristics of the compositions on the surface of catalysts was tested by a Thermo K-Alpha) with Al Kα source X-ray photoelectron spectroscopy (XPS). Avantage v5.973 software was used for fitting the raw data. The XPS data acquired was corrected with respect to the binding energy of C1s (284.6 eV) as calibration peak for any shift because of charging.

The ultraviolet-visible diffuse reflection absorption spectra (UV–vis) were collected by an UV–vis spectrophotometer (Shimadzu UV-3600 UV-VIS-NIR Spectrophotometer) with an integrated sphere. $BaSO_4$ was used as a reference for films. The data obtained from the UV-Vis analysis were taken as a function of the wavelength of the light reflected from the sample (reflectance mode), then Tauc plots were obtained using the Kubelka-Munk function. The band gap energies of the samples were also obtained from the Kubelka–Munk function (αhν) vs. (hν) plot (Tauc plot).

4.2.5 Photoelectrochemical Characterization

Photoelectrochemical measurements were performed in a standard three-electrode electrochemical cell using the working electrode (sample coated on FTO glass, 1 × 2.5 cm; 2 mm slides) platinum wire as counter electrode, and standard calomel electrode as reference. All photoelectrochemical measurements were performed by Princeton Applied Research VersaSTAT MC workstation. A 300 W Xenon lamb (Newport, 66901) was used as the light source.

LSV studies were performed to examine the CO_2 photoreduction activity of the films of powders in an 0.1 M $KHCO_3$ aqueous solution under the illumination with 300 W Xe lamp. The LSV studies were performed in Ar and CO_2 saturated electrolyte. The electrolyte was bubbled with Ar or CO_2 for 30 min before starting the measurement.

4.2.6 Photocatalytic Characterization

The photocatalytic CO_2 reduction experiments were carried out in a 25 mL quartz vial. 300 W Xe lamp as light source. 10 mg of the photocatalyst powder was completely dissolved in 15 ml of deionized water in an ultrasonic bath for 20 minutes. The system was saturated with a CO_2 for 30 minutes before starting the experiment. The exit port of the cell was connected to a gas chromatography (Agilent 7820A with Poraplot column and TCD detector, He as a carrier gas or Agilent MicroGC with MS-5A and PoraplotU column with micro TCD detector; He carrier gas for MS-5A and Ar carrier as for PoraplotU). The gas detection system was a continuous system. CO_2 was continuously bubbled into the electrolyte and unreacted CO_2 and gas products if any were collected from the exit port of the cell. The gas was sampled every 30 min to detect any gaseous products in the gas line. The picture of the experimental setup was given in Figure 4.2. Liquid products after the photocatalytic reactions were analyzed with 1H NMR.

The photocatalytic CO_2 reduction experiments were performed in a 25 mL quartz vial and using 150 W Xe lamp as light source. 10 mg of the photocatalyst was fully dissolved in 15 ml of water by ultrasonic bath for 15 minutes. Only water used as a medium without any hole scavenger or co catalyst. The closed system for the cell was established by connecting it to GC with a mass flow controller that provided CO_2 on one side and a water trap connection on the other. The system was saturated with CO_2 for 30 minutes prior to the start of the experiment. Throughout the experiment, the GC was

monitored hourly by direct flow of possible gaseous products. After the six-hour experiment, the solution was analyzed by NMR to detect any liquid products.

The photocatalytic HER experiments were conducted in a 5 ml quartz cell using a 300 W Xe lamp as the light source. 10 mg of the photocatalyst powder was fully dissolved in 5ml of 10 vol% methanol aqueous solution in an ultrasonic bath for 15 minutes. 2 rubber septa were used to obtain a completely closed system. First, the vial was closed hermetically with the rubber septa. Then the second one was closed on top of the other in reverse. The system was purged by Argon with a needle to remove dissolved O_2 for 30 minutes before the experiment. Then Argon flow continued between the two septa throughout the experiment to prevent any gas leaking. All experiments were performed for 6 hours.

The liquid products of photocatalytic CO_2 reduction were qualitatively and quantitatively analyzsed with an NMR spectrometer. All ^1H nuclear magnetic resonance spectrometer (NMR) data acquisition process was completed using 500 MHz Bruker Ascend magnet equipped with Avance NEO console and BBO double resonance room temperature probe in D_2O+H_2O. The spectra were analyzed with the ChemEx software and the concentration of liquid products were calculated based on the concentration and peak height of the Sodium trimethylsilylpropanesulfonate (DSS) reference chemical.

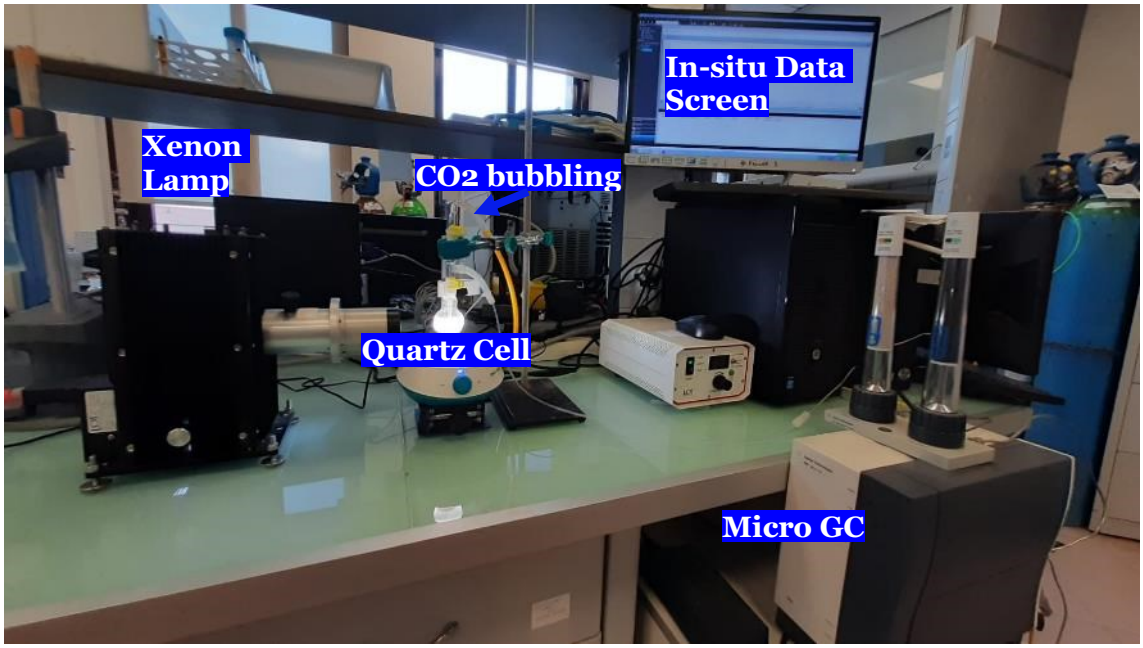

Figure 4.2: Photocatalytic setup utilized for CO_2 reduction.

4.3 Results and Discussion

4.3.1 X-Ray Diffraction

Undoped and doped $KCa_2Nb_3O_{10}$ structures were successfully synthesized, and proton exchanged according to the literature [129], [178], [179]. XRD patterns of the orthorhombic phase of undoped, 1.5%, 3% and 5% Ru-doped $KCa_2Nb_3O_{10}$ and its protonated structures (HCNO) are shown in Figure . Accordingly, XRD analyzes of KNCO and proton exchanged $HCa_2Nb_3O_{10}$ phase were found to be compatible with the literature[180], [181]. There is no significant change in the crystal structure of the material after the proton exchange [178]. All the diffraction peaks can be precisely indexed as $KCa_2Nb_3O_{10}$ (JCPDS, No. 04-013-2545). This indicates the successful synthesis of a highly crystalline structure. In addition, no impurity peak related to any Ruthenium compound was observed.

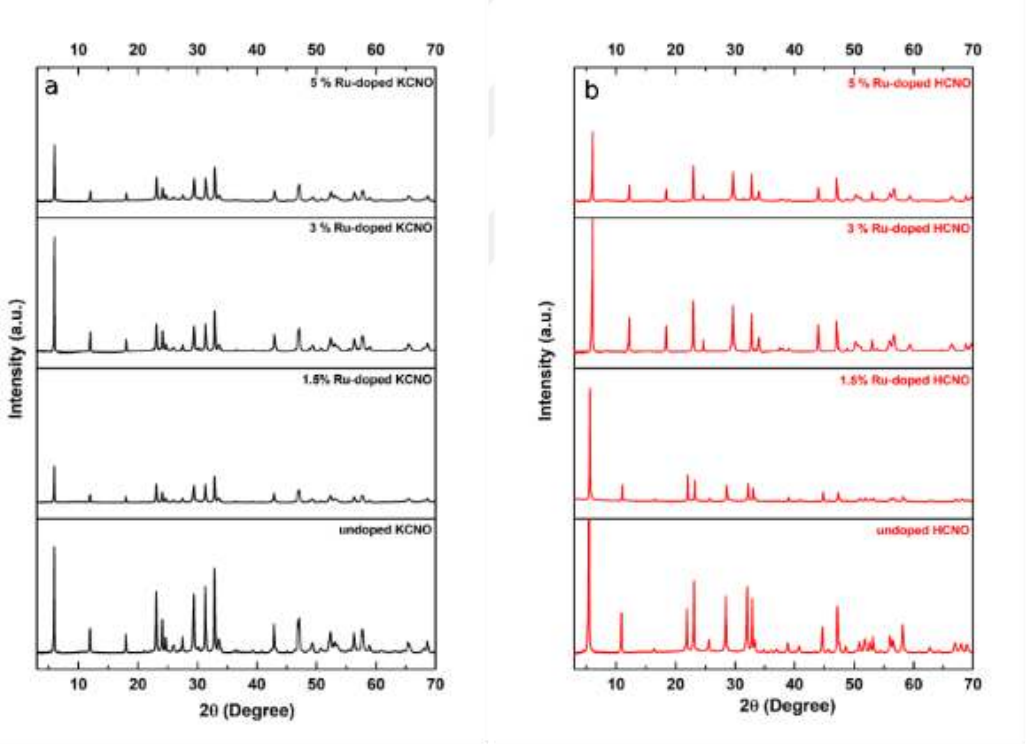

Figure 4.3: XRD patterns of the as-obtained undoped, 1.5%, 3% and 5% Ru-doped $KCa_2Nb_3O_{10}$ and $HCa_2Nb_3O_{10}$ phases after proton exchange.

4.3.2 Morphology of Samples

The morphology of undoped and Ruthenium doped structures prepared by solid state methods was investigated with FESEM as given in Figure . The FESEM images of the the protonated form of the layered structure and restacked exfoliated nanosheets are

also given in the figre. As can be seen, both the parent KCNO and protonated HCNO consisted of agglomerated plate-like particles. The KCNO crystals are well-crystallized. Similarly, the HCNO samples have the well defined layered structure, which shows that the platelike morphology was not affected by proton exchange process. After an exfoliation process, the colloidal nanosheets were restacked the addition of an acid. H_3O^+ precipitates the colloidal nanosheets as a result of the electrostatic attraction between the hydronium ions and negatively charged 2D nanosheets. The restacked nanosheets form a disordered structure as presented in Figure 4.4 e,f, which results in higher surface are in comparison to the parent and protonated structure.

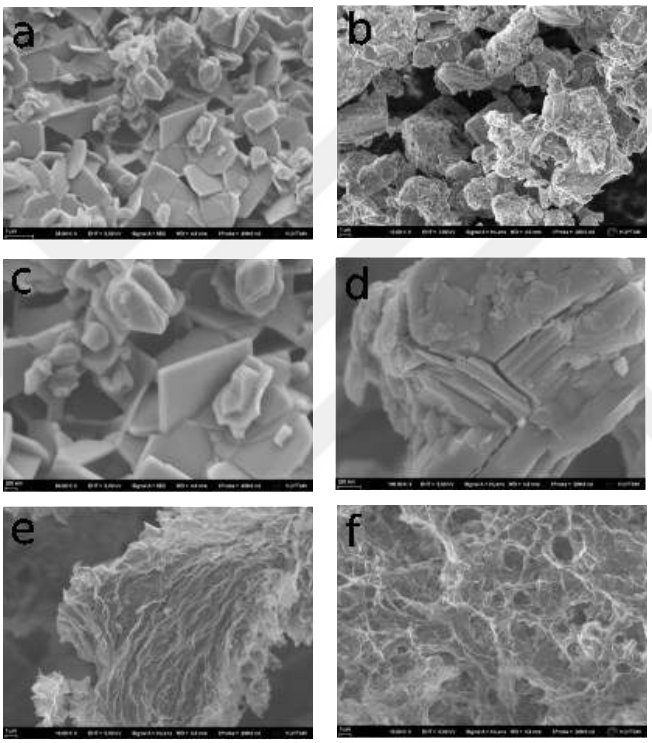

Figure 4.4: SEM images of undoped KCNO (a), 1.5 % Ru-doped KCNO (b) , undoped HCNO (c), 1.5 % Ru-doped HCNO (d), undoped $[CNO]^-$ nanosheets, and (f) 1.5 % Ru-doped $[CNO]^-$ nanosheets.

4.3.3 Absorption Spectra and Band Gap Determination

The undoped KCNO and undoped HCNO samples shows intense UV absorption with an absorption edge located around 350 nm. After doping of ruthenium, the absorption edge is extended to the visible light region with enhanced absorption intensity. As exhibited in Figure 4.5, the absorption curves for Ru-doped samples show a spectral blue shift compared to undoped samples. Moreover, as the ruthenium dope ratio increased, the amount of light absorbed in the visible range also increased. Besides, parent

samples are more effective than proton exchange ones. This may be because the color of the samples is slightly lighter after the proton exchange process. The optical band gaps of the samples were obtained from UV–vis diffuse reflectance spectrum and derived from the Kubelka–Munk conversion. When compares the UV-vis absorption spectra for undoped, 1.5%, 3% and 5% Ru-doped $KCa_2Nb_3O_{10}$ and their protonated version $HCa_2Nb_3O_{10}$ samples. It is observed that the absorption edge is blue shifted after the protonation process for both undoped and Ru-doped samples. Oshima et al. [182] stated that this change in absorbance edges after protonation is due to different interactions between the interlayer cations and the oxygen atoms facing the interlayer space. Ru-doped KCNO have higher absorption in 350-500 nm wavelength range. This can be confirmed by the difference in the colors of the powders. Undoped and 1.5, 3.0 and 5.0% Ru doped powders are shown in the Figure 4.6. The undoped powder is white in color. However, it exhibits a yellow-orange tone due to the ruthenium dopant. Indeed, as the amount of ruthenium ratio in the structure increases, the color becomes darker. which also visually proves that Ru-doped sample absorbs in the visible region.

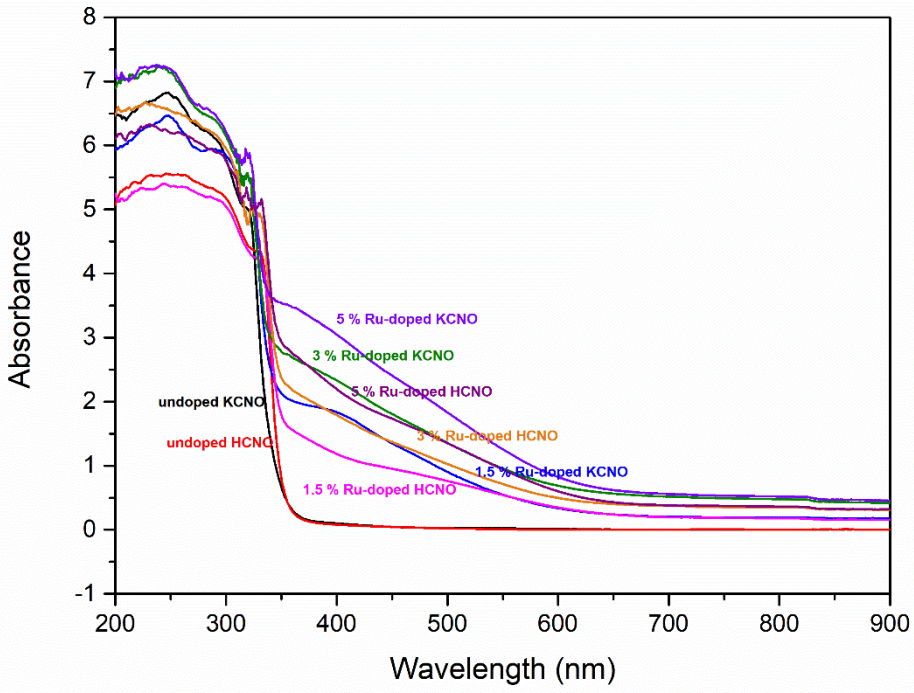

Figure 4.5: UV−Vis diffuse reflectance spectra (DRS) of all undoped and Ru-doped KCNO and HCNO samples.

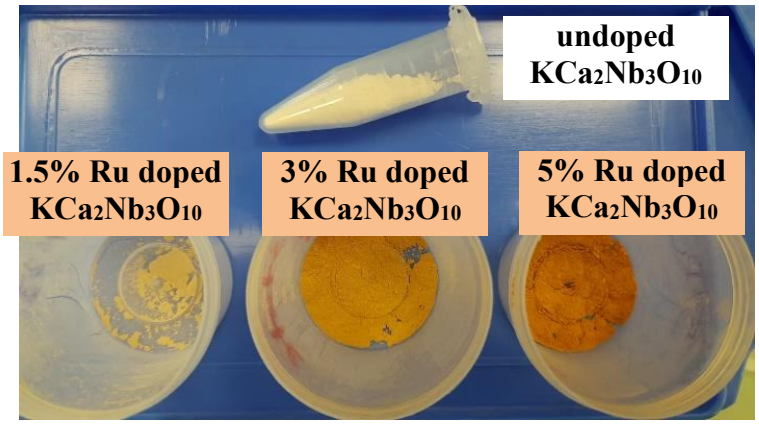

Figure 4.6: The color change of undoped $KCa_2Nb_3O_{10}$ powder with different Ruthenium doping ratios (1.5%, 3% and 5% Ru).

The band gap energies of samples obtained from $(\alpha h\nu)^{1/2}$ versus $(h\nu)$ plots by using the Kubelka–Munk function [183]. The band gaps of undoped KCNO, 1.5% Ru-doped KCNO, 3.0% Ru-doped KCNO, 5.0% Ru-doped KCNO and their protonated versions were estimated from UV-VIS reflection spectra as given in Figure 4.7. These values are 3.57 eV, 3.50 eV, 3.41 eV, 3.38eV, 3.49 eV, 3.42, 3.39 eV, 3.36 eV, respectively. These values are also in given in the chart in Figure 4.8.

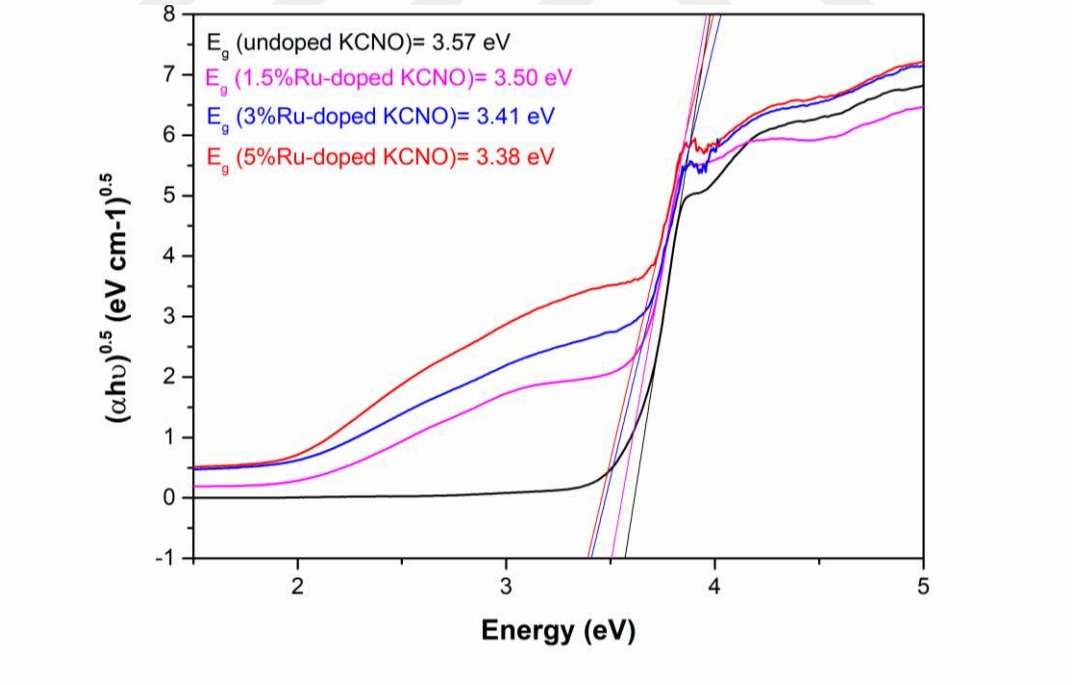

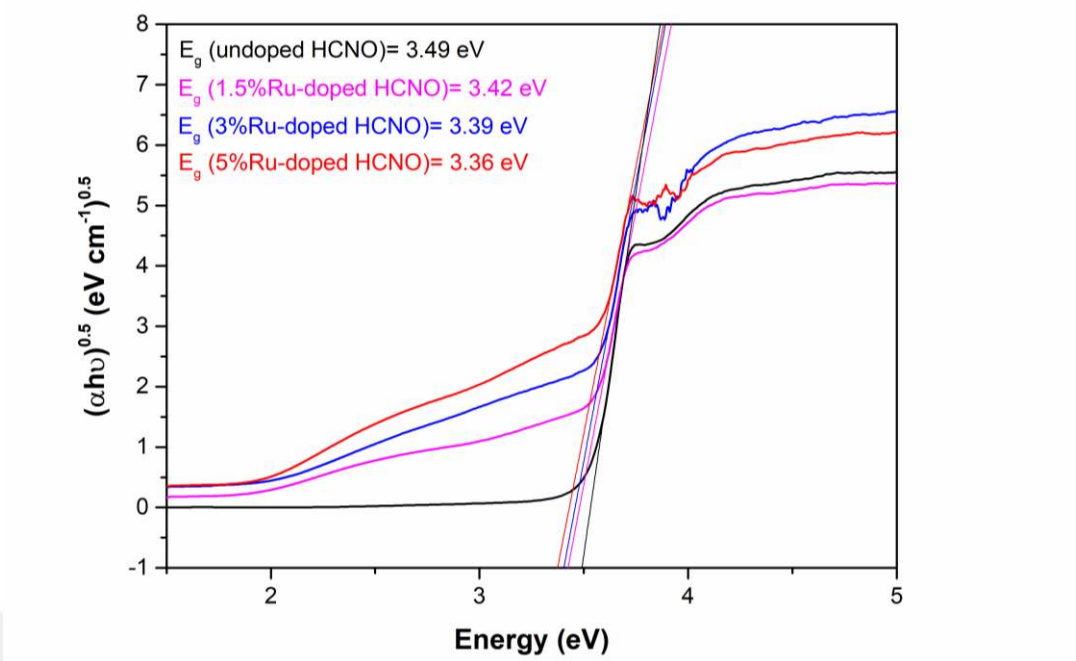

Figure 4.7 Tauc plots of undoped and 1.5 %, 3% and 5% Ru-doped $KCa_2Nb_3O_{10}$ and $HCa_2Nb_3O_{10}$ for estimation of band gap energies.

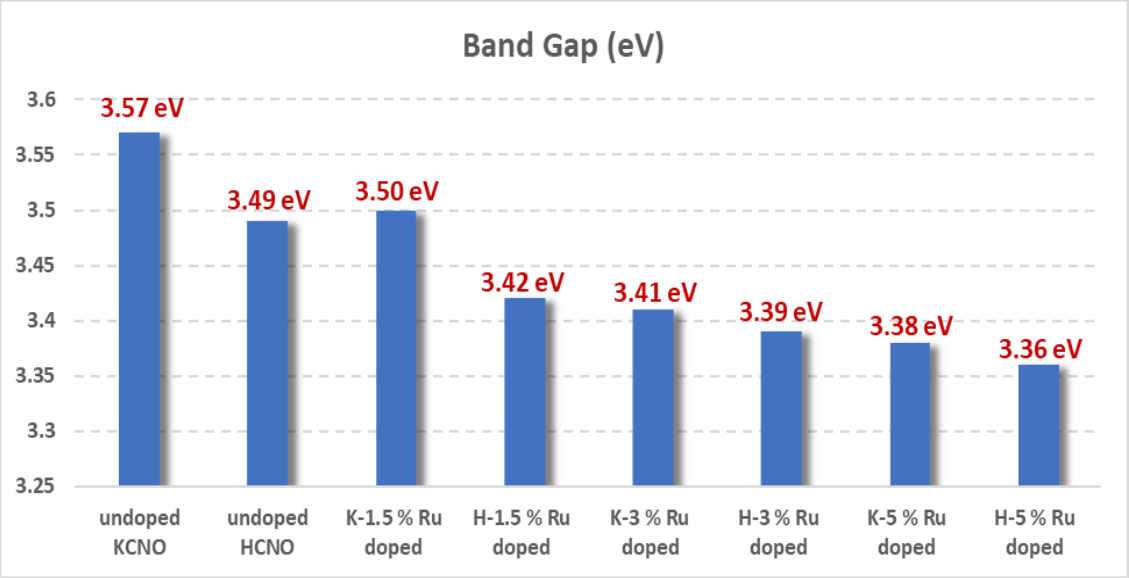

Figure 4.8: Representative image of effect of Ru-doping on band gap energy difference.

In order to determine the energy positions of the bands of the photocatalyst, the valence bands of the samples were determined from XPS valence spectrum given in Figure 4.9. All valence band position data obtained according to the vacuum level were converted according to NHE (2.78 V, 1.77 V, 2.24 V and 1.62 V vs NHE, undoped parent, undoped protonated, Ru-doped parent and Ru-doped protonated respectively). The

location of conduction band was estimated either by the combination of the valence band from the XPS data and optical band gap or by assuming that the conduction band is approximately 0.1-0.4 eV above the flat band potentials [184]–[186].

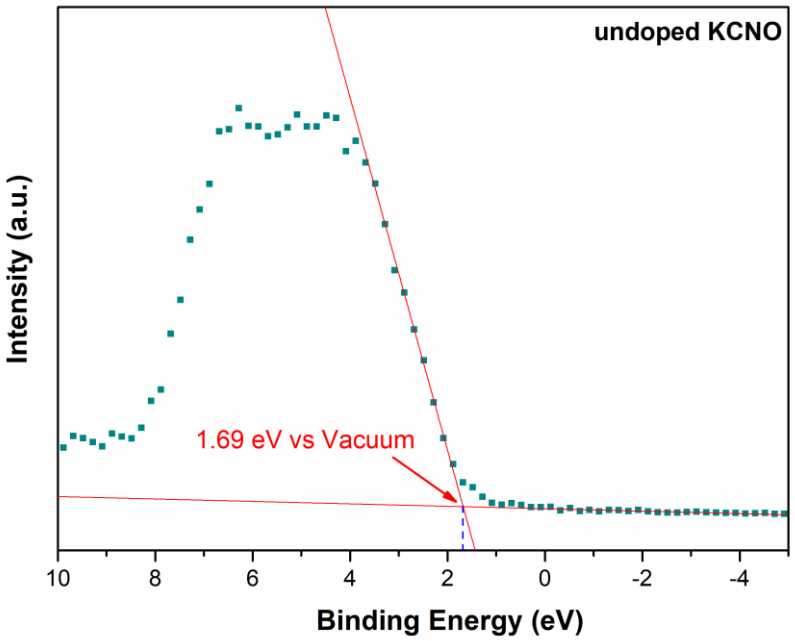

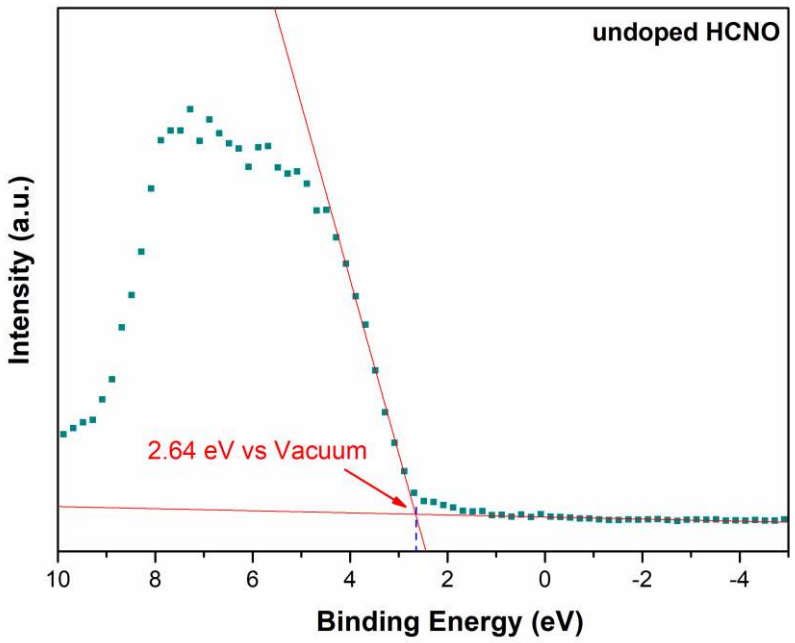

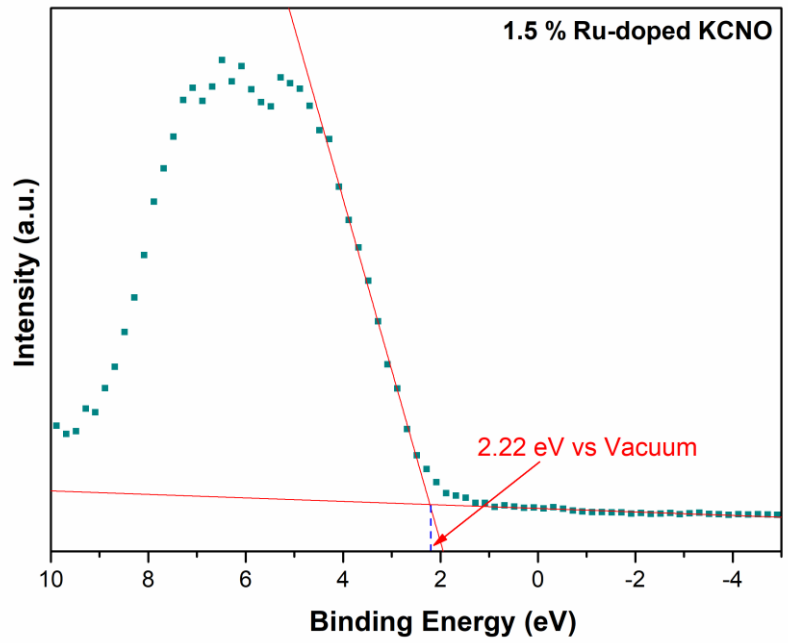
1.5 % Ru-doped KCNO
Intensity (a.u.)
2.22 eV vs Vacuum
10
8
6
4
2
0
-2
-4
Binding Energy (eV)

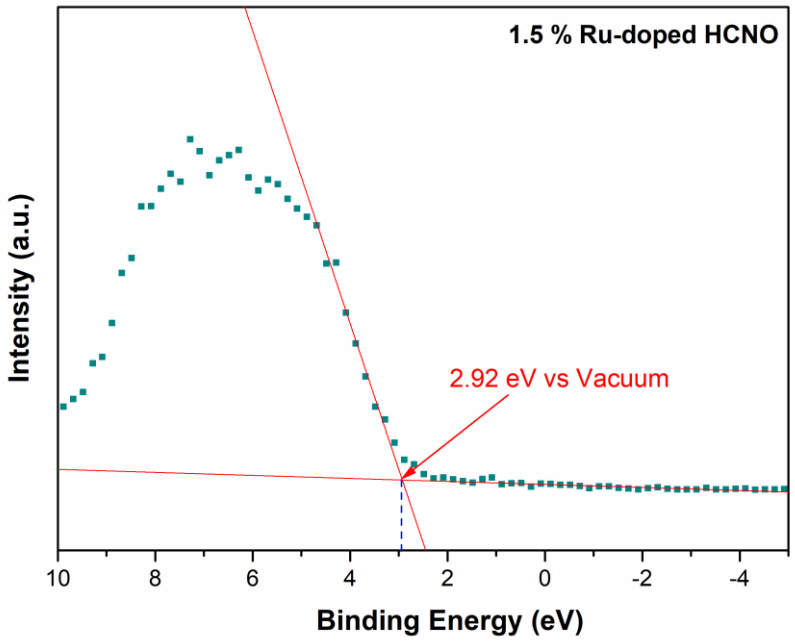
1.5 % Ru-doped HCNO
Intensity (a.u.)
2.92 eV vs Vacuum
10
8
6
4
2
0
-2
-4
Binding Energy (eV)

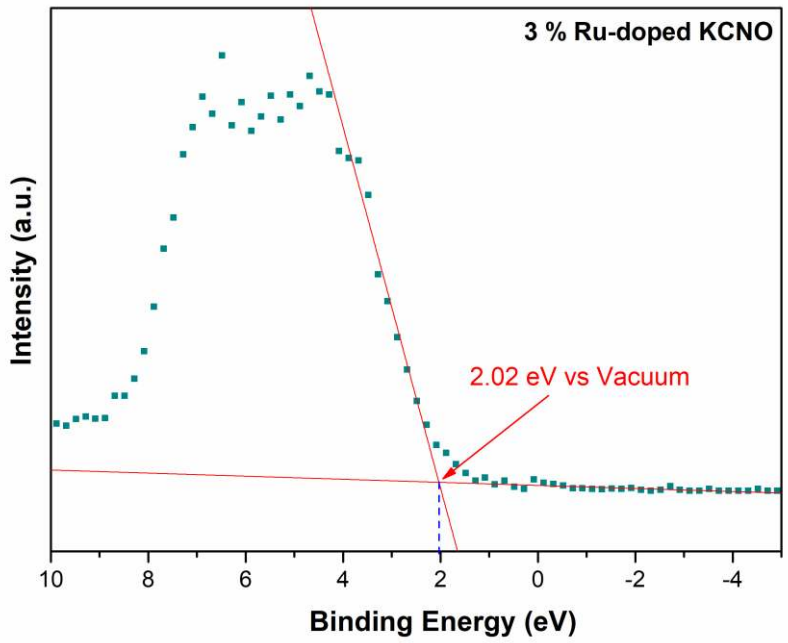
3 % Ru-doped KCNO
Intensity (a.u.)
2.02 eV vs Vacuum
10
8
6
4
2
0
-2
-4
Binding Energy (eV)

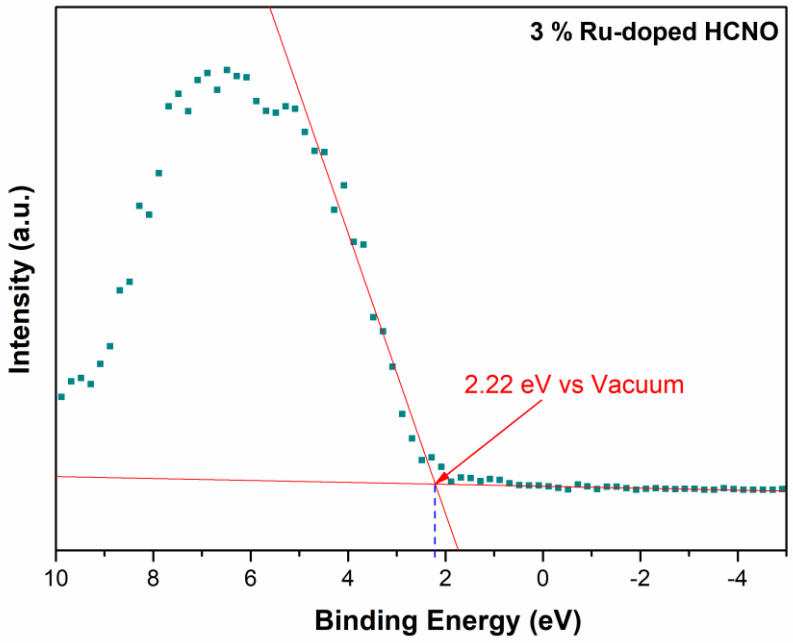
3 % Ru-doped HCNO
Intensity (a.u.)
2.22 eV vs Vacuum
10
8
6
4
2
0
-2
-4
Binding Energy (eV)

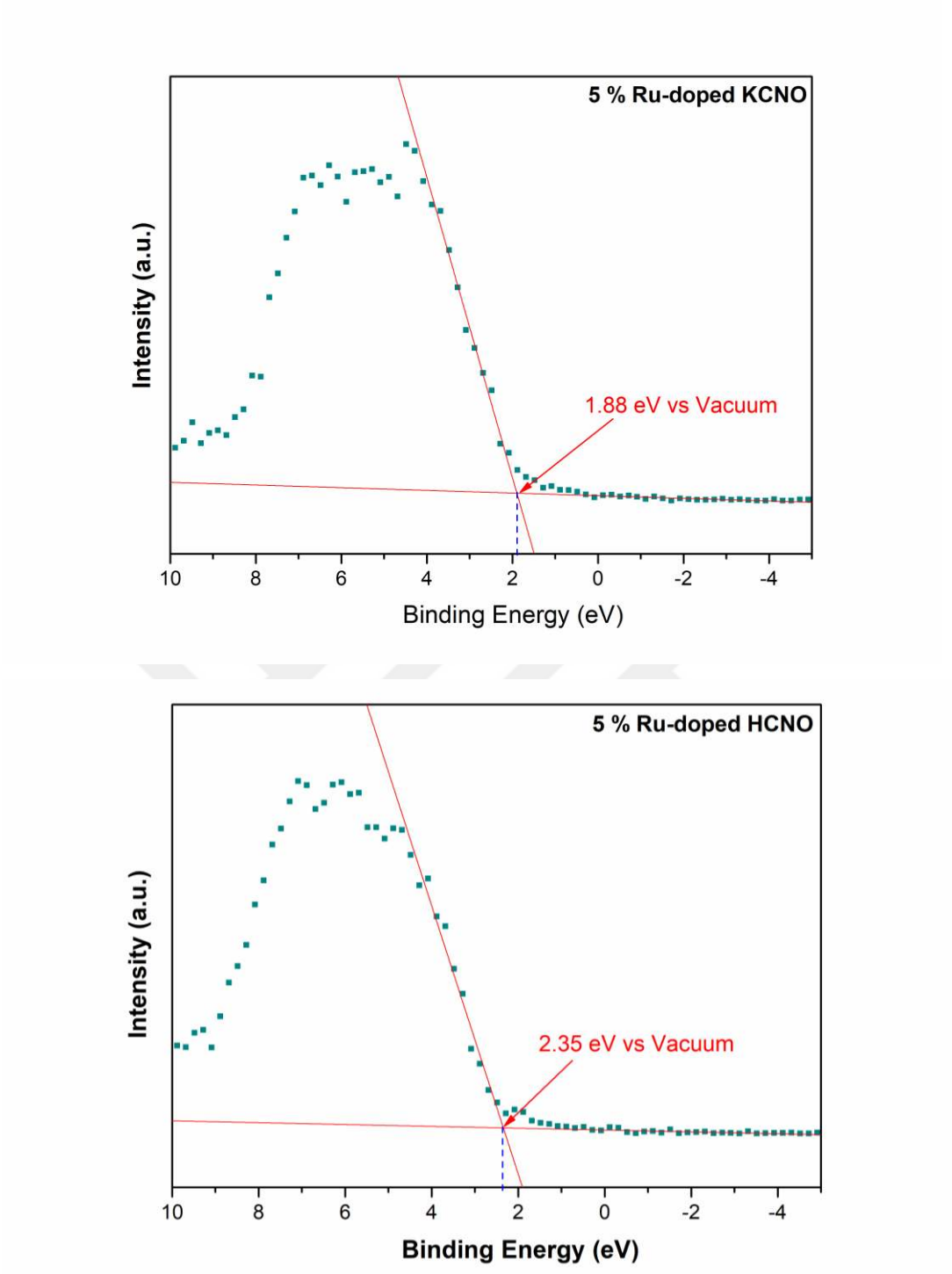

Figure 4.9: XPS spectra of core levels to valence band maximum (VBM) for KCNO and protonated HCNO doped and undoped samples.

Band structures of undoped and Ru-doped parent and protonated samples are given in Figure 4.10 according to these estimations. There is a negative shift in the conduction bands after doping with noble metals compared to undoped samples. In addition, it was seen that the conduction bands shift to more negative potentials and valence bands almost remain identical after the proton exchange reaction.

Figure 4.10: Schematic diagram of undoped and Ru-doped samples estimated band structures from along with Tauc's Plot and XPS Valence Band Spectra Data.

4.3.4 Photoelectrochemical Measurements

All photoelectrochemical (PEC) experiments were carried out in 0.5 M K_2SO_4 using three electrode systems under UV-irradiation. The photo response of all samples was measured using the chronoamperometry technique.

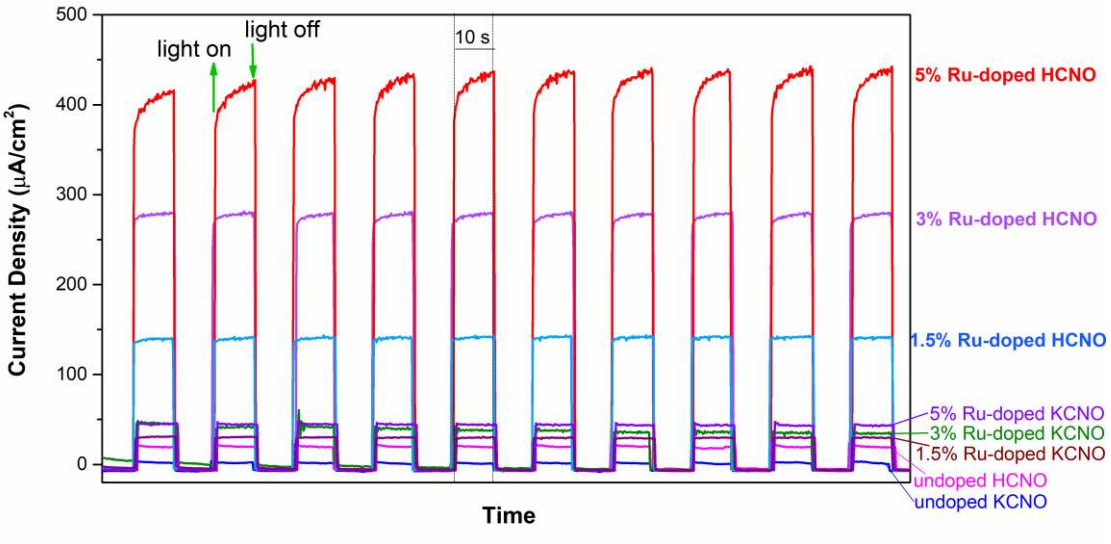

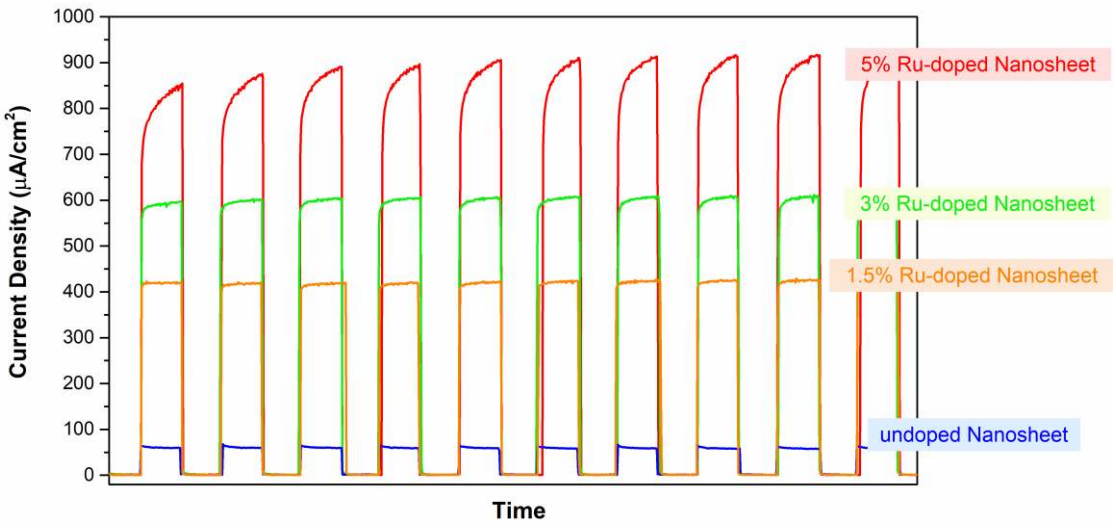

Figure 4.11: Photoelectrochemical performances of all version of the samples were measured by chronoamperometry technique in 0.5 M K_2SO_4 at scan rate 20 mV s^{-1} under the UV irradiation.

To understand the mechanism of the photoinduced charge transfer kinetics as migration and separation rate of photogenerated electrons and holes, transient photocurrent response was carried out. The surface e-hole recombination mechanism is generally interpreted from the photocurrent response of the semiconductor electrodes with chopped illumination [187]. Figure a and b show the kinetics of the photocurrent and the responses to chopping the UV-light for the undoped and Ru-doped $KCa_2Nb_3O_{10}$, $HCa_2Nb_3O_{10}$ exchanged and nanosheet versions. All experiments were performed at 1.2 V (vs. SCE) and with chopped illumination without a hole scavenger. Figure 4.11 b, the transient photocurrent response of single site Ruthenium-doped and undoped nanosheet samples are compared. The current densities of samples are given in Table 2.

Table 2 The current density values from chronoamperometry experiments of all samples

	Undoped	1.5% Ru-doped	3% Ru-doped	5% Ru-doped
KCNO	15 μA/cm^2	30 μA/cm^2	38 μA/cm^2	45 μA/cm^2
HCNO	22 μA/cm^2	138 μA/cm^2	273 μA/cm^2	433 μA/cm^2
$[CNO]^-$ Nanosheet	60 μA/cm^2	410 μA/cm^2	585 μA/cm^2	900 μA/cm^2

When the values were examined, the photocurrent of the Nanosheets showed a significant increase, increasing about 5 times compared to the parent material. Considering the ruthenium-doped material, a significant change was observed compared to the undoped samples. In particular, the photocurrent density of the 5% Ru-doped $[CNO]^-$ nanosheet sample was around 900 μA/cm^2, followed by 3% Ru-doped and 1.5% Ru-doped $[CNO]^-$ nanosheet was 585 μA/cm^2 and 410 μA/cm^2 respectively.

4.3.5 Linear Sweep Voltammetry (LSV)

Linear sweep voltammetry (LSV) technique was used to compare the CO_2 reduction activity of the samples. The LSV measurements were performed using an electrochemical equipped with a standard three-electrode system. The reference electrode and the counter electrode were SCE and platinum wire, respectively. A 300 W Xe arc lamp was taken as the light source. The photocatalytic activities of the electrodes were compared using two solutions: Argon-saturated 0.1 M $KHCO_3$ and CO_2-saturated 0.1 M $KHCO_3$ at 20 mV s^{-1}.

The photoelectrocatalytic performance of CO_2 reduction of samples were examined under both dark and light conditions. The films were prepared by electrophoretic deposition technique were used as a working electrode.

In LSV curve reflects the amount of current flowing through the working electrode at a given potential. A higher cathodic current density value means that a higher amount of current is flowing through the working electrode and more facile charge transfer kinetics. When considering the photocatalytic reduction of CO_2, a negative current density that is more pronounced is typically perceived as an indication of enhanced efficiency in CO_2 reduction. This interpretation stems from the fact that the reduction process involves the transfer of electrons from the working electrode to CO_2 molecules, consequently generating a current flow through the working electrode. Thus, a higher current density implies a greater number of electrons being successfully transferred from the working electrode to CO_2, thereby leading to heightened CO_2 reduction efficiency.
LSV plots of undoped, 1.5 %, 3 % and % 5 Ru-doped Parent, their protonated and nanosheet versions are given in Figure 4.12. These LSV plots show distinct cathodic currents, evidence of the samples' photoelectrochemical reduction.

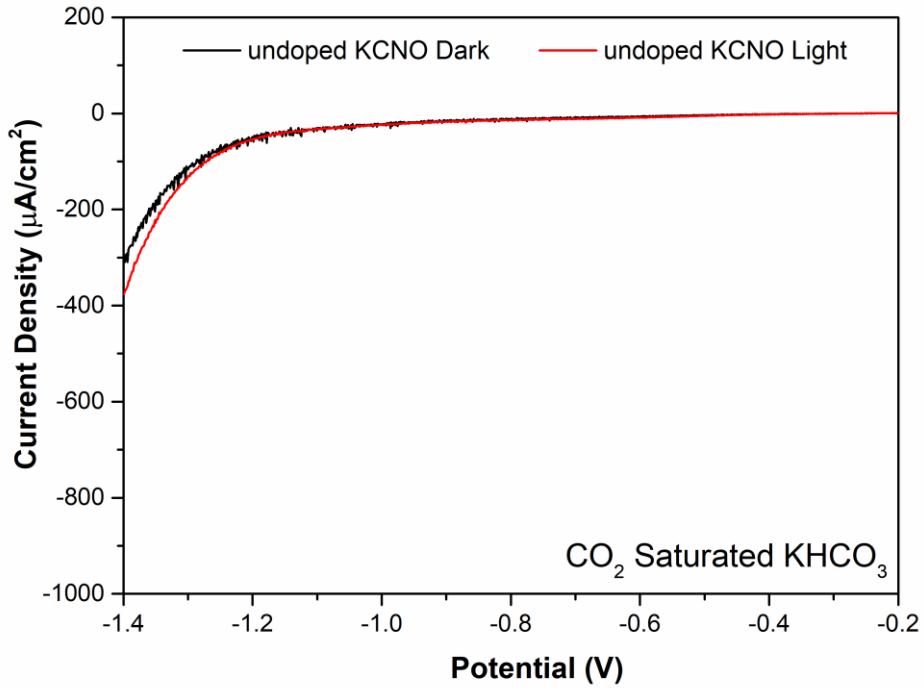
undoped KCNO Dark
undoped KCNO Light
Current Density (μA/cm²)
Potential (V)
CO2 Saturated KHCO3
200
0
-200
-400
-600
-800
-1000
-1.4
-1.2
-1.0
-0.8
-0.6
-0.4
-0.2

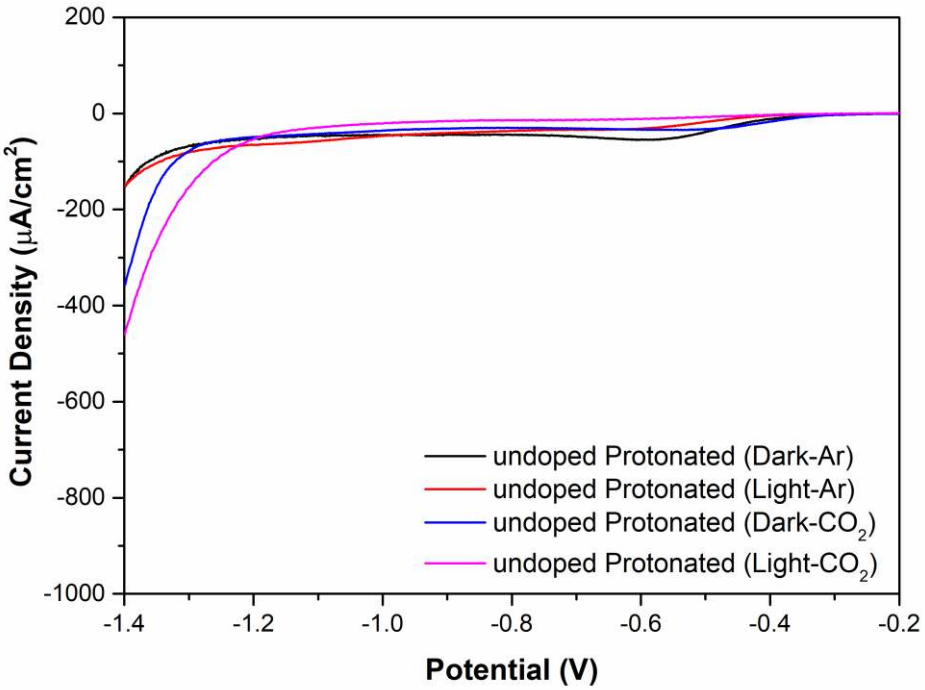
undoped Protonated (Dark-Ar)
undoped Protonated (Light-Ar)
undoped Protonated (Dark-CO2)
undoped Protonated (Light-CO2)
Current Density (μA/cm²)
Potential (V)
200
0
-200
-400
-600
-800
-1000
-1.4
-1.2
-1.0
-0.8
-0.6
-0.4
-0.2

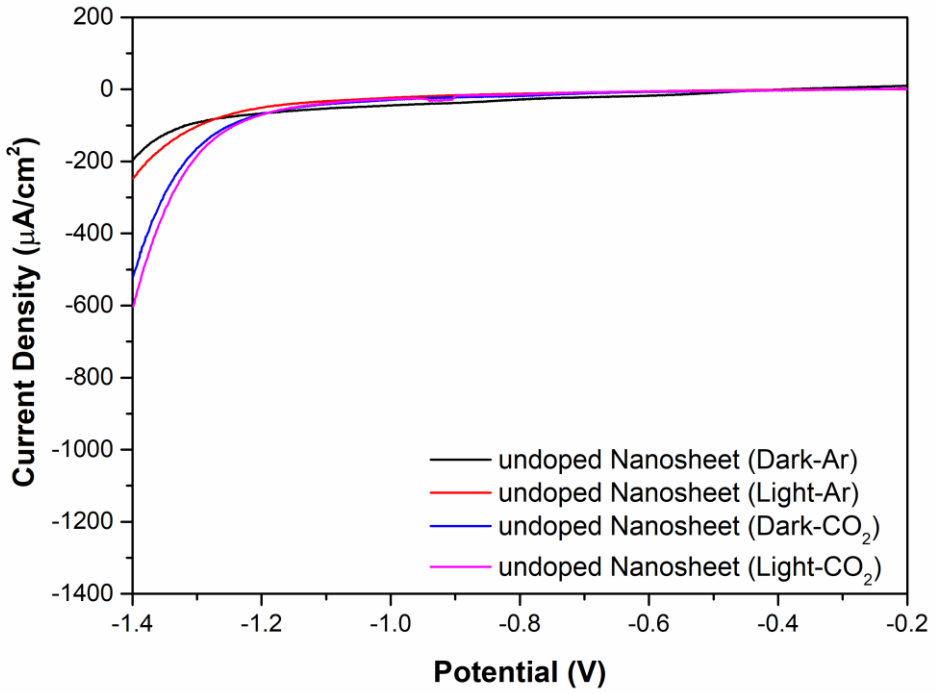
Current Density (μA/cm²)
Potential (V)
undoped Nanosheet (Dark-Ar)
undoped Nanosheet (Light-Ar)
undoped Nanosheet (Dark-CO2)
undoped Nanosheet (Light-CO2)

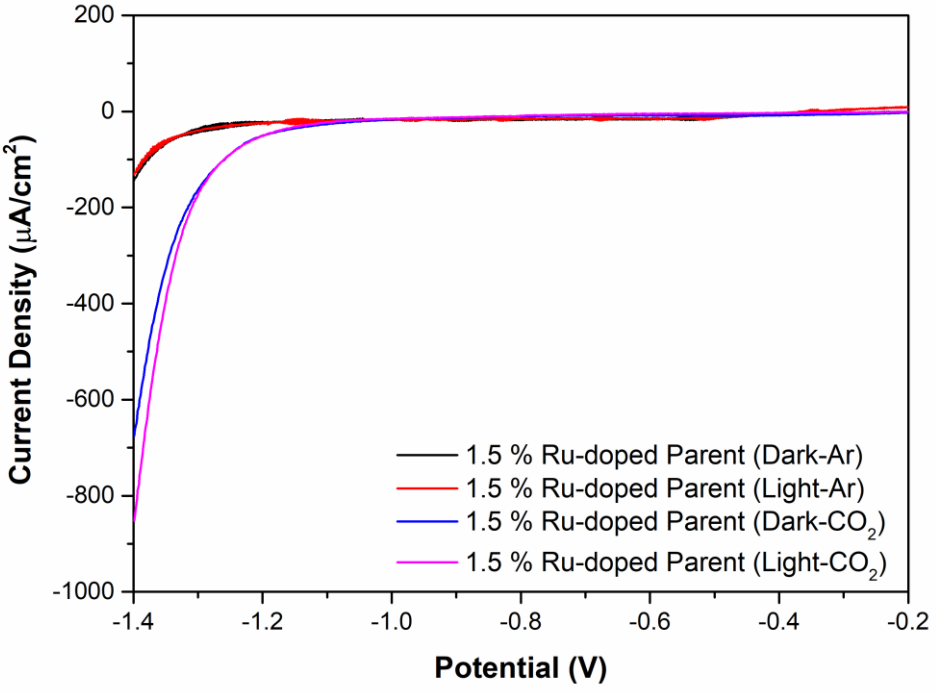
Current Density (μA/cm²)
Potential (V)
1.5 % Ru-doped Parent (Dark-Ar)
1.5 % Ru-doped Parent (Light-Ar)
1.5 % Ru-doped Parent (Dark-CO2)
1.5 % Ru-doped Parent (Light-CO2)

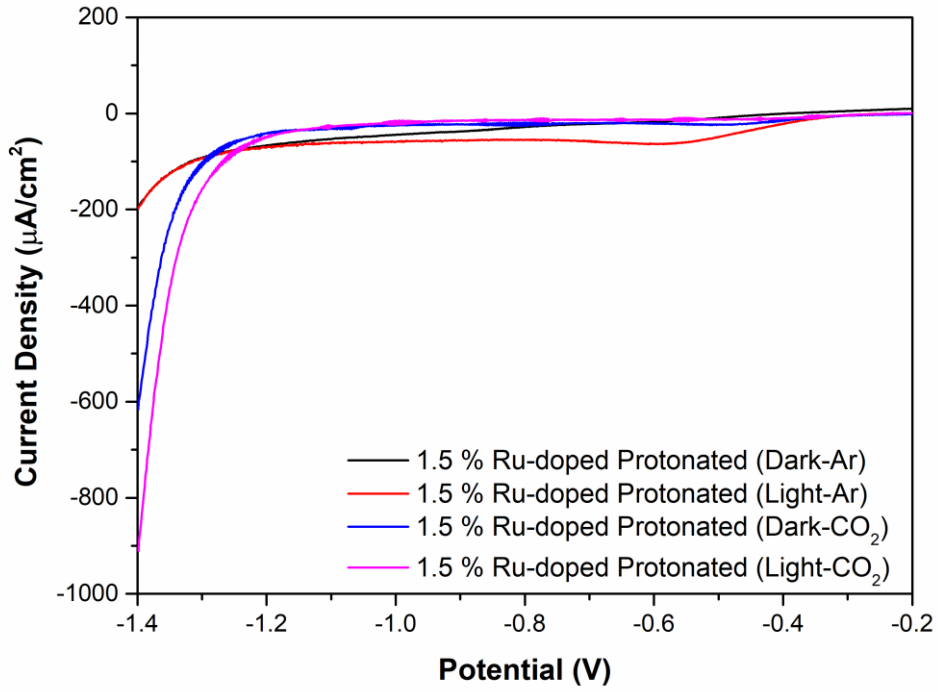
Current Density (μA/cm²)
Potential (V)
200
0
-200
-400
-600
-800
-1000
-1.4
-1.2
-1.0
-0.8
-0.6
-0.4
-0.2
1.5 % Ru-doped Protonated (Dark-Ar)
1.5 % Ru-doped Protonated (Light-Ar)
1.5 % Ru-doped Protonated (Dark-CO2)
1.5 % Ru-doped Protonated (Light-CO2)

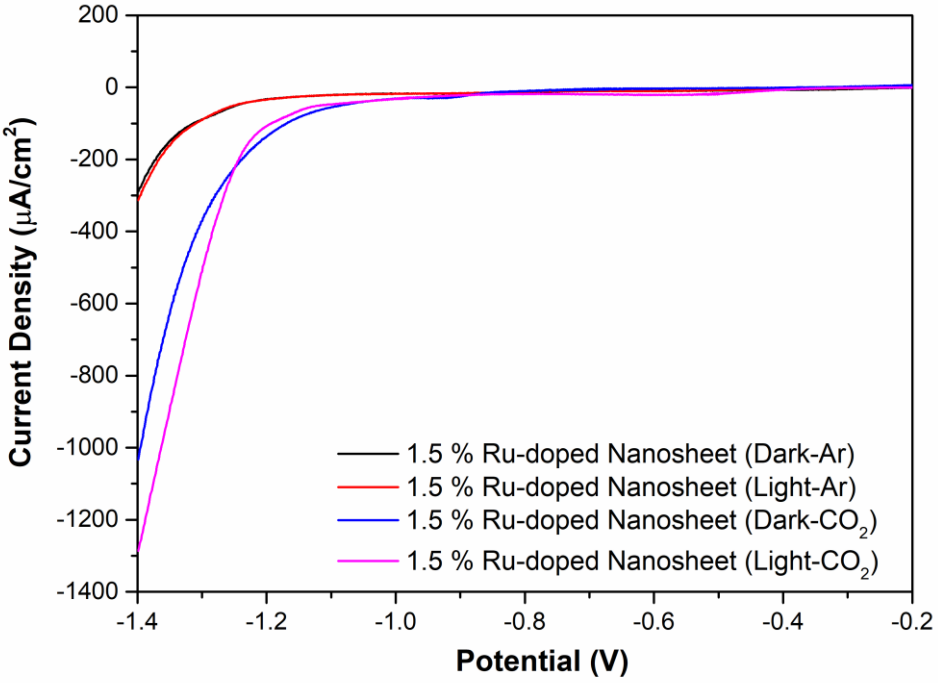
Current Density (μA/cm²)
Potential (V)
200
0
-200
-400
-600
-800
-1000
-1200
-1400
-1.4
-1.2
-1.0
-0.8
-0.6
-0.4
-0.2
1.5 % Ru-doped Nanosheet (Dark-Ar)
1.5 % Ru-doped Nanosheet (Light-Ar)
1.5 % Ru-doped Nanosheet (Dark-CO2)
1.5 % Ru-doped Nanosheet (Light-CO2)

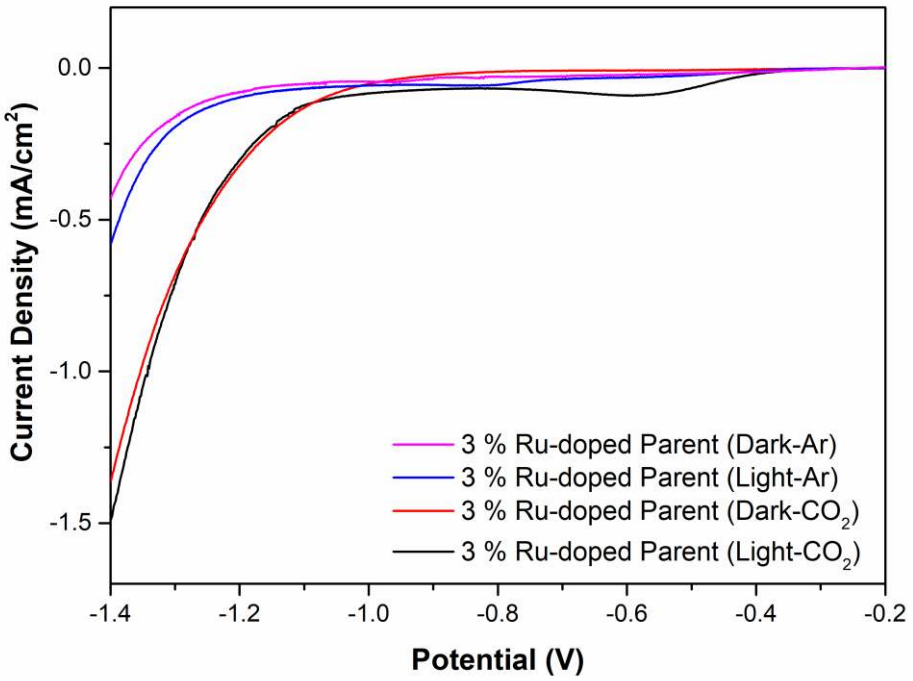
0.0
-0.5
-1.0
-1.5
Current Density (mA/cm^2)
-1.4
-1.2
-1.0
-0.8
-0.6
-0.4
-0.2
Potential (V)
3 % Ru-doped Parent (Dark-Ar)
3 % Ru-doped Parent (Light-Ar)
3 % Ru-doped Parent (Dark-CO_2)
3 % Ru-doped Parent (Light-CO_2)

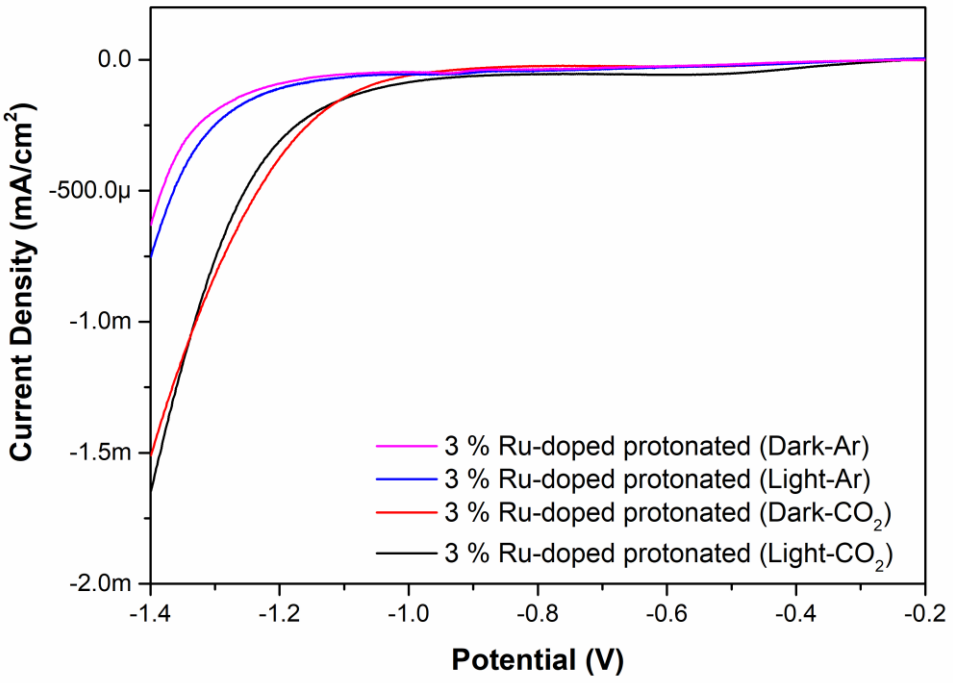
0.0
-500.0µ
-1.0m
-1.5m
-2.0m
Current Density (mA/cm^2)
-1.4
-1.2
-1.0
-0.8
-0.6
-0.4
-0.2
Potential (V)
3 % Ru-doped protonated (Dark-Ar)
3 % Ru-doped protonated (Light-Ar)
3 % Ru-doped protonated (Dark-CO_2)
3 % Ru-doped protonated (Light-CO_2)

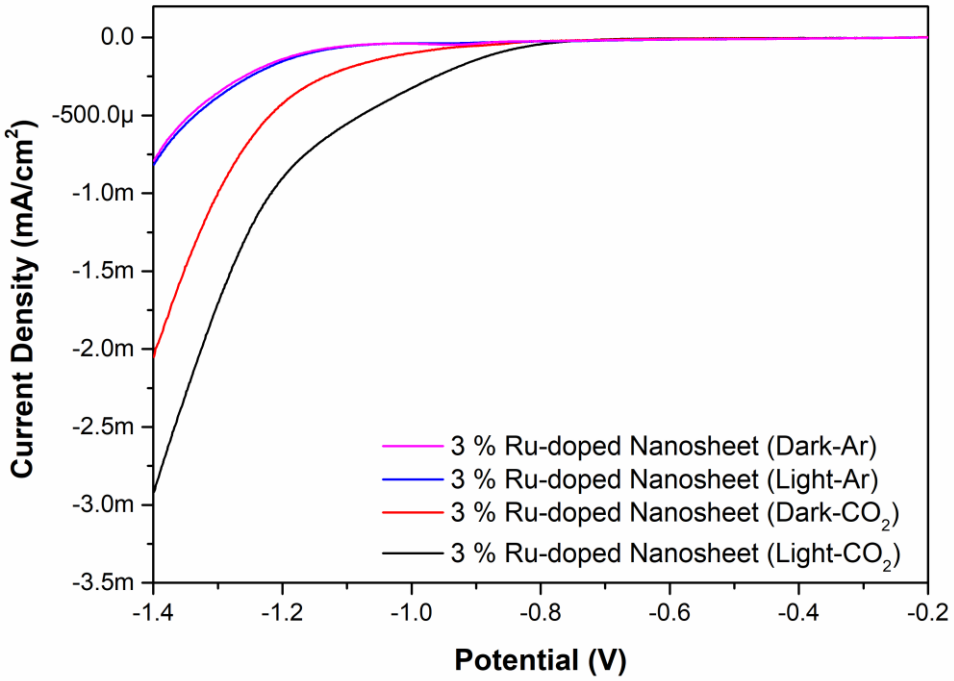
0.0
-500.0µ
-1.0m
-1.5m
-2.0m
-2.5m
-3.0m
-3.5m
Current Density (mA/cm²)
-1.4
-1.2
-1.0
-0.8
-0.6
-0.4
-0.2
Potential (V)
3 % Ru-doped Nanosheet (Dark-Ar)
3 % Ru-doped Nanosheet (Light-Ar)
3 % Ru-doped Nanosheet (Dark-CO2)
3 % Ru-doped Nanosheet (Light-CO2)

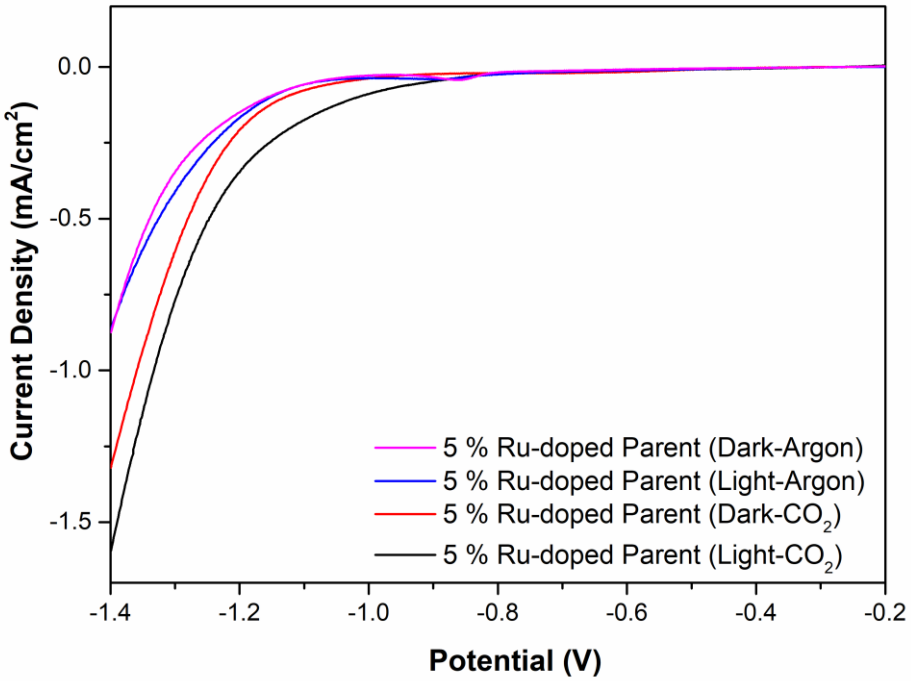
0.0
-0.5
-1.0
-1.5
Current Density (mA/cm²)
-1.4
-1.2
-1.0
-0.8
-0.6
-0.4
-0.2
Potential (V)
5 % Ru-doped Parent (Dark-Argon)
5 % Ru-doped Parent (Light-Argon)
5 % Ru-doped Parent (Dark-CO2)
5 % Ru-doped Parent (Light-CO2)

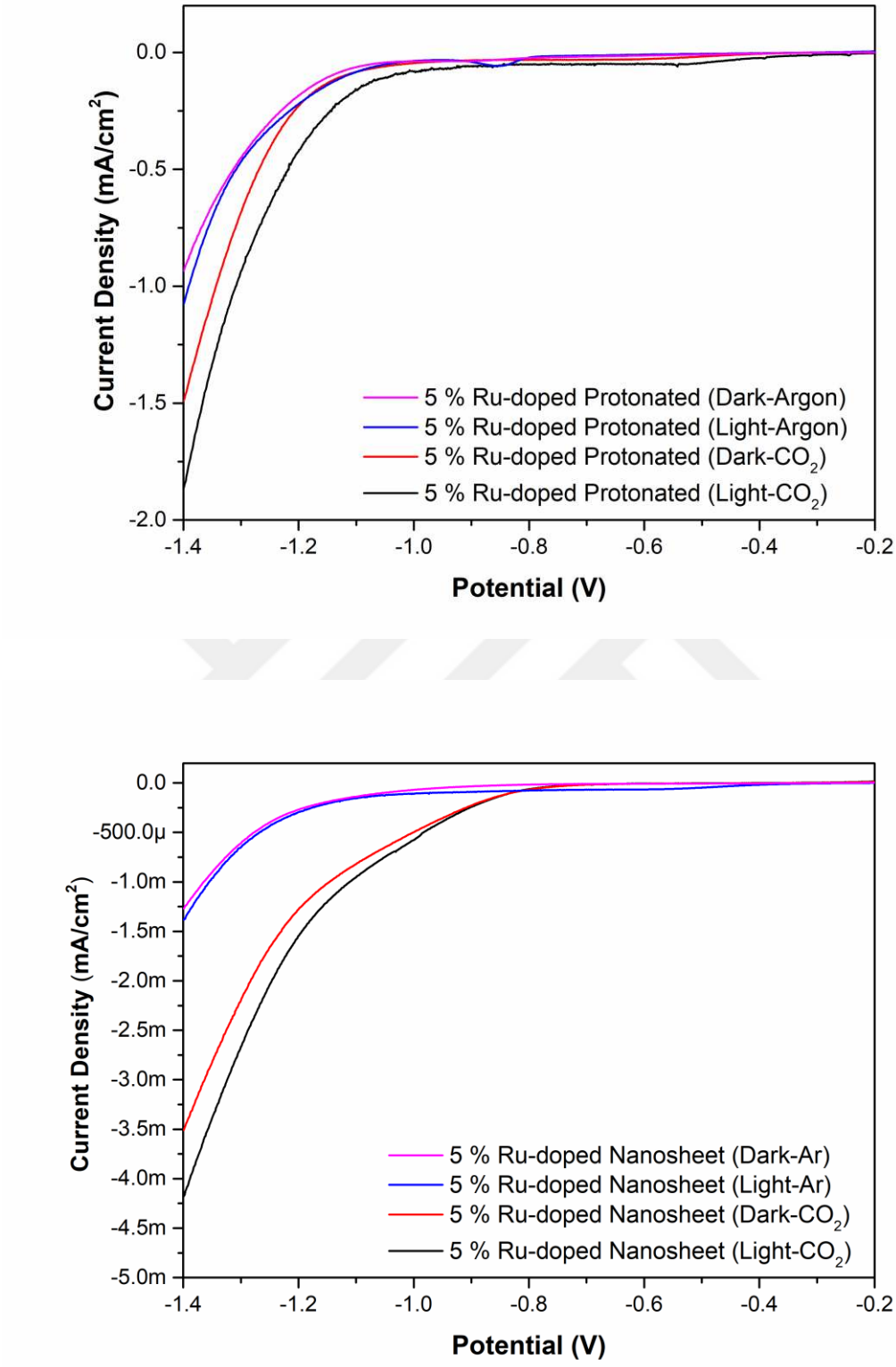

Figure 4.12: Linear Sweep Voltammetry (LSV) plot of undoped, 1.5 %, 3.0 % and % 5.0 Ru-doped KCNO, HCNO and $[CNO]^-$ nanosheet versions in 0.1 M $KHCO_3$ electrolyte. Experiments were carried out separately in solution saturated with Argon and CO_2 under

illumination and dark conditions. Potential sweep rate 20 mV/s.

The cathodic current obtained from the samples in the saturated solution with CO_2 is higher than the Argon saturated solution. Obviously, all versions of undoped KCNO samples exhibited the lowest current density in presence and absence of CO_2.
Notably, the nanosheet sample doped with 5% Ruthenium exhibited a significant augmentation in photocurrent when compared to the other samples. This remarkable enhancement can be attributed to the presence of Ruthenium, which effectively decreases the reflectance of incident light, thereby enabling more efficient photon capture. Additionally, Ruthenium doping also contributes to the reduction in transport distances, leading to enhanced separation of photogenerated electrons and holes.

After loading of Ruthenium into $KCa_2Nb_3O_{10}$ structure, cathodic final potentials go more negative. Due to its lower Fermi energy level, it possesses the ability to extract photogenerated electrons from the powder and facilitate the separation of electron-hole pairs [188] . Their current densities increase evidently when the bias potential was over -0.8 V, reflecting a good coupling of the photoelectrocatalytic reduction of CO_2 (Figure 4.13).

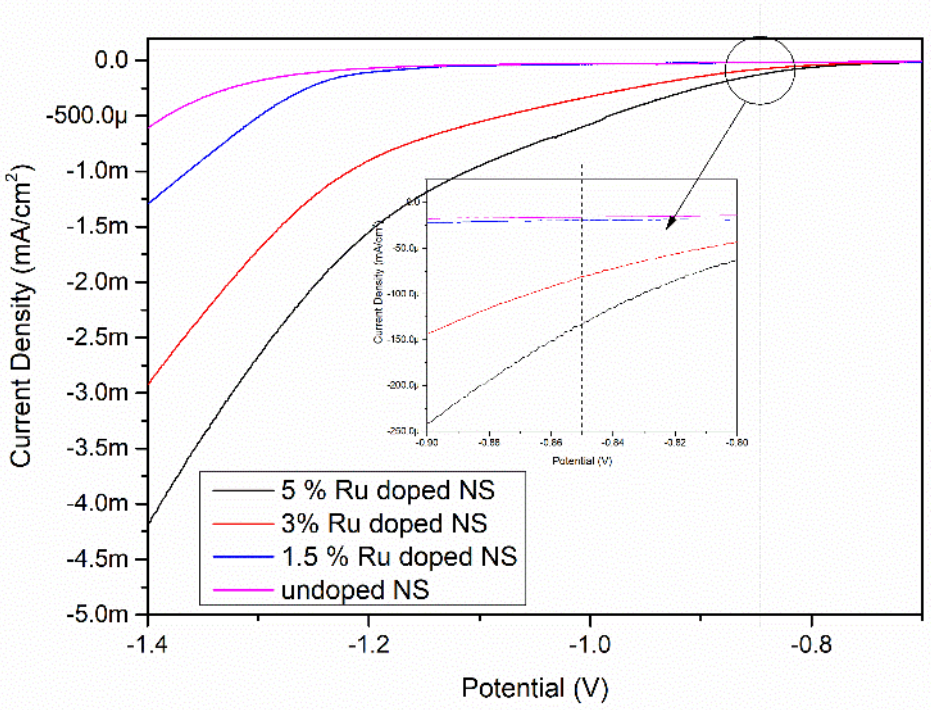

Figure 4.13: The cathodic current densities at over -0.8 V of Linear Sweep Voltammetry (LSV) plot of 1.5 %, 3.0 % and % 5.0 Ru-doped [CNO]- nanosheet sample.

Nevertheless, it is crucial to acknowledge that a more negative current density does not invariably correlate with a greater overall efficiency of CO_2 reduction. The efficiency of CO_2 reduction depends on a number of factors, including the type of photocatalyst used, the reaction conditions, and the specific products being produced. Consequently, for a comprehensive understanding of CO_2 reduction efficiency within a given experiment, it becomes imperative to conduct a thorough analysis of the LSV data. This analysis should include an examination of both potential and current density values, in addition to an evaluation of the resulting products obtained.

LSV results supports the higher photocurrent of all nanosheet samples compared to their parent and protonated versions at different voltages applied. The cathodic current density of undoped, 1.5 %, 3% and 5% Ru doped Nanosheet samples in CO_2-saturated electrolyte under light are 600 $\mu A/cm^2$, 1.30 mA/cm^2, 2.93 mA/cm^2, 4.10 mA/cm^2, respectively.

Comparing the electrocatalytic activity of different ratio Ruthenium doped, it can be observed that higher cathodic current density can be achieved with 5 % Ru-doped nanosheet sample. Ruthenium increased the photocatalytic activity by providing an extra active site [189] for CO_2 reduction reactions. Among all samples, specifically the nanosheet of 5% Ru-doped sample, drastically increased the cathodic current (~4.10 mA). In these nanosheets, which have a large surface area, the number of active sites is much higher. Both results from the transient photocurrent response and LSV provide evidence for improved the promoted separation efficiency of photogenerated charges for 5 % Ru as compared to other samples. This enhanced separation efficiency can be attributed to their superior photocatalytic performance.

4.3.6 Photocatalytic CO_2 Reduction

Various approaches, such as catalytic, photocatalytic, electrocatalytic, and photoelectrocatalytic processes, have been extensively investigated for the conversion of CO_2 into hydrocarbon fuels. Each approach requires efficient catalysts input to activate the thermodynamically stable linear CO_2 molecule, which exhibits high carbon oxidation states. Among these potential approaches, the photoconversion of CO_2 with water using heterogeneous photocatalysts stands out as a sustainable solution. This approach, often referred to as artificial photosynthesis, emulates natural photosynthesis and offers a

means to produce solar fuels and high-value chemicals (e.g., CO, formic acid, ethanol, and methanol) in an environmentally friendly manner.

The NMR study was conducted using a MHz Bruker Ascend magnet equipped with an Avance NEO console and a BBO double resonance room temperature probe. To avoid the water peak dominating over other molecules, water suppression experiments were used instead of routine 1D proton pulse [190]. In this study, we used 1D NOESY-presat (noesygppr1d) pulse program for all NMR data acquisitions, and each spectrum consisted of 8K scans of 32K complex data points with a spectral width of 9615.4 Hz.

To prepare the NMR samples, the powder-solvent mixture was centrifuged at 3000 rpm for 15 minutes following a 6-hour photocatalytic experiment. A liquid sample was then taken from the resulting solution, which was free of any powder particles. 495 µl of each NMR samples were mixed with 55 µl of 10% deuterium oxide (D_2O), containing 1 mM 3-trimethylsilyl-1-propanesulfonate, sodium salt (DSS) [191], and loaded into a standard 5 mm NMR tube. Chenomx is a software tool designed to determine the concentration and peak shape of various molecules within its library. This determination is made by analyzing the concentration and peak height of the DSS chemical. Chenomx NMR Suite 9.02 software (Chenomx inc., Canada) was used to detect the ethanol and methanol peaks on the spectrum.

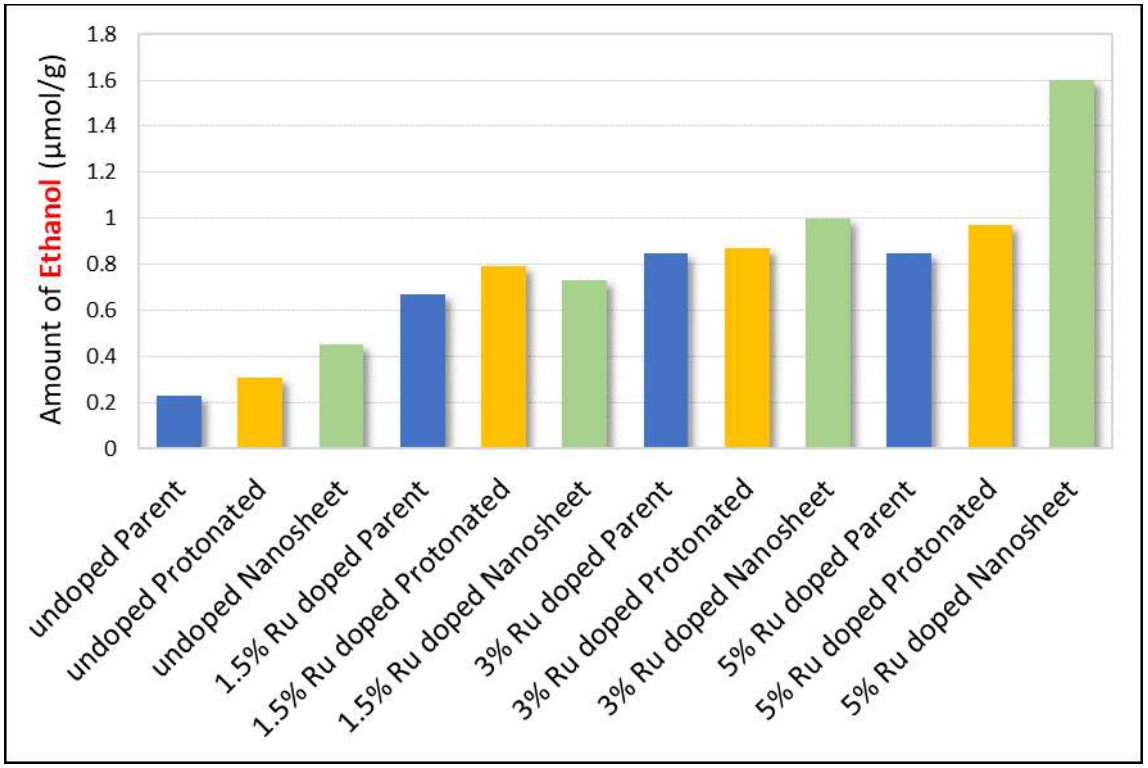

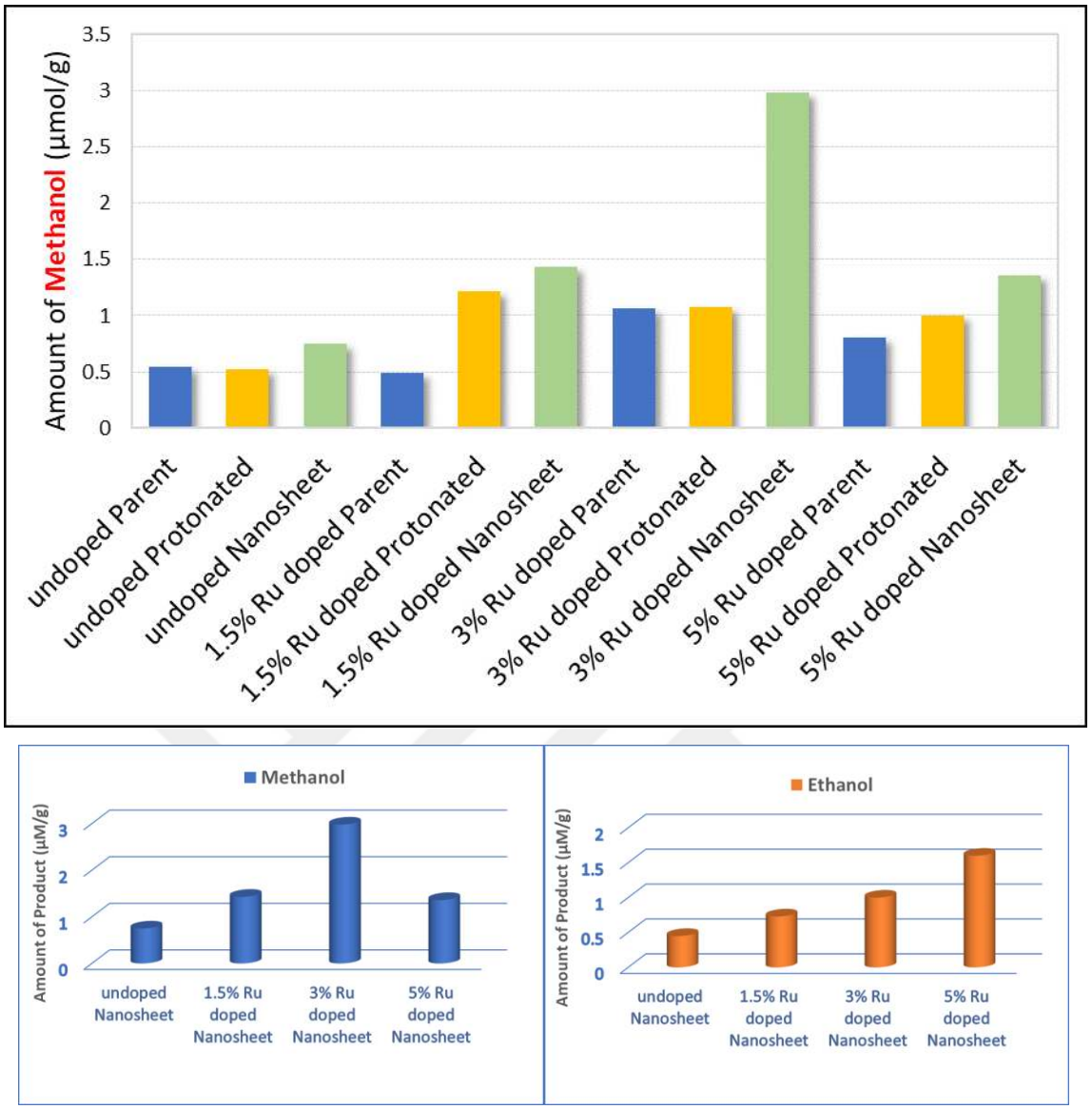

Figure 4.14: Calculated methanol and ethanol amounts from NMR results of 1 H NMR spectrum of parent, protonated and nanosheet versions of undoped and 1.5%, 3% and 5% Ruthenium doped samples.

Figure 4.14 displays the NMR results of the 6-hour photocatalytic experiments. Technical term abbreviations have been explained when first used. The graph shows the yields of methanol and ethanol in the main products. Methanol and ethanol amounts were observed to be higher in all nanosheet samples than in parent and protonated samples. This increase can be attributed to the significantly larger surface areas of the nanosheets, resulting in a higher number of active sites for CO_2 reduction reactions compared to the others. When assessing the ratios of ruthenium, it can be noted that with an increase in the amount of Ru, there is a corresponding increase in systematic ethanol production. However, there is an interesting observation when it comes to methanol, particularly in

the 3% sample where a noticeable increase is evident, contradicting the other samples. Interestingly, in the 5% sample, there is a decrease in the proportion of liquid methanol in comparison to the 3% sample. There may be various reasons for this result. As previously mentioned, the CO_2 reduction system is multielectron mechanism [192], such as methanol production (6 e- mechanism). This could pose a challenge as the photocatalyst's mechanism is liable to alteration under different mediums, giving rise to varying intermediates. In the CO_2-H_2O photocatalytic system, a suggested mechanism for methanol could be as follows [192]:

$$CO_2 + e^-_{CB} \rightarrow {}^{\cdot}CO_2^- \quad (4.1)$$

$${}^{\cdot}CO_2^- + H_2O \rightarrow HCOO^{\cdot} \quad (4.2)$$

$$HCOO^{\cdot} + e^-_{CB} \rightarrow HCOO^- \quad (4.3)$$

$$H_2O + h^+_{VB} \rightarrow H^+ + OH^{\cdot} \quad (4.4)$$

$$HCOO^- + OH^{\cdot} \rightarrow HCOOH \quad (4.5)$$

$$HCOOH + 2h^+_{VB} \rightarrow HCHO \quad (4.6)$$

$$HCHO + H^+ \rightarrow H_2{}^{\cdot}COH \rightarrow CH_3OH \quad (4.7)$$

According to this mechanism, the formation of formic acid and formaldehyde as intermediate products is observed. The diversity of these intermediate products and their conversion into different structures may be one reason for obtaining less methanol in the 5% nanosheet sample. Another issue is the possibility of methanol being converted into different products. For example, methanol can transform into ethanol through another mechanism. This is supported by the data showing a dramatic increase in ethanol in the 5% Ru doped nanosheet sample compared to the others.

4.4 Conclusion

In this chapter, photoelectrochemical and photocatalytic investigations were conducted to determine the effect of single-site Ruthenium doping on the photocatalytic CO_2 reduction performance. The single-site Ruthenium-doped $KCa_2Nb_3O_{10}$ phase was successfully synthesized in three different ratios. Chronoamperometry and Linear Sweep Voltammetry tests were performed for photoelectrochemical analysis. According the chronoamperometry experiments, the photocurrent of the Nanosheets showed a significant increase, increasing about 5 times compared to the parent material. Considering the ruthenium-doped material, a great change was observed compared to the

undoped samples. In particular, the photocurrent density of the 5% Ru-doped [CNO]-nanosheet sample was around 900 μA/cm^2, followed by 3% Ru-doped and 1.5% Ru-doped [CNO]- nanosheet was 585 μA/cm^2 and 410 μA/cm^2 respectively.

Linear sweep voltammetry analyses revealed that all nanosheet samples exhibited higher photocurrents compared to their undoped and protonated counterparts under various applied voltages. In a CO_2-saturated electrolyte under light, the cathodic current density increased with increasing ruthenium doping percentages: undoped (600 μA/cm^2), 1.5% Ru-doped (1.30 mA/cm^2), 3% Ru-doped (2.93 mA/cm^2), and 5% Ru-doped (4.10 mA/cm^2).

When comparing the electrocatalytic activity of different ruthenium-doped ratios, the 5% Ru-doped nanosheet sample demonstrated the highest cathodic current density. Ruthenium played a crucial role in enhancing photocatalytic activity by providing additional active sites for CO_2 reduction reactions. The nanosheets, especially the 5% Ru-doped sample, exhibited a significant increase in cathodic current (~4.10 mA) due to their large surface area and higher number of active sites. Both transient photocurrent response and linear sweep voltammetry results supported the improved separation efficiency of photogenerated charges for the 5% Ru-doped sample, indicating its superior photocatalytic performance.

NMR analysis was performed to examine CO_2 reduction products in the liquid phase. Main products were methanol and ethanol. Methanol and ethanol production were consistently higher in nanosheet samples compared to undoped and protonated versions, attributed to the larger surface area facilitating more active sites for CO_2 reduction reactions. With increasing ruthenium ratio, there was increase in ethanol production systematically. However, a notable increase in methanol, particularly in the 3% sample, contradicted other ratios. The complexity of the CO_2 reduction system, operating on a multielectron mechanism, and the likelihood of different intermediates under varied conditions may explain these results. The suggested mechanism for methanol involves formic acid and formaldehyde as intermediates, with their diverse structures potentially leading to lower methanol yields in the 5% nanosheet sample. Additionally, the possibility of methanol converting into ethanol is supported by data showing a significant increase in ethanol in the 5% Ru-doped nanosheet sample.

According to these results, ruthenium doping is highly effective for the photocatalytic CO_2 reduction activity. Although no gas products were obtained, valuable and useful products such as Methanol and ethanol were obtained. The

photoelectrochemical CO_2 reduction results showed a systematic increase with increasing Ru content. Through analyzing various intermediates formed during photocatalytic CO_2 experiments, the 3% Ru-doped nanosheet sample emerged as the most successful. This study has valuable insights into the development and design of 2D layered photocatalysts for future photocatalytic CO_2 reduction. It may be valuable for future research to explore the maximum doping ratio of ruthenium in the $KCa_2Nb_3O_{10}$ phase and further studies could focus on improving the selectivity.

CHAPTER 5: CONCLUSION & OUTLOOK

The research consists of three main parts, focusing on different aspects of photocatalysis, investigating the catalytic efficiency and carbon dioxide (CO2) reduction in the hydrogen evolution reaction (HER), and the hole scavenger study aimed at increasing photocatalytic activity. Different strategies are used to improve photocatalytic performance in each section.

In the first part, Hole Cleaner, the aim was to grasp the mechanical effect of hole cleaners on photocatalytic efficiency. These scavengers play a crucial role in preventing electron-hole recombination, which is a major challenge in photocatalytic activity. $[Ca_2Nb_3O_{10}]^-$nanosheets served as photocatalysts, and six different hole scavengers selected from existing literature were compared with a 0.5 M K_2SO_4 reference solution. Three particularly effective hole scavengers were subjected to detailed analysis through cyclic voltammetry and photocurrent experiments. The photocatalytic HER results showed a significant increase in photocurrent when using hole scavengers; this demonstrates their role in preventing recombination by accepting and trapping holes.

In the second chapter, Photocatalytic HER, the focus shifted to the synthesis of undoped and Pd-doped $KCa_2Nb_3O_{10}$ phases, followed by protonation to enhance photocatalytic activity. Protonated samples, especially the 3% Pd-doped nanosheets, demonstrated substantial increases in hydrogen evolution compared to undoped samples. This chapter highlighted the efficiency of single-site Pd doping and the proton exchange method in significantly boosting hydrogen production rates.

The third chapter examines the effect of single-site Ruthenium doping on photocatalytic CO_2 reduction performance in Photocatalytic CO_2 Reduction. Ruthenium-doped nanosheets exhibited enhanced photocurrents, with the 5% Ru-doped sample demonstrating superior cathodic current density in CO_2-saturated electrolyte. NMR analysis revealed methanol and ethanol as the main products, with ruthenium doping systematically increasing their production. This chapter underscored the effectiveness of ruthenium doping in enhancing photocatalytic CO_2 reduction and provided valuable insights for the design of future 2D layered photocatalysts.

This study will contribute to future clean energy research. The materials synthesized for photocatalytic CO_2 reduction and photocatalytic HER applications in this thesis have shown promising results that will shed light on future research efforts. In future studies,

these materials could be tested with different noble metals. Moreover, the doping of metals, which could be more cost-effective as single-site dopants, can be investigated. Furthermore, methods enhancing selectivity can be investigated, with photoelectrochemical methods being particularly effective in improving selectivity.

BIBLIOGRAPHY

[1] R. Lindsey, "Climate and Earth's Energy Budget Overview Incoming Sunlight Heating Imbalances Earth's Energy Budget Surface Energy Budget The Atmosphere's Energy Budget Climate Forcings and Global Warming Heat," 2009. [Online]. Available: https://earthobservatory.nasa.gov/features/EnergyBalance

[2] V. Ramanathan and Y. Feng, "Air pollution, greenhouse gases and climate change: Global and regional perspectives," *Atmos Environ*, vol. 43, no. 1, pp. 37–50, Jan. 2009, doi: 10.1016/j.atmosenv.2008.09.063.

[3] J. Houghton, "Global warming," *Reports on Progress in Physics*, vol. 68, no. 6, pp. 1343–1403, Jun. 2005, doi: 10.1088/0034-4885/68/6/R02.

[4] D. Huisingh, Z. Zhang, J. C. Moore, Q. Qiao, and Q. Li, "Recent advances in carbon emissions reduction: Policies, technologies, monitoring, assessment and modeling," *J Clean Prod*, vol. 103, pp. 1–12, 2015, doi: 10.1016/j.jclepro.2015.04.098.

[5] Hannah Ritchie, Pablo Rosado, and Max Roser, "CO_2 and Greenhouse Gas Emissions," Published online at OurWorldInData.org. Retrieved from:https://ourworldindata.org/co2-and-greenhouse-gas-emissions' [Online Resource].

[6] "Australia's Emissions Targets.-Are we on track?"

[7] S. Fawzy, A. I. Osman, J. Doran, and D. W. Rooney, "Strategies for mitigation of climate change: a review," *Environmental Chemistry Letters*, vol. 18, no. 6. Springer Science and Business Media Deutschland GmbH, pp. 2069–2094, Nov. 01, 2020. doi: 10.1007/s10311-020-01059-w.

[8] E. A. Morgan, J. Nalau, and B. Mackey, "Assessing the alignment of national-level adaptation plans to the Paris Agreement," *Environ Sci Policy*, vol. 93, pp. 208–220, Mar. 2019, doi: 10.1016/j.envsci.2018.10.012.

[9] "IEA (2022), Energy Statistics Data Browser, IEA, Paris https://www.iea.org/data-and-statistics/data-tools/energy-statistics-data-browser".

[10] "Working_Paper_-_National_Hydrogen_Strategies_-_September_2021".

[11] O. F. Noyan, M. M. Hasan, and N. Pala, "A Global Review of the Hydrogen Energy Eco-System," *Energies*, vol. 16, no. 3. MDPI, Feb. 01, 2023. doi: 10.3390/en16031484.

[12] J. M. M. Arcos and D. M. F. Santos, "The Hydrogen Color Spectrum: Techno-Economic Analysis of the Available Technologies for Hydrogen Production," *Gases*, vol. 3, no. 1, pp. 25–46, Feb. 2023, doi: 10.3390/gases3010002.

[13] H. Ishaq, I. Dincer, and C. Crawford, "A review on hydrogen production and utilization: Challenges and opportunities," *Int J*

Hydrogen Energy, vol. 47, no. 62, pp. 26238–26264, Jul. 2022, doi: 10.1016/j.ijhydene.2021.11.149.

[14] S. K. Dash, S. Chakraborty, and D. Elangovan, "A Brief Review of Hydrogen Production Methods and Their Challenges," *Energies*, vol. 16, no. 3. MDPI, Feb. 01, 2023. doi: 10.3390/en16031141.

[15] M. Hermesmann and T. E. Müller, "Green, Turquoise, Blue, or Grey? Environmentally friendly Hydrogen Production in Transforming Energy Systems," *Progress in Energy and Combustion Science*, vol. 90. Elsevier Ltd, May 01, 2022. doi: 10.1016/j.pecs.2022.100996.

[16] B. Shirizadeh and P. Quirion, "Long-term optimization of the hydrogen-electricity nexus in France: Green, blue, or pink hydrogen?," *Energy Policy*, vol. 181, p. 113702, Oct. 2023, doi: 10.1016/j.enpol.2023.113702.

[17] I. Panić, A. Cuculić, and J. Ćelić, "Color-Coded Hydrogen: Production and Storage in Maritime Sector," *Journal of Marine Science and Engineering*, vol. 10, no. 12. MDPI, Dec. 01, 2022. doi: 10.3390/jmse10121995.

[18] W. Cheng and S. Lee, "How Green Are the National Hydrogen Strategies?," *Sustainability (Switzerland)*, vol. 14, no. 3, Feb. 2022, doi: 10.3390/su14031930.

[19] J. Incer-Valverde, A. Korayem, G. Tsatsaronis, and T. Morosuk, "'Colors' of hydrogen: Definitions and carbon intensity," *Energy Convers Manag*, vol. 291, p. 117294, Sep. 2023, doi: 10.1016/j.enconman.2023.117294.

[20] G. Kakoulaki, I. Kougias, N. Taylor, F. Dolci, J. Moya, and A. Jäger-Waldau, "Green hydrogen in Europe – A regional assessment: Substituting existing production with electrolysis powered by renewables," *Energy Convers Manag*, vol. 228, Jan. 2021, doi: 10.1016/j.enconman.2020.113649.

[21] M. F. Vostakola, B. Salamatinia, and B. A. Horri, "A Review on Recent Progress in the Integrated Green Hydrogen Production Processes," *Energies*, vol. 15, no. 3. MDPI, Feb. 01, 2022. doi: 10.3390/en15031209.

[22] S. Shiva Kumar and H. Lim, "An overview of water electrolysis technologies for green hydrogen production," *Energy Reports*, vol. 8. Elsevier Ltd, pp. 13793–13813, Nov. 01, 2022. doi: 10.1016/j.egyr.2022.10.127.

[23] P. Nikolaidis and A. Poullikkas, "A comparative overview of hydrogen production processes," *Renewable and Sustainable Energy Reviews*, vol. 67. Elsevier Ltd, pp. 597–611, Jan. 01, 2017. doi: 10.1016/j.rser.2016.09.044.

[24] I. Ourya and S. Abderafi, "Technology comparison for green hydrogen production," in *IOP Conference Series: Earth and Environmental Science*, IOP Publishing Ltd, Apr. 2022. doi: 10.1088/1755-1315/1008/1/012007.

[25] M. Nasser, T. F. Megahed, S. Ookawara, and H. Hassan, "A review of water electrolysis–based systems for hydrogen production using hybrid/solar/wind energy systems," *Environmental Science and Pollution Research*, vol. 29, no. 58. Springer Science and Business Media Deutschland GmbH, pp. 86994–87018, Dec. 01, 2022. doi:

10.1007/s11356-022-23323-y.

[26] D. Zheng, Y. Xue, J. Wang, P. S. Varbanov, J. J. Klemeš, and C. Yin, "Nanocatalysts in photocatalytic water splitting for green hydrogen generation: Challenges and opportunities," *J Clean Prod*, vol. 414, Aug. 2023, doi: 10.1016/j.jclepro.2023.137700.

[27] N. Xiao, S. Li, X. Li, L. Ge, Y. Gao, and N. Li, "The roles and mechanism of cocatalysts in photocatalytic water splitting to produce hydrogen," 2020. [Online]. Available: http://www.sciencedirect.com/science/journal/18722067

[28] S. R. Lingampalli, M. M. Ayyub, and C. N. R. Rao, "Recent Progress in the Photocatalytic Reduction of Carbon Dioxide," *ACS Omega*, vol. 2, no. 6, pp. 2740–2748, Jun. 2017, doi: 10.1021/acsomega.7b00721.

[29] J. Hong, W. Zhang, J. Ren, and R. Xu, "Photocatalytic reduction of CO2: A brief review on product analysis and systematic methods," *Analytical Methods*, vol. 5, no. 5. pp. 1086–1097, Mar. 07, 2013. doi: 10.1039/c2ay26270c.

[30] F. Zhang, Y. Zhu, Q. Lin, L. Zhang, X. Zhang, and H. Wang, "Noble-metal single-atoms in thermocatalysis, electrocatalysis, and photocatalysis," *Energy and Environmental Science*, vol. 14, no. 5. Royal Society of Chemistry, pp. 2954–3009, May 01, 2021. doi: 10.1039/d1ee00247c.

[31] S. Samanta and R. Srivastava, "Catalytic conversion of CO2to chemicals and fuels: The collective thermocatalytic/photocatalytic/electrocatalytic approach with graphitic carbon nitride," *Materials Advances*, vol. 1, no. 6. Royal Society of Chemistry, pp. 1506–1545, 2020. doi: 10.1039/d0ma00293c.

[32] Q. J. Wu, J. Liang, Y. B. Huang, and R. Cao, "Thermo-, Electro-, and Photocatalytic CO2Conversion to Value-Added Products over Porous Metal/Covalent Organic Frameworks," *Acc Chem Res*, vol. 55, no. 20, pp. 2978–2997, Oct. 2022, doi: 10.1021/acs.accounts.2c00326.

[33] Y. Y. Birdja, E. Pérez-Gallent, M. C. Figueiredo, A. J. Göttle, F. Calle-Vallejo, and M. T. M. Koper, "Advances and challenges in understanding the electrocatalytic conversion of carbon dioxide to fuels," *Nature Energy*, vol. 4, no. 9. Nature Publishing Group, pp. 732–745, Sep. 01, 2019. doi: 10.1038/s41560-019-0450-y.

[34] F. Y. Gao, R. C. Bao, M. R. Gao, and S. H. Yu, "Electrochemical CO2-to-CO conversion: Electrocatalysts, electrolytes, and electrolyzers," *Journal of Materials Chemistry A*, vol. 8, no. 31. Royal Society of Chemistry, pp. 15458–15478, Aug. 21, 2020. doi: 10.1039/d0ta03525d.

[35] G. Gadikota, "Carbon mineralization pathways for carbon capture, storage and utilization," *Communications Chemistry*, vol. 4, no. 1. Nature Research, Dec. 01, 2021. doi: 10.1038/s42004-021-00461-x.

[36] L. Wu, W. Wei, L. Song, M. Woźniak-Karczewska, Ł. Chrzanowski, and B. J. Ni, "Upgrading biogas produced in anaerobic digestion: Biological removal and bioconversion of CO2 in biogas," *Renewable and Sustainable Energy Reviews*, vol. 150. Elsevier Ltd, Oct. 01,

2021. doi: 10.1016/j.rser.2021.111448.

[37] A. C. Deacy, A. F. R. Kilpatrick, A. Regoutz, and C. K. Williams, "Understanding metal synergy in heterodinuclear catalysts for the copolymerization of CO2 and epoxides," *Nat Chem*, vol. 12, no. 4, pp. 372–380, Apr. 2020, doi: 10.1038/s41557-020-0450-3.

[38] Y. Zhao, Y. Li, and L. Sun, "Recent advances in photocatalytic decomposition of water and pollutants for sustainable application," *Chemosphere*, vol. 276, Aug. 2021, doi: 10.1016/j.chemosphere.2021.130201.

[39] F. Liang, K. Zhang, L. Zhang, Y. Zhang, Y. Lei, and X. Sun, "Recent Development of Electrocatalytic CO2 Reduction Application to Energy Conversion," *Small*, vol. 17, no. 44. John Wiley and Sons Inc, Nov. 01, 2021. doi: 10.1002/smll.202100323.

[40] S. Hao *et al.*, "A Mini Review of the Preparation and Photocatalytic Properties of Two-Dimensional Materials," *Frontiers in Chemistry*, vol. 8. Frontiers Media S.A., Dec. 09, 2020. doi: 10.3389/fchem.2020.582146.

[41] G. S. Shanker, A. Biswas, and S. Ogale, "2D materials and their heterostructures for photocatalytic water splitting and conversion of CO2 to value chemicals and fuels," *JPhys Energy*, vol. 3, no. 2. IOP Publishing Ltd, Apr. 01, 2021. doi: 10.1088/2515-7655/abdcab.

[42] Y. Sun, S. Gao, F. Lei, and Y. Xie, "Atomically-thin two-dimensional sheets for understanding active sites in catalysis," *Chemical Society Reviews*, vol. 44, no. 3. Royal Society of Chemistry, pp. 623–636, Feb. 07, 2015. doi: 10.1039/c4cs00236a.

[43] X. Bao, Q. Ou, Z. Q. Xu, Y. Zhang, Q. Bao, and H. Zhang, "Band Structure Engineering in 2D Materials for Optoelectronic Applications," *Advanced Materials Technologies*, vol. 3, no. 11. Wiley-Blackwell, Nov. 01, 2018. doi: 10.1002/admt.201800072.

[44] F. Chen, Y. Zhang, and H. Huang, "Layered photocatalytic nanomaterials for environmental applications," *Chinese Chemical Letters*, vol. 34, no. 3, Mar. 2023, doi: 10.1016/j.cclet.2022.05.037.

[45] Y. Zhao, S. Zhang, R. Shi, G. I. N. Waterhouse, J. Tang, and T. Zhang, "Two-dimensional photocatalyst design: A critical review of recent experimental and computational advances," *Materials Today*, vol. 34. Elsevier B.V., pp. 78–91, Apr. 01, 2020. doi: 10.1016/j.mattod.2019.10.022.

[46] M. Aggarwal, N. P. Shetti, S. Basu, and T. M. Aminabhavi, "Two-dimensional ultrathin metal-based nanosheets for photocatalytic CO2 conversion to solar fuels," *Journal of Environmental Management*, vol. 313. Academic Press, Jul. 01, 2022. doi: 10.1016/j.jenvman.2022.114916.

[47] C. Candia-Onfray, S. Rojas, M. V. B. Zanoni, and R. Salazar, "An updated review of metal–organic framework materials in photo(electro)catalytic applications: From CO2 reduction to wastewater treatments," *Current Opinion in Electrochemistry*, vol. 26. Elsevier B.V., Apr. 01, 2021. doi: 10.1016/j.coelec.2020.100669.

[48] D. Li, H. Q. Xu, L. Jiao, and H. L. Jiang, "Metal-organic frameworks for catalysis: State of the art, challenges, and opportunities," *EnergyChem*, vol. 1, no. 1. Elsevier B.V., Jul. 01, 2019. doi:

10.1016/j.enchem.2019.100005.

[49] M. Guo, M. Zhang, R. Liu, X. Zhang, and G. Li, "State-of-the-Art Advancements in Photocatalytic Hydrogenation: Reaction Mechanism and Recent Progress in Metal-Organic Framework (MOF)-Based Catalysts," *Advanced Science*, vol. 9, no. 1. John Wiley and Sons Inc, Jan. 01, 2022. doi: 10.1002/advs.202103361.

[50] P. Behera, S. Subudhi, S. P. Tripathy, and K. Parida, "MOF derived nano-materials: A recent progress in strategic fabrication, characterization and mechanistic insight towards divergent photocatalytic applications," *Coordination Chemistry Reviews*, vol. 456. Elsevier B.V., Apr. 01, 2022. doi: 10.1016/j.ccr.2021.214392.

[51] Q. Wang, Q. Gao, A. M. Al-Enizi, A. Nafady, and S. Ma, "Recent advances in MOF-based photocatalysis: Environmental remediation under visible light," *Inorganic Chemistry Frontiers*, vol. 7, no. 2. Royal Society of Chemistry, pp. 300–339, Jan. 21, 2020. doi: 10.1039/c9qi01120j.

[52] J. Wen, J. Xie, X. Chen, and X. Li, "A review on g-C 3 N 4 -based photocatalysts," *Appl Surf Sci*, vol. 391, pp. 72–123, Jan. 2017, doi: 10.1016/j.apsusc.2016.07.030.

[53] S. Ye, R. Wang, M. Z. Wu, and Y. P. Yuan, "A review on g-C 3 N 4 for photocatalytic water splitting and CO 2 reduction," in *Applied Surface Science*, Elsevier B.V., Dec. 2015, pp. 15–27. doi: 10.1016/j.apsusc.2015.08.173.

[54] X. Wang *et al.*, "A metal-free polymeric photocatalyst for hydrogen production from water under visible light," *Nat Mater*, vol. 8, no. 1, pp. 76–80, 2009, doi: 10.1038/nmat2317.

[55] G. Mamba and A. K. Mishra, "Graphitic carbon nitride (g-C3N4) nanocomposites: A new and exciting generation of visible light driven photocatalysts for environmental pollution remediation," *Applied Catalysis B: Environmental*, vol. 198. Elsevier B.V., pp. 347–377, Dec. 05, 2016. doi: 10.1016/j.apcatb.2016.05.052.

[56] G. Dong, Y. Zhang, Q. Pan, and J. Qiu, "A fantastic graphitic carbon nitride (g-C3N4) material: Electronic structure, photocatalytic and photoelectronic properties," *Journal of Photochemistry and Photobiology C: Photochemistry Reviews*, vol. 20, no. 1. Elsevier, pp. 33–50, 2014. doi: 10.1016/j.jphotochemrev.2014.04.002.

[57] J. Xu, L. Zhang, R. Shi, and Y. Zhu, "Chemical exfoliation of graphitic carbon nitride for efficient heterogeneous photocatalysis," *J Mater Chem A Mater*, vol. 1, no. 46, pp. 14766–14772, Dec. 2013, doi: 10.1039/c3ta13188b.

[58] X. Liu *et al.*, "Recent developments of doped g-C3N4 photocatalysts for the degradation of organic pollutants," *Crit Rev Environ Sci Technol*, vol. 51, no. 8, pp. 751–790, 2021, doi: 10.1080/10643389.2020.1734433.

[59] Z. Chen *et al.*, "Synthesis and fabrication of g-C3N4-based materials and their application in elimination of pollutants," *Science of the Total Environment*, vol. 731. Elsevier B.V., Aug. 20, 2020. doi: 10.1016/j.scitotenv.2020.139054.

[60] S. Yin, J. Han, T. Zhou, and R. Xu, "Recent progress in g-C3N4 based low cost photocatalytic system: Activity enhancement and

emerging applications," *Catalysis Science and Technology*, vol. 5, no. 12. Royal Society of Chemistry, pp. 5048–5061, Jul. 15, 2015. doi: 10.1039/c5cy00938c.

[61] Z. Otgonbayar and W. C. Oh, "MXene-based nanocomposite for the photocatalytic CO2 reduction: Comprehensive review," *Molecular Catalysis*, vol. 541. Elsevier B.V., Apr. 15, 2023. doi: 10.1016/j.mcat.2023.113085.

[62] J. Shen *et al.*, "Emerging applications of MXene materials in CO2 photocatalysis," *FlatChem*, vol. 28, Jul. 2021, doi: 10.1016/j.flatc.2021.100252.

[63] T. P. Nguyen *et al.*, "MXenes: Applications in electrocatalytic, photocatalytic hydrogen evolution reaction and CO2 reduction," *Molecular Catalysis*, vol. 486. Elsevier B.V., May 01, 2020. doi: 10.1016/j.mcat.2020.110850.

[64] S. Cao, B. Shen, T. Tong, J. Fu, and J. Yu, "2D/2D Heterojunction of Ultrathin MXene/Bi2WO6 Nanosheets for Improved Photocatalytic CO2 Reduction," *Adv Funct Mater*, vol. 28, no. 21, May 2018, doi: 10.1002/adfm.201800136.

[65] Z. Guo, J. Zhou, L. Zhu, and Z. Sun, "MXene: A promising photocatalyst for water splitting," *J Mater Chem A Mater*, vol. 4, no. 29, pp. 11446–11452, 2016, doi: 10.1039/c6ta04414j.

[66] "Advanced Materials - 2011 - Naguib - Two-Dimensional Nanocrystals Two-Dimensional Nanocrystals Produced by Exfoliation of".

[67] X. Zhang, Z. Zhang, J. Li, X. Zhao, D. Wu, and Z. Zhou, "Ti2CO2 MXene: A highly active and selective photocatalyst for CO2 reduction," *J Mater Chem A Mater*, vol. 5, no. 25, pp. 12899–12903, 2017, doi: 10.1039/c7ta03557h.

[68] C. Karthikeyan, P. Arunachalam, K. Ramachandran, A. M. Al-Mayouf, and S. Karuppuchamy, "Recent advances in semiconductor metal oxides with enhanced methods for solar photocatalytic applications," *Journal of Alloys and Compounds*, vol. 828. Elsevier Ltd, Jul. 05, 2020. doi: 10.1016/j.jallcom.2020.154281.

[69] W. Jiang *et al.*, "Role of oxygen vacancy in metal oxides for photocatalytic CO2 reduction," *Applied Catalysis B: Environmental*, vol. 321. Elsevier B.V., Feb. 01, 2023. doi: 10.1016/j.apcatb.2022.122079.

[70] F. M. Sanakousar, C. Vidyasagar, V. M. Jiménez-Pérez, and K. Prakash, "Recent progress on visible-light-driven metal and non-metal doped ZnO nanostructures for photocatalytic degradation of organic pollutants," *Materials Science in Semiconductor Processing*, vol. 140. Elsevier Ltd, Mar. 15, 2022. doi: 10.1016/j.mssp.2021.106390.

[71] K. M. Lee, C. W. Lai, K. S. Ngai, and J. C. Juan, "Recent developments of zinc oxide based photocatalyst in water treatment technology: A review," *Water Research*, vol. 88. Elsevier Ltd, pp. 428–448, Jan. 01, 2016. doi: 10.1016/j.watres.2015.09.045.

[72] A. L. T. Zheng, C. A. C. Abdullah, E. L. T. Chung, and Y. Andou, "Recent progress in visible light-doped ZnO photocatalyst for pollution control," *International Journal of Environmental Science*

and Technology, vol. 20, no. 5. Institute for Ionics, pp. 5753–5772, May 01, 2023. doi: 10.1007/s13762-022-04354-x.

[73] Z. Li, S. Wang, J. Wu, and W. Zhou, "Recent progress in defective TiO2 photocatalysts for energy and environmental applications," *Renewable and Sustainable Energy Reviews*, vol. 156. Elsevier Ltd, Mar. 01, 2022. doi: 10.1016/j.rser.2021.111980.

[74] A. S. M. Nur *et al.*, "A review on the development of elemental and codoped TiO2 photocatalysts for enhanced dye degradation under UV–vis irradiation," *Journal of Water Process Engineering*, vol. 47, p. 102728, Jun. 2022, doi: 10.1016/j.jwpe.2022.102728.

[75] M. Shuaib, "Layer-by-Layer Assembly of Perovskite Nanosheets and Its Applications to Electronic Materials ペロブスカイトナノシートのレイヤーバ　イレイヤー集積とその電子材料への応用," 2017.

[76] B. J. Sahiga and W. Tio Putra, "Special Issue II) August (2018) Res."

[77] W. Zhang, K. Fujii, E. Niwa, M. Hagihala, T. Kamiyama, and M. Yashima, "Oxide-ion conduction in the Dion–Jacobson phase CsBi2Ti2NbO10−δ," *Nat Commun*, vol. 11, no. 1, Dec. 2020, doi: 10.1038/s41467-020-15043-z.

[78] A. J. Jacobson, J. T. Lewandowski, and J. W. Johnson, "ION EXCHANGE OF THE LAYERED PEROVSKITE KCa2Nb3010 BY PROTONS*," 1986.

[79] A. J. Jacobson, J. T. Lewandowski, and J. W. Johnson, "ION EXCHANGE REACTIONS OF THE LAYERED SOLID ACID HCa2Nb3Olo WITH ALKALI METAL CATIONS," 1990.

[80] Y. Hu *et al.*, "Layered perovskite oxides and their derivative nanosheets adopting different modification strategies towards better photocatalytic performance of water splitting," *Renewable and Sustainable Energy Reviews*, vol. 119. Elsevier Ltd, Mar. 01, 2020. doi: 10.1016/j.rser.2019.109527.

[81] Y. Li and S. C. E. Tsang, "Recent progress and strategies for enhancing photocatalytic water splitting," *Materials Today Sustainability*, vol. 9. Elsevier Ltd, Sep. 01, 2020. doi: 10.1016/j.mtsust.2020.100032.

[82] D. Liu *et al.*, "Single noble metal atoms doped 2D materials for catalysis," *Applied Catalysis B: Environmental*, vol. 297. Elsevier B.V., Nov. 15, 2021. doi: 10.1016/j.apcatb.2021.120389.

[83] K. Khan *et al.*, "Recent Progress, Challenges, and Prospects in Two-Dimensional Photo-Catalyst Materials and Environmental Remediation," *Nano-Micro Letters*, vol. 12, no. 1. Springer, Aug. 01, 2020. doi: 10.1007/s40820-020-00504-3.

[84] D. P. Kumar *et al.*, "Ultrathin layered Zn-doped MoS2 nanosheets deposited onto CdS nanorods for spectacular photocatalytic hydrogen evolution," *J Alloys Compd*, vol. 905, Apr. 2022, doi: 10.1016/j.jallcom.2022.164193.

[85] S. Cao *et al.*, "Single-Atom Engineering of Directional Charge Transfer Channels and Active Sites for Photocatalytic Hydrogen Evolution," *Adv Funct Mater*, vol. 28, no. 32, Aug. 2018, doi: 10.1002/adfm.201802169.

[86] X. Li, Z. Zhuang, W. Li, and H. Pan, "Photocatalytic reduction of

CO2over noble metal-loaded and nitrogen-doped mesoporous TiO2," *Appl Catal A Gen*, vol. 429–430, pp. 31–38, Jul. 2012, doi: 10.1016/j.apcata.2012.04.001.

[87] G. S. Shanker, A. Biswas, and S. Ogale, "2D materials and their heterostructures for photocatalytic water splitting and conversion of CO2 to value chemicals and fuels," *JPhys Energy*, vol. 3, no. 2. IOP Publishing Ltd, Apr. 01, 2021. doi: 10.1088/2515-7655/abdcab.

[88] H. She *et al.*, "Construction of a Two-Dimensional Composite Derived from TiO2 and SnS2 for Enhanced Photocatalytic Reduction of CO2 into CH4," *ACS Sustain Chem Eng*, vol. 7, no. 1, pp. 650–659, Jan. 2019, doi: 10.1021/acssuschemeng.8b04250.

[89] R. Zhong, Z. Zhang, S. Luo, Z. C. Zhang, L. Huang, and M. Gu, "Comparison of TiO 2 and g-C 3 N 4 2D/2D nanocomposites from three synthesis protocols for visible-light induced hydrogen evolution," *Catal Sci Technol*, vol. 9, no. 1, pp. 75–85, 2019, doi: 10.1039/c8cy00965a.

[90] R. tang Guo *et al.*, "Photocatalytic reduction of CO2 into CO over nanostructure Bi2S3 quantum dots/g-C3N4 composites with Z-scheme mechanism," *Appl Surf Sci*, vol. 500, Jan. 2020, doi: 10.1016/j.apsusc.2019.144059.

[91] Z. Guo, H. Wu, M. Li, T. Tang, J. Wen, and X. Li, "Phosphorus-doped graphene quantum dots loaded on TiO2 for enhanced photodegradation," *Appl Surf Sci*, vol. 526, Oct. 2020, doi: 10.1016/j.apsusc.2020.146724.

[92] R. Long, N. J. English, and O. V. Prezhdo, "Minimizing electron-hole recombination on TiO2 sensitized with PbSe quantum dots: Time-domain Ab initio analysis," *Journal of Physical Chemistry Letters*, vol. 5, no. 17, pp. 2941–2946, Sep. 2014, doi: 10.1021/jz5013627.

[93] J. M. Elward and A. Chakraborty, "Effect of heterojunction on exciton binding energy and electron-hole recombination probability in CdSe/ZnS quantum dots," *J Chem Theory Comput*, vol. 11, no. 2, pp. 462–471, Feb. 2015, doi: 10.1021/ct500548x.

[94] K. Izawa *et al.*, "Photoelectrochemical oxidation of methanol on oxide nanosheets," *Journal of Physical Chemistry B*, vol. 110, no. 10, pp. 4645–4650, Mar. 2006, doi: 10.1021/jp056210l.

[95] N. Denisov, J. E. Yoo, and P. Schmuki, "Effect of different hole scavengers on the photoelectrochemical properties and photocatalytic hydrogen evolution performance of pristine and Pt-decorated TiO2 nanotubes," *Electrochim Acta*, vol. 319, pp. 61–71, Oct. 2019, doi: 10.1016/j.electacta.2019.06.173.

[96] H. Pan and M. D. Heagy, "Bicarbonate reduction with semiconductor photocatalysts: Study of effect of positive hole scavengers," *MRS Commun*, vol. 8, no. 3, pp. 1173–1177, Sep. 2018, doi: 10.1557/mrc.2018.177.

[97] T. T. D. Nguyen *et al.*, "The roles of ethanol and isopropanol as hole scavengers in the photoreduction reaction of graphene oxide by TiO2: A competition of oxygenated groups removal and carbon defects invasion," *J Mol Liq*, vol. 381, Jul. 2023, doi: 10.1016/j.molliq.2023.121831.

[98] M. Tahir, "Vanadium Carbide (V2CTx) MXene-Supported Exfoliated g-C3N4 with the Role of Hole Scavenger as a Rapid Electron Transfer Channel for Enhancing Photocatalytic CO2 Reduction to CO and CH4," *Energy and Fuels*, vol. 37, no. 14, pp. 10615–10630, Jul. 2023, doi: 10.1021/acs.energyfuels.3c01301.

[99] T. ming Su, Z. zeng Qin, H. bing Ji, Y. xiu Jiang, and G. Huang, "Recent advances in the photocatalytic reduction of carbon dioxide," *Environmental Chemistry Letters*, vol. 14, no. 1. Springer Verlag, pp. 99–112, Mar. 01, 2016. doi: 10.1007/s10311-015-0528-0.

[100] K. Li, X. An, K. H. Park, M. Khraisheh, and J. Tang, "A critical review of CO2 photoconversion: Catalysts and reactors," *Catal Today*, vol. 224, pp. 3–12, 2014, doi: 10.1016/j.cattod.2013.12.006.

[101] S. N. Habisreutinger, L. Schmidt-Mende, and J. K. Stolarczyk, "Photocatalytic reduction of CO2 on TiO2 and other semiconductors," *Angewandte Chemie - International Edition*, vol. 52, no. 29. pp. 7372–7408, Jul. 15, 2013. doi: 10.1002/anie.201207199.

[102] J. Z. Y. Tan and M. M. Maroto-Valer, "A review of nanostructured non-titania photocatalysts and hole scavenging agents for CO2 photoreduction processes," *Journal of Materials Chemistry A*, vol. 7, no. 16. Royal Society of Chemistry, pp. 9368–9385, 2019. doi: 10.1039/c8ta10410g.

[103] B. R. Shah and U. D. Patel, "Mechanistic aspects of photocatalytic degradation of Lindane by TiO2in the presence of Oxalic acid and EDTA as hole-scavengers," *J Environ Chem Eng*, vol. 9, no. 4, Aug. 2021, doi: 10.1016/j.jece.2021.105458.

[104] S. T. Gebre *et al.*, "Amine Hole Scavengers Facilitate Both Electron and Hole Transfer in a Nanocrystal/Molecular Hybrid Photocatalyst," *J Am Chem Soc*, vol. 145, no. 5, pp. 3238–3247, Feb. 2023, doi: 10.1021/jacs.2c13464.

[105] T. T. D. Nguyen *et al.*, "The roles of ethanol and isopropanol as hole scavengers in the photoreduction reaction of graphene oxide by TiO2: A competition of oxygenated groups removal and carbon defects invasion," *J Mol Liq*, vol. 381, Jul. 2023, doi: 10.1016/j.molliq.2023.121831.

[106] Y. Wei *et al.*, "Synergistic impact of cocatalysts and hole scavenger for promoted photocatalytic H2 evolution in mesoporous TiO2–NiSx hybrid," *Journal of Energy Chemistry*, pp. 45–56, May 2019, doi: 10.1016/j.jechem.2018.05.013.

[107] Z. Jiang, R. Qi, Z. Huang, W. Shangguan, R. J. Wong, and A. Lee, "Impact of Methanol Photomediated Surface Defects on Photocatalytic H2 Production Over Pt/TiO2," *Energy and Environmental Materials*, vol. 3, no. 2, pp. 202–208, Jun. 2020, doi: 10.1002/eem2.12068.

[108] A. W. Mureithi, Y. Sun, T. Mani, A. R. Howell, and J. Zhao, "Impact of hole scavengers on photocatalytic reduction of nitrobenzene using cadmium sulfide quantum dots," *Cell Rep Phys Sci*, vol. 3, no. 5, May 2022, doi: 10.1016/j.xcrp.2022.100889.

[109] K. Doudrick, T. Yang, K. Hristovski, and P. Westerhoff, "Photocatalytic nitrate reduction in water: Managing the hole

scavenger and reaction by-product selectivity," *Appl Catal B*, vol. 136–137, pp. 40–47, Jun. 2013, doi: 10.1016/j.apcatb.2013.01.042.

[110] M. Shen and M. A. Henderson, "Identification of the active species in photochemical hole scavenging reactions of methanol on TiO2," *Journal of Physical Chemistry Letters*, vol. 2, no. 21, pp. 2707–2710, Nov. 2011, doi: 10.1021/jz201242k.

[111] S. Rengaraj and X. Z. Li, "Enhanced photocatalytic reduction reaction over Bi3+-TiO2 nanoparticles in presence of formic acid as a hole scavenger," *Chemosphere*, vol. 66, no. 5, pp. 930–938, 2007, doi: 10.1016/j.chemosphere.2006.06.007.

[112] A. Sowmya and S. Meenakshi, "Photocatalytic reduction of nitrate over Ag-TiO2 in the presence of oxalic acid," *Journal of Water Process Engineering*, vol. 8, pp. e23–e30, Dec. 2015, doi: 10.1016/j.jwpe.2014.11.004.

[113] H. Dotan, K. Sivula, M. Grätzel, A. Rothschild, and S. C. Warren, "Probing the photoelectrochemical properties of hematite (α-Fe 2O3) electrodes using hydrogen peroxide as a hole scavenger," *Energy Environ Sci*, vol. 4, no. 3, pp. 958–964, Mar. 2011, doi: 10.1039/c0ee00570c.

[114] X. Huang *et al.*, "Recent advances of doped graphite carbon nitride for photocatalytic reduction of CO2: a review," *Research on Chemical Intermediates*, vol. 46, no. 12. Springer Science and Business Media B.V., pp. 5133–5164, Dec. 01, 2020. doi: 10.1007/s11164-020-04278-6.

[115] M. J. Berr *et al.*, "Hole scavenger redox potentials determine quantum efficiency and stability of Pt-decorated CdS nanorods for photocatalytic hydrogen generation," *Appl Phys Lett*, vol. 100, no. 22, May 2012, doi: 10.1063/1.4723575.

[116] C. Ladasiu, N. Kulischow, R. Marschall, C. Ladasiu, N. Kulischow, and R. Marschall, "Tuning the Photocatalytic Activity of Layered Perovskite Niobates by Controlled Ion Exchange and Hydration."

[117] P. Makuła, M. Pacia, and W. Macyk, "How To Correctly Determine the Band Gap Energy of Modified Semiconductor Photocatalysts Based on UV-Vis Spectra," *Journal of Physical Chemistry Letters*, vol. 9, no. 23. American Chemical Society, pp. 6814–6817, Dec. 06, 2018. doi: 10.1021/acs.jpclett.8b02892.

[118] L. Shi *et al.*, "Annealing temperature effects on photoelectrochemical performance of bismuth vanadate thin film photoelectrodes," *RSC Adv*, vol. 8, no. 51, pp. 29179–29188, 2018, doi: 10.1039/c8ra04887h.

[119] N. Denisov, J. Yoo, and P. Schmuki, "Effect of different hole scavengers on the photoelectrochemical properties and photocatalytic hydrogen evolution performance of pristine and Pt-decorated TiO2 nanotubes." [Online]. Available: https://www.sciencedirect.com/science/article/pii/S0013468619313167

[120] M. Ahmad, X. Quan, S. Chen, H. Yu, and Z. Zeng, "Operating redox couple transport mechanism for enhancing photocatalytic H2 generation of Pt and CrOx-decorated ZnCdS nanocrystals," *Appl Catal B*, vol. 283, Apr. 2021, doi: 10.1016/j.apcatb.2020.119601.

[121] E. Kalamaras and P. Lianos, "Current Doubling effect revisited: Current multiplication in a PhotoFuelCell," *Journal of Electroanalytical Chemistry*, vol. 751, pp. 37–42, Jun. 2015, doi: 10.1016/j.jelechem.2015.05.029.
[122] "A. Manivannan et al: Investigation of Current Doubling Reactions."
[123] G. J. Gerardi, E. H. Poindexter, B. E. Conway, and D. F. Tessier, "Investigation of 'Current Doubling' Mechanism of Organic Compounds by the Rotating Ring Disk Electrode Technique You may also like Generation of P b Centers by High Electric Fields: Thermochemical Effects Temperature Dependence of the Tafel Slope and Electrochemical Barrier Symmetry Factor, in Electrode Kinetics."
[124] C. P. Thurgood, D. W. Kirk, and F. R. Foulkes, "To cite this article: Yasuhisa Maeda et al," 1981.
[125] N. Hykaway, W. M. Sears, H. Morisaki, and S. R. Morrison, "Current-Doubling Reactions on Titanium Dioxide Photoanodes," 1986. [Online]. Available: https://pubs.acs.org/sharingguidelines
[126] B. Jung *et al.*, "Photocatalytic reduction of chlorate in aqueous TiO 2 suspension with hole scavenger under simulated solar light", doi: 10.1007/s42247-020-00145-7/Published.
[127] X. Cai, Y. Luo, B. Liu, and H. M. Cheng, "Preparation of 2D material dispersions and their applications," *Chemical Society Reviews*, vol. 47, no. 16. Royal Society of Chemistry, pp. 6224–6266, Aug. 21, 2018. doi: 10.1039/c8cs00254a.
[128] D. Liu *et al.*, "Single noble metal atoms doped 2D materials for catalysis," *Applied Catalysis B: Environmental*, vol. 297. Elsevier B.V., Nov. 15, 2021. doi: 10.1016/j.apcatb.2021.120389.
[129] A. J. Jacobson, J. T. Lewandowski, and J. W. Johnson, "ION EXCHANGE OF THE LAYERED PEROVSKITE KCa2Nb3010 BY PROTONS*," 1986.
[130] Y. Ebina, T. Sasaki, M. Harada, and M. Watanabe, "Restacked perovskite nanosheets and their Pt-loaded materials as photocatalysts," *Chemistry of Materials*, vol. 14, no. 10, pp. 4390–4395, Oct. 2002, doi: 10.1021/cm020622e.
[131] H. D. Acta and S. S. Spectroscopy, "Less-Common Met," 1991.
[132] C. Sun, P. Peng, L. Zhu, W. Zheng, and Y. Zhao, "Designed reversible alkylamine intercalation-deintercalation in the layered perovskite-type oxide KCa2Nb3O10," *Eur J Inorg Chem*, no. 24, pp. 3864–3870, 2008, doi: 10.1002/ejic.200800271.
[133] G. W. Graham, A. E. O'neill Ay, D. Uy, W. H. Weber, H. Sun, and X. Q. Pan, "Observation of strained PdO in an aged Pd/ceria±zirconia catalyst."
[134] F. Zaccarini, R. Bakker, and E. Pushkarev, "RAMAN SPECTROSCOPY AND ELECTRON MICROPROBE CHARACTERISATION OF A Pt-Fe-Pd-Ni-Cu OXIDE FROM NURALI CHROMITITE, SOUTHERN URALS, RUSSIA MiLeSlag-Mineralogy and Leachability of Steel Slags View project Mineralogy and genesis of precious-, rare-, and critical metals in hydrothermal ore deposits of Greece View project," 2018. [Online]. Available: https://www.researchgate.net/publication/327681420

[135] A. Baylet, P. Marécot, D. Duprez, P. Castellazzi, G. Groppi, and P. Forzatti, "In situ Raman and in situ XRD analysis of PdO reduction and Pd° oxidation supported on γ-Al2O3 catalyst under different atmospheres," *Physical Chemistry Chemical Physics*, vol. 13, no. 10, pp. 4607–4613, Mar. 2011, doi: 10.1039/c0cp01331e.

[136] F. Ascencio, C. Reyes-Damián, and R. Escudero, "Macroscopic Quantum Tunneling in PdO Nanoparticles," *J Supercond Nov Magn*, vol. 34, no. 5, pp. 1499–1506, May 2021, doi: 10.1007/s10948-021-05866-2.

[137] J. Yoshimura, Y. Ebina, J. Kondo, K. Domen', Y. 227, and J. A. Tanaka, "Visible Light Induced Photocatalytic Behavior of a Layered Perovskite Type Niobate, RbPb2Nb3O10," 1993. [Online]. Available: https://pubs.acs.org/sharingguidelines

[138] C. Yang *et al.*, "Core-shell nanostructured 'black' Rutile Titania as excellent catalyst for hydrogen production enhanced by sulfur doping," *J Am Chem Soc*, vol. 135, no. 47, pp. 17831–17838, Nov. 2013, doi: 10.1021/ja4076748.

[139] X. An, C. Hu, H. Liu, and J. Qu, "Hierarchical Nanotubular Anatase/Rutile/TiO2(B) Heterophase Junction with Oxygen Vacancies for Enhanced Photocatalytic H2 Production," *Langmuir*, vol. 34, no. 5, pp. 1883–1889, Feb. 2018, doi: 10.1021/acs.langmuir.7b03745.

[140] M. Q. Yang, X. Pan, N. Zhang, and Y. J. Xu, "A facile one-step way to anchor noble metal (Au, Ag, Pd) nanoparticles on a reduced graphene oxide mat with catalytic activity for selective reduction of nitroaromatic compounds," *CrystEngComm*, vol. 15, no. 34, pp. 6819–6828, Sep. 2013, doi: 10.1039/c3ce40694f.

[141] S. Ida, Y. Okamoto, S. Koga, H. Hagiwara, and T. Ishihara, "Black-colored nitrogen-doped calcium niobium oxide nanosheets and their photocatalytic properties under visible light irradiation," *RSC Adv*, vol. 3, no. 29, pp. 11521–11524, Aug. 2013, doi: 10.1039/c3ra40638e.

[142] B. Siritanaratkul, K. Maeda, T. Hisatomi, and K. Domen, "Synthesis and photocatalytic activity of perovskite niobium oxynitrides with wide visible-light absorption bands," *ChemSusChem*, vol. 4, no. 1, pp. 74–78, Jan. 2011, doi: 10.1002/cssc.201000207.

[143] A. Kubacka, M. Fernández-García, and G. Colón, "Advanced nanoarchitectures for solar photocatalytic applications," *Chemical Reviews*, vol. 112, no. 3. pp. 1555–1614, Mar. 14, 2012. doi: 10.1021/cr100454n.

[144] D. Neagu and J. T. S. Irvine, "Enhancing electronic conductivity in strontium titanates through correlated A and B-site doping," *Chemistry of Materials*, vol. 23, no. 6, pp. 1607–1617, Mar. 2011, doi: 10.1021/cm103489r.

[145] D. Kim, Z. Zhang, and K. Yong, "Synergistic doping effects of a ZnO:N/BiVO4:Mo bunched nanorod array photoanode for enhancing charge transfer and carrier density in photoelectrochemical systems," *Nanoscale*, vol. 10, no. 43, pp. 20256–20265, Nov. 2018, doi: 10.1039/c8nr06630b.

[146] N. O. Laschuk, E. B. Easton, and O. V. Zenkina, "Reducing the

resistance for the use of electrochemical impedance spectroscopy analysis in materials chemistry," *RSC Advances*, vol. 11, no. 45. Royal Society of Chemistry, pp. 27925–27936, Aug. 08, 2021. doi: 10.1039/d1ra03785d.

[147] R. Huang, J. Wu, M. Zhang, B. Liu, Z. Zheng, and D. Luo, "Strategies to enhance photocatalytic activity of graphite carbon nitride-based photocatalysts," *Mater Des*, vol. 210, Nov. 2021, doi: 10.1016/j.matdes.2021.110040.

[148] D. Jiang *et al.*, "KCa2Nb3O10/ZnIn2S4 nanosheet heterojunctions with improved charge separation efficiency for efficient photocatalytic CO2 reduction," *J Alloys Compd*, vol. 865, Jun. 2021, doi: 10.1016/j.jallcom.2021.158836.

[149] Q. Lu, H. You, W. Fang, X. Li, and X. Zeng, "Boosting visible-light photocatalytic hydrogen evolution over layered 2 perovskite by incorporating CdS quantum dots." [Online]. Available: https://ssrn.com/abstract=4402638

[150] B. Tian, W. Gao, X. Zhang, Y. Wu, and G. Lu, "Water splitting over core-shell structural nanorod CdS@Cr2O3 catalyst by inhibition of H2-O2 recombination via removing nascent formed oxygen using perfluorodecalin," *Appl Catal B*, vol. 221, pp. 618–625, 2018, doi: 10.1016/j.apcatb.2017.09.065.

[151] K. Maeda *et al.*, "Photocatalytic Overall Water Splitting Promoted by Two Different Cocatalysts for Hydrogen and Oxygen Evolution under Visible Light," *Angewandte Chemie*, vol. 122, no. 24, pp. 4190–4193, Jun. 2010, doi: 10.1002/ange.201001259.

[152] R. Shi, G. I. N. Waterhouse, and T. Zhang, "Recent Progress in Photocatalytic CO2 Reduction Over Perovskite Oxides," *Solar RRL*, vol. 1, no. 11. Wiley-VCH Verlag, Nov. 01, 2017. doi: 10.1002/solr.201700126.

[153] J. Ran, M. Jaroniec, and S. Z. Qiao, "Cocatalysts in Semiconductor-based Photocatalytic CO2 Reduction: Achievements, Challenges, and Opportunities," *Advanced Materials*, vol. 30, no. 7. Wiley-VCH Verlag, Feb. 15, 2018. doi: 10.1002/adma.201704649.

[154] Y. He, Y. Wang, L. Zhang, B. Teng, and M. Fan, "High-efficiency conversion of CO2 to fuel over ZnO/g-C3N4 photocatalyst," *Appl Catal B*, vol. 168–169, pp. 1–8, Jun. 2015, doi: 10.1016/j.apcatb.2014.12.017.

[155] F. Fresno *et al.*, "Selectivity in UV photocatalytic CO2 conversion over bare and silver-decorated niobium-tantalum perovskites," *Catal Today*, vol. 361, pp. 85–93, Feb. 2021, doi: 10.1016/j.cattod.2020.01.013.

[156] F. Yoshitomi, K. Sekizawa, K. Maeda, and O. Ishitani, "Selective Formic Acid Production via CO2 Reduction with Visible Light Using a Hybrid of a Perovskite Tantalum Oxynitride and a Binuclear Ruthenium(II) Complex," *ACS Appl Mater Interfaces*, vol. 7, no. 23, pp. 13092–13097, Jun. 2015, doi: 10.1021/acsami.5b03509.

[157] T. Biswal, K. P. Shadangi, P. K. Sarangi, and R. K. Srivastava, "Conversion of carbon dioxide to methanol: A comprehensive review," *Chemosphere*, vol. 298, Jul. 2022, doi: 10.1016/j.chemosphere.2022.134299.

[158] J. Wu *et al.*, "Research advances in the light-driven conversion of CO2 to valuable chemicals by two-dimensional nanomaterials," *Materials Today Energy*, vol. 28. Elsevier Ltd, Aug. 01, 2022. doi: 10.1016/j.mtener.2022.101065.

[159] G. R. Monama, K. E. Ramohlola, E. I. Iwuoha, and K. D. Modibane, "Progress on perovskite materials for energy application," *Results in Chemistry*, vol. 4. Elsevier B.V., Jan. 01, 2022. doi: 10.1016/j.rechem.2022.100321.

[160] M. Irshad *et al.*, "Photocatalysis and perovskite oxide-based materials: a remedy for a clean and sustainable future," *RSC Advances*, vol. 12, no. 12. Royal Society of Chemistry, pp. 7009–7039, Mar. 02, 2022. doi: 10.1039/d1ra08185c.

[161] J. Gong, M. Hao, Y. Zhang, M. Liu, and Y. Zhou, "Layered 2D Halide Perovskites beyond the Ruddlesden–Popper Phase: Tailored Interlayer Chemistries for High-Performance Solar Cells," *Angewandte Chemie - International Edition*, vol. 61, no. 10. John Wiley and Sons Inc, Mar. 01, 2022. doi: 10.1002/anie.202112022.

[162] G. Zhang, G. Liu, L. Wang, and J. T. S. Irvine, "Inorganic perovskite photocatalysts for solar energy utilization," *Chemical Society Reviews*, vol. 45, no. 21. Royal Society of Chemistry, pp. 5951–5984, Nov. 07, 2016. doi: 10.1039/c5cs00769k.

[163] Y. Hu *et al.*, "Layered perovskite oxides and their derivative nanosheets adopting different modification strategies towards better photocatalytic performance of water splitting," *Renewable and Sustainable Energy Reviews*, vol. 119. Elsevier Ltd, Mar. 01, 2020. doi: 10.1016/j.rser.2019.109527.

[164] K. Awaya and S. Ida, "Stress-Induced Photoluminescence Change of Monolayer Nanosheet Prepared by Delamination of Aurivillius-Phase Layered Perovskite," *Chemistry of Materials*, May 2023, doi: 10.1021/acs.chemmater.3c00466.

[165] Y. Wang, M. Liu, W. Chen, L. Mao, and W. Shangguan, "Ag loaded on layered perovskite H2SrTa2O7 to enhance the selectivity of photocatalytic CO2 reduction with H2O," *J Alloys Compd*, vol. 786, pp. 149–154, May 2019, doi: 10.1016/j.jallcom.2019.01.325.

[166] A. Mahmoud Idris *et al.*, "A heterostructure of halide and oxide double perovskites Cs2AgBiBr6/Sr2FeNbO6 for boosting the charge separation toward high efficient photocatalytic CO2 reduction under visible-light irradiation," *Chemical Engineering Journal*, vol. 446, Oct. 2022, doi: 10.1016/j.cej.2022.137197.

[167] S. Shyamal, S. K. Dutta, and N. Pradhan, "Doping Iron in CsPbBr3 Perovskite Nanocrystals for Efficient and Product Selective CO2 Reduction," *Journal of Physical Chemistry Letters*, vol. 10, no. 24, pp. 7965–7969, Dec. 2019, doi: 10.1021/acs.jpclett.9b03176.

[168] J. Pi *et al.*, "Surface and Defect Engineering Coupling of Halide Double Perovskite Cs2NaBiCl6 for Efficient CO2 Photoreduction," *Adv Energy Mater*, vol. 12, no. 43, Nov. 2022, doi: 10.1002/aenm.202202074.

[169] J. C. Wang *et al.*, "Surface Defect Engineering of CsPbBr3 Nanocrystals for High Efficient Photocatalytic CO2 Reduction," *Solar RRL*, vol. 5, no. 7, Jul. 2021, doi: 10.1002/solr.202100154.

[170] R. Konta, T. Ishii, H. Kato, and A. Kudo, "Photocatalytic activities of noble metal ion doped SrTiO3 under visible light irradiation," *Journal of Physical Chemistry B*, vol. 108, no. 26, pp. 8992–8995, Jul. 2004, doi: 10.1021/jp049556p.

[171] S. Ida *et al.*, " A Cocatalyst that Stabilizes a Hydride Intermediate during Photocatalytic Hydrogen Evolution over a Rhodium-Doped TiO 2 Nanosheet ," *Angewandte Chemie*, vol. 130, no. 29, pp. 9211–9215, Jul. 2018, doi: 10.1002/ange.201803214.

[172] H. Hata, Y. Kobayashi, V. Bojan, W. Justin Youngblood, and T. E. Mallouk, "Direct deposition of trivalent rhodium hydroxide nanoparticles onto a semiconducting layered calcium niobate for photocatalytic hydrogen evolution," *Nano Lett*, vol. 8, no. 3, pp. 794–799, Mar. 2008, doi: 10.1021/nl072571w.

[173] D. Jiang, T. Wang, Q. Xu, D. Li, S. Meng, and M. Chen, "Perovskite oxide ultrathin nanosheets/g-C3N4 2D-2D heterojunction photocatalysts with significantly enhanced photocatalytic activity towards the photodegradation of tetracycline," *Appl Catal B*, vol. 201, pp. 617–628, Feb. 2017, doi: 10.1016/j.apcatb.2016.09.001.

[174] L. Yang *et al.*, "An ultrathin two-dimensional iridium-based perovskite oxide electrocatalyst with highly efficient {001} facets for acidic water oxidation," *Journal of Energy Chemistry*, vol. 66, pp. 619–627, Mar. 2022, doi: 10.1016/j.jechem.2021.09.016.

[175] J. Wang *et al.*, "Ultrathin 2D NbWO6 Perovskite Semiconductor Based Gas Sensors with Ultrahigh Selectivity under Low Working Temperature," *Advanced Materials*, vol. 34, no. 2, Jan. 2022, doi: 10.1002/adma.202104958.

[176] Y. Liu *et al.*, "Highly Defective Layered Double Perovskite Oxide for Efficient Energy Storage via Reversible Pseudocapacitive Oxygen-Anion Intercalation," *Adv Energy Mater*, vol. 8, no. 11, Apr. 2018, doi: 10.1002/aenm.201702604.

[177] T. Kayoshi Oshima, M. Eguchi, and A. Maeda, "Photocatalytic Water Oxidation over Metal Oxide Nanosheets Having aT hree-Layer Perovskite Structure", doi: 10.1002/cssc.v9.4.

[178] A. J. Jacobson, J. T. Lewandowski, and J. W. Johnson, "ION EXCHANGE REACTIONS OF THE LAYERED SOLID ACID HCa2Nb3Olo WITH ALKALI METAL CATIONS," 1990.

[179] C. Ladasiu, N. Kulischow, R. Marschall, C. Ladasiu, N. Kulischow, and R. Marschall, "Tuning the Photocatalytic Activity of Layered Perovskite Niobates by Controlled Ion Exchange and Hydration."

[180] S. H. Kweon *et al.*, "Sintering behavior and dielectric properties of KCa2Nb3O10 ceramics," *J Eur Ceram Soc*, vol. 33, no. 5, pp. 907–911, May 2013, doi: 10.1016/j.jeurceramsoc.2012.11.017.

[181] S. Tahara and Y. Sugahara, "Interlayer Surface Modification of the Protonated Triple-Layered Perovskite HCa2Nb3O10·xH2O with n-Alcohols," *Langmuir*, vol. 19, no. 22, pp. 9473–9478, Oct. 2003, doi: 10.1021/la0343876.

[182] T. Oshima, T. Yokoi, M. Eguchi, and K. Maeda, "Synthesis and photocatalytic activity of K2CaNaNb3O10, a new Ruddlesden-Popper phase layered perovskite," *Dalton Transactions*, vol. 46, no. 32, pp. 10594–10601, 2017, doi: 10.1039/c6dt04872b.

[183] Y. Guo *et al.*, "Bi-functional ionic liquids facilitate liquid-phase exfoliation of porphyrin-based covalent organic frameworks in water for highly efficient CO2 photoreduction," *Green Chemistry*, 2022, doi: 10.1039/d2gc03194a.

[184] B. A. Pinaud, Z. Chen, D. N. Abram, and T. F. Jaramillo, "Thin films of sodium birnessite-type MnO2: Optical properties, electronic band structure, and solar photoelectrochemistry," *Journal of Physical Chemistry C*, vol. 115, no. 23, pp. 11830–11838, Jun. 2011, doi: 10.1021/jp200015p.

[185] D. Li *et al.*, "Noble-metal-free Mo2C co-catalsyt modified perovskite oxide nanosheet photocatalysts with enhanced hydrogen evolution performance," *Colloids Surf A Physicochem Eng Asp*, vol. 615, Apr. 2021, doi: 10.1016/j.colsurfa.2021.126252.

[186] N. Hirayama *et al.*, "Solar-Driven Photoelectrochemical Water Oxidation over an n-Type Lead-Titanium Oxyfluoride Anode," *J Am Chem Soc*, vol. 141, no. 43, pp. 17158–17165, Oct. 2019, doi: 10.1021/jacs.9b06570.

[187] L. M. Peter, A. B. Walker, T. Bein, A. G. Hufnagel, and I. Kondofersky, "Interpretation of photocurrent transients at semiconductor electrodes: Effects of band-edge unpinning," *Journal of Electroanalytical Chemistry*, vol. 872, Sep. 2020, doi: 10.1016/j.jelechem.2020.114234.

[188] W. Ma *et al.*, "Nickel and indium core-shell co-catalysts loaded silicon nanowire arrays for efficient photoelectrocatalytic reduction of CO2 to formate," *Journal of Energy Chemistry*, vol. 54, pp. 422–428, Mar. 2021, doi: 10.1016/j.jechem.2020.06.023.

[189] P. Li *et al.*, "Boosting oxygen evolution of single-atomic ruthenium through electronic coupling with cobalt-iron layered double hydroxides," *Nat Commun*, vol. 10, no. 1, Dec. 2019, doi: 10.1038/s41467-019-09666-0.

[190] H. Mirzajani *et al.*, "An ultra-compact and wireless tag for battery-free sweat glucose monitoring," *Biosens Bioelectron*, vol. 213, Oct. 2022, doi: 10.1016/j.bios.2022.114450.

[191] A. W. Kahsay *et al.*, "Selective and Low Overpotential Electrochemical CO 2 Reduction to Formate on CuS Decorated CuO Heterostructure," *Catal Letters*, vol. 149, no. 3, pp. 860–869, Mar. 2019, doi: 10.1007/s10562-019-02657-2.

[192] E. Karamian and S. Sharifnia, "On the general mechanism of photocatalytic reduction of CO2," *Journal of CO2 Utilization*, vol. 16, pp. 194–203, Dec. 2016, doi: 10.1016/j.jcou.2016.07.004.